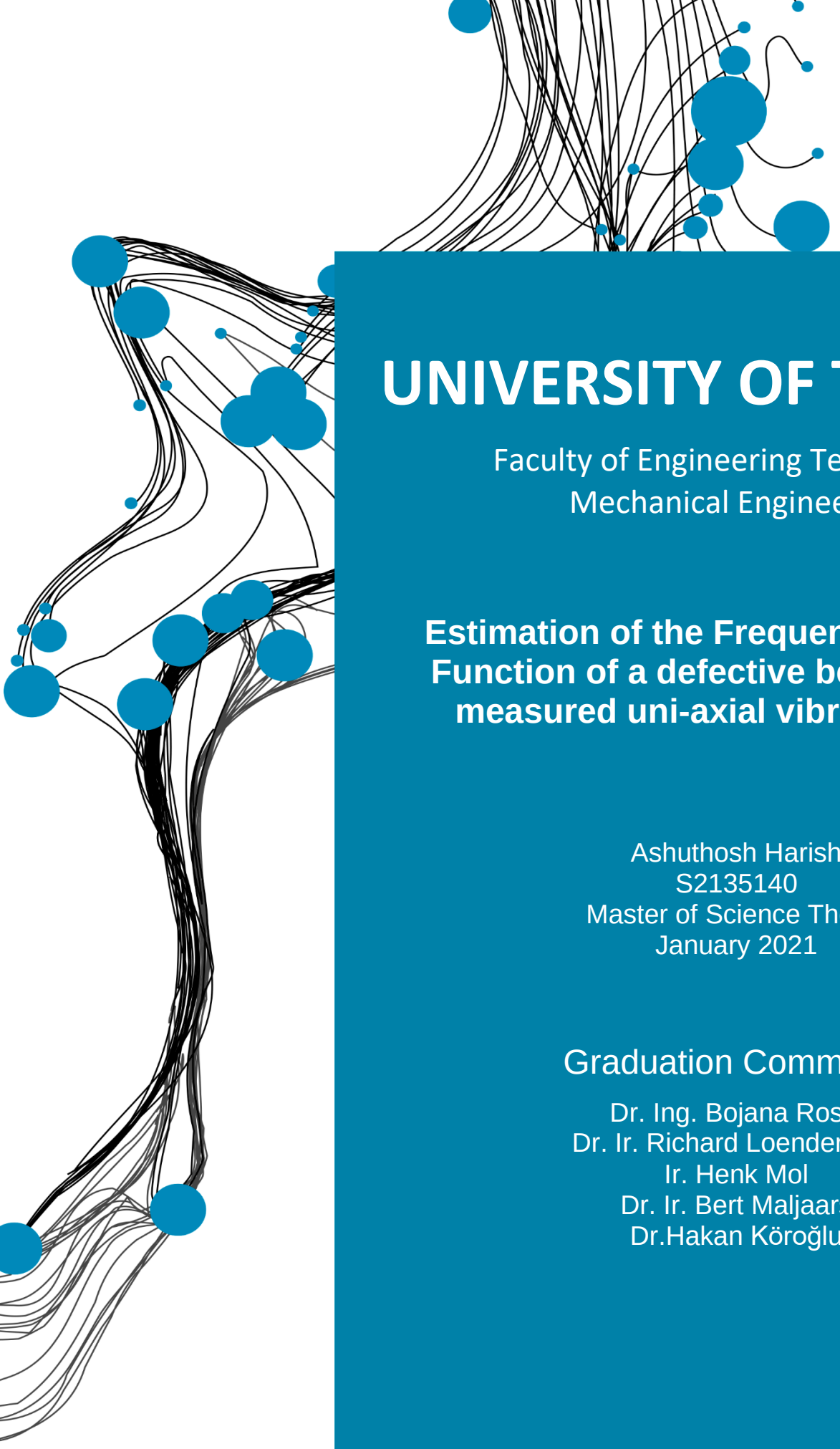

UNIVERSITY OF TWENTE.

Faculty of Engineering Technology,
Mechanical Engineering

Estimation of the Frequency Response Function of a defective bearing from a measured uni-axial vibration signal

Ashuthosh Harish
S2135140
Master of Science Thesis
January 2021

Graduation Committee

Dr. Ing. Bojana Rosic
Dr. Ir. Richard Loendersloot
Ir. Henk Mol
Dr. Ir. Bert Maljaars
Dr.Hakan Köroğlu

SKF®

UNIVERSITY OF TWENTE.

Summary

The axle bearing transmits the high axle load to the wheelsets while providing a smooth rolling-movement for the wheelsets in a train. The axle bearing's failure may result in unplanned breakdowns, derailment, wear on the wheel profile, damage to the track, and the train. Spalling is one of the significant causes of a failure of the axle bearing. The breakaway of material from the surface of the raceway is known as spalling. Condition monitoring techniques are developed to detect and estimate the size of the spall to mitigate the failure of the axle bearing and improve the uptime of the asset. The bearing's condition monitoring must be done by studying its response to the rolling-element moving over a spall, as bearings are sealed and integrated into the machinery. Among the many condition monitoring techniques available, the most common method is to observe the axle bearing's vibration response to the rolling-element and spall interaction, as this is the least invasive method and is characterized by low sensor cost.

The rolling-element and spall interaction results in an excitation pulse. The dynamic vibration response in the frequency domain to this excitation pulse has notches (local minima). The notches caused by the excitation pulse are dependent on the size of the spall and Hertzian contact length, or Hertzian contact length. These notches caused by excitation pulse can be used as a feature to estimate the size of the spall. However, the dynamic response spectrum will also have notches due to the anti-resonances of the bearing. Thus, making it difficult to differentiate between the notches caused by the excitation force pulse (spall size sensitive feature) and the anti-resonance. To precisely extract the notches caused by the excitation pulse in the bearing’s dynamic response spectrum, it is essential to separate the FRF (resonance and anti-resonance frequencies) from the measured dynamic response.

The notches (local minima) in the dynamic response spectrum caused by the excitation pulse are dependent on the speed and the load. The notches in the dynamic response spectrum caused by the bearing's anti-resonance are independent of speed and load. Based on the dynamic vibration response properties, three methods are developed to estimate the FRF of a bearing. The three methods are Mean Filter, Kalman Filter implementation, and Ensemble Kalman Filter Implementation.

Synthetic data is used to verify the three methods developed to estimate the FRF of a defective bearing. An experimental setup is developed to validate the theory on the dynamic response of a defective bearing and FRF estimation methods. The experimental study showed the theory on the rolling-element, and spall interaction is valid for small spalls (spall size is smaller than the Hertzian contact). However, the theory on the rolling-element spall interaction deviated at higher frequencies for large spalls (spall size is larger than the Hertzian contact). This was because of the damping effect of the lubrication.

The results of applying the Mean Filter method on the experimental data and synthetic data show that the Mean Filter successfully estimated the shape (resonance and anti-resonance) of the FRF of a bearing with either large or small spalls. However, fail to estimate the exact amplitude and the unit of the FRF. The Kalman Filter implementation method on the experimental data and synthetic data shows that this method successfully estimates the shape of the FRF for bearings with either large or small spalls. However, it is unable to estimate the amplitude of the FRF precisely. The Ensemble Kalman Filter implementation method successfully estimates the shape and the amplitude of the FRF of a bearing with small spalls. However, this method fails for large spalls at higher frequencies.

The scope for future work should focus on developing a more in-depth insight into the dynamic vibration response of bearing to a large spall and irregularly shaped spalls. It is believed that the quantification of the error in defective bearing preparation and experimental setup can further improve the Kalman filter and Ensemble Kalman filter formulation.

Acknowledgment

Throughout this master thesis, the author has received a great deal of support and assistance. The author would like to thank the University of Twente and SKF for facilitating and providing all the resources required to conduct the research leading to this thesis successfully.

The author would like to thank Bert Maljaars (SKF), Bojana Rosic (UT), Henk Mol (SKF), and Richard Londersloot (UT) for their intensive supervision. Lastly, the author would like to thank his family and friends for believing in him and encouraging him to give his best.

Contents

Nomenclature

Dynamics and vibration

M	Mass matrix	[kg]
C	Damping matrix	[kg/s]
K	Stiffness matrix	[N/m]
y	Displacement of the bearing	[m]
f	Force produced due to rolling-element and spall interaction	[N]
Δf	Amplitude of the excitation force pulse	[N]
t	Time	[s]
m	Mass	[kg]
ω	Frequency	[rad/s]
$H(\omega)$	Frequency response function	[m/N]
ω_n	Natural frequency	[rad/s]
ω_r	Resonance frequency	[rad/s]
T	Time interval	[s]
E	Young's modulus	[N/m^2]
I	Identity matrix	[-]
ξ	Damping ratio	[-]
v	Poisson's ratio	[-]
η	Measurement noise	[-]
R	Covariance of the measurement noise	[-]
S	State transition matrix	[-]
w	Modelling noise	[-]
Q	Modelling noise covariance matrix	[-]
G	Kalman Gain	[-]

Mathematical operators

$\mathcal{F}(.)$	Fourier transform operator
$\circ$	Hadamard product (element-wise matrix multiplication)
$()^T$	Transpose

Bearing frequencies and parameters

V	The velocity of the rolling element over the spall	[m/s]
L	Length of the defect in the direction of rotation	[m]
b	Half Hertzian contact	[m]
d_p	The pitch diameter of the bearing	[m]
α	Contact angle between the rolling element and the raceway	[rad]
D	Diameter of the rolling-element	[m]
$F(\rho)_l$	Curvature-difference of rolling element and raceway	[m^{-1}]
f_{ir}	Rotational speed of the inner ring	[Hz]
f_{ord}	Outer-ring defect frequency	[Hz]
f_{red}	Inner-ring defect frequency	[Hz]
f_{ird}	Rolling-element defect frequency	[Hz]
z	Number of rolling-elements in the bearing	[Hz]
C_l	Constant related to the material properties of the bearing	[-]
Q	Load on the rolling-element	[N]

Indices

i	Inner ring
re	Rolling element
o	Outer ring
k	Speed step
l	Symbol used to represent both the inner-ring and outer-ring (i.e., l = i, o)

1 Introduction

The first chapter of this thesis introduces the research conducted at SKF in collaboration with the University of Twente. This chapter helps to understand the need, motivation, and objective of the research.

A brief introduction on the importance of monitoring the condition of a bearing in railway application is explained in Section 1.1. Following this, the different condition monitoring techniques and the challenges in implementing the condition monitoring techniques are explained in Section 1.2. Based on the challenges in monitoring the condition of a bearing, the research objective of this thesis is presented in Section 1.3. The overview of the report is given in Section 1.4.

1.1 Need for condition monitoring of a bearing in a railway application

The European Union in 2011 had set a target of shifting as much as 30% of the road transport to other modes of transport such as rail or waterborne transport by 2030 to reduce the negative effect (traffic jams, damage to the environment, noise, accidents) of a dominating road transport [1]. To achieve this target, the railway industry is under immense pressure to make railway travel the more efficient, affordable, and available mode of transport for freight and passengers.

The trains are operated under high axle load to make the railway travel fulfill the freight and passenger transport requirements [2]. The axle bearing transmits this high axle load to the wheelsets while providing a smooth rolling-movement for the wheelsets [3]. The high axle load results in high pressure at the contacts of the rolling-elements and the raceways of the axle bearings. The high pressure at the contacts between the rolling-elements and the raceways of the axle bearing does not allow much deviation from the ideally smooth surfaces of a bearing.

Any small imperfection in the contact surface between the rolling-element and the raceways results in the failure of the axle bearing. The contaminants (particles) entering the bearing is one of the significant causes for the surface imperfection in the railway axle bearings [4, 5]. These particles are over-rolled by the rolling-elements. The over-rolling creates indentations in the raceways, as shown in Figure 1.1a. The indentation results in stress concentration. This indentation is then subjected to cyclic stress by the rolling-elements, initiating the surface fatigue and eventually causing the metal to break away from the raceway, as shown in Figure 1.1b and Figure 1.1c. The breakaway of material from the surface of the raceway is known as spalling. Once the spalling has occurred, the damage progresses until the bearing becomes unserviceable, as seen in Figure 1.1d.

The axle bearing's failure may result in wear on the wheel profile, damage to the track, unplanned breakdowns, and derailment [6]. Therefore, condition monitoring of the axle bearing is essential to estimate the size of the spall, to detect and mitigate the failure of the bearing.

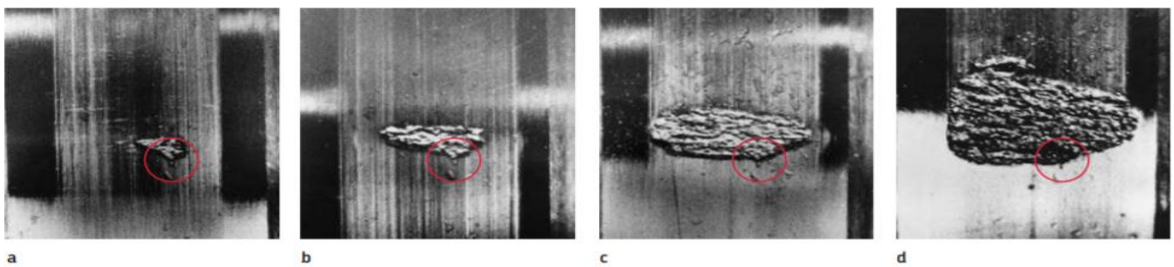

Figure 1.1 Damage progression [4].

1.2 Different condition monitoring techniques of a bearing

The bearing's condition monitoring must be done by studying its response to the rolling-element moving over a spall, as bearings are sealed and integrated into the machinery. A closed housing with a sealing system is used to prevent contamination and grease leakage of a train's axle bearing. Among the many condition monitoring techniques available, the most common technique is to observe the axle bearing's vibration response to the rolling-element and spall interaction, as this is the least invasive technique and is characterized by low sensor cost [5].

The different condition monitoring algorithms developed for vibration analysis can be broadly divided into two categories:

- event detection method: The events of the entry of rolling-element into the spall and exit from the spall are detected in the time domain to estimate the spall size.
- spectral method: The spall size is estimated based on the spectral content of vibration response of a bearing caused by the rolling-element and spall interaction.

1.2.1 Event detection method

In reference [7], the authors proposed that the rolling-element's interaction with the spall resulted in two events, the first event originating from the entry of the rolling-element into the spall (de-stress) and the second event being due to the departure of the rolling element from the spall (re-stress). This theory on rolling-element and spall interaction has been proven numerically in [8], analytically in [9, 10, 11], and experimentally in [5, 12, 13]. The spall size can be estimated by calculating the time between the de-stressing of the rolling-element at the entry of the spall and the impact of the rolling-element with the spall's edge at the exit of the spall.

In real life application of the condition monitoring techniques on a bearing in railway application, extracting the low-energy entry event from the noisy raw vibration signal is complicated. Thus, making it difficult to estimate the correct size of the spall. Several methods are developed to extract the low energy entry of the rolling-element into the spall.

Several studies [14, 15, 16, 17, 18, 19] proposed a wavelet transform to reduce the ambiguity in detecting rolling-element entry and exit components of the vibration signal by improving the sharpness of the vibration signal. The wavelet methods successfully detected the entry and exit event from vibration data of a rectangular spalled bearing in a controlled test rig. However, in the natural case with irregular spalls, the exact point of entry was found to be ambiguous and difficult to detect from the vibration data [20].

In reference [7, 21], the authors proposed synchronous averaging or minimum entropy deconvolution to pre-whiten the raw signal to remove the ambiguity in estimating the exact entry point of the rolling-element into the spall. Then applied wavelet and envelope analysis on the pre-whitten signal to enhance the detection of entry and exit events. Similarly, in reference [20], the authors proposed an auto-regressive model on the raw vibration signal to extract the pre-whitened signal. Then Hilbert transform is applied to the pre-whitened signal to determine the entry and exit events.

The pre-whitening based on the cyclo-station properties, combined with wavelet decomposition or Hilbert transform, successfully estimated the size of a spall from a vibration signal of a bearing with naturally occurring spalls [7, 20, 21]. However, these techniques failed when used for raw vibration data from a railway application because of the high vibration noise.

1.2.2 Spectral method

The spectral method described in reference [5], unlike the event detection method, does not need to extract the exact entry and the exit point of the rolling element into the spall. The author proposed that a rectangular force pulse is produced when the rolling-element moves over a spall. For spalls bigger than the Hertzian contact length, the rectangular force pulse duration is inversely proportional to the size of the spall.

The Fourier transform of this force pulse has local minima (so-called 'notch frequency') at certain frequencies; at these frequencies, the bearings are not excited by the rectangular force pulse. Thus, the bearing's dynamic response spectrum has notches (local minima) where the bearing is not excited by the excitation force pulse. The authors proposed the notch frequencies (local minima) in the spectrum of a bearing's dynamic response as a feature to estimate the spall size on the surface of the bearing. A detailed description of this theory is further explained in chapter 2.

As observed by the vibration sensor, the dynamic response of the bearing to the rolling-element moving over a spall depends not only on the magnitude of the excitation force but also on the frequency of the excitation. The effect of the latter is highly non-linear [22]. At certain frequencies, the so-called resonance frequencies, the response can be much higher than the excitation force amplitude. On the other hand, there also may exist frequencies where the response amplitude approaches zero, so-called anti-resonance frequencies. This non-linear function, which relates the excitation force to the bearing's dynamic response, is known as the frequency response function (FRF). Therefore, the dynamic response spectrum has notches due to the excitation force pulse and the anti-resonance frequencies of the bearing. Thus, it is difficult to differentiate between the notches caused by the excitation force pulse and the anti-resonance frequencies.

Estimating the FRF of the bearing from its measured vibration signal will make it possible to precisely locate the notches caused by the excitation pulse and the anti-resonance frequencies of the bearing. Several studies proposed experimental modal analysis to estimate the FRF [23, 24]. The complexity is that the machine's frequency response function is often not entirely repeatable nor reproducible between identical copies of a bearing system [5, 25]. This is because bearing and its housing are produced with a finite three-dimensional geometrical accuracy, causing additional dynamic forces in the system and changes in the load distribution. As a result, it is challenging to standardize the FRF of a bearing system.

1.3 Research objectives

The spectral analysis method proposed in reference [5] provides a new way to approach the spall size estimation in the bearing. However, to effectively monitor the spall size using the spectral methods, it is essential to separate the system's FRF and the excitation pulse.

In this thesis, a robust algorithm is developed to estimate the FRF of a defective bearing from its vibration response caused by the rolling-element and spall interaction using a uni-axial vibration sensor. This master thesis tries to answer the following question.

How to estimate the frequency response function by processing the uni-axial vibration response of a rolling-element moving over a spall located on the bearing's outer-ring?

Some subquestions are made that could help estimate the frequency response function from the measured vibration response of a defective bearing. The subquestions are:

- How do the properties of the dynamic response of a defective bearing change with the speed, load, and size of the spall?

- How to process the vibration signal to extract the bearing's dynamic response in the frequency domain to the rolling-element moving over a spall?
- How can the uniaxial dynamic response of a defective bearing be processed to estimate the frequency response function?

With the help of these questions, a methodology will be proposed to extract the frequency response function from the measured uni-axial vibration signal.

1.4 Report overview

This report gives an overview of what is achieved during a Master thesis on the subject of estimating the FRF from the measured vibration signal of a uni-axial vibration sensor. Chapter 1 introduces the problem and the focus area of the research. Chapter 2 includes the relevant theoretical background on the excitation pulse, the FRF, and the bearing's dynamic response. In Chapter 3, the methods to estimate the FRF from the measured vibration signal based on the properties of the excitation pulse and FRF are explained. Chapter 4 explains the experimental setup, measurement procedures, and signal processing techniques to extract the dynamic response of a bearing in the frequency domain. Chapter 5, the analysis and discussion on the FRF extracted from the experimental data using the methods developed in Chapter 3, is presented. Finally, Chapter 6 gives the conclusion and suggestions for future work.

2 Theory on dynamic vibration response

In this chapter, a detailed theory on the bearing's dynamic response, the frequency response function (FRF), and the excitation pulse are discussed. First, the relationship between the bearing's dynamic response, FRF, and excitation pulse spectrum is presented in Section 2.1. Following this, a detailed theory on the excitation pulse in the time and frequency domain is presented in Section 2.2 and Section 2.3, respectively. Next, the detailed theory on the FRF is explained in Section 2.4. The Kinematic properties of the bearing are presented in Section 2.5.

2.1 The relation between dynamic response, FRF, and excitation pulse

The equation of motion that describes the dynamic behavior of a bearing to a rolling-element moving over a spall is given by:

$$M\ddot{y}(t) + C\dot{y}(t) + Ky(t) = f(t) \tag{2.1}$$

where M is the mass matrix, C is the damping matrix, K is the stiffness matrix of the bearing. $f(t)$ is the column vector of the force pulse produced at the location of the spall due to the rolling-element moving over a spall. The force $f(t)$ is known as the excitation force. $y(t)$ is the column vector describing the displacement of the bearing at the location of the sensor as a response to the excitation force.

The bearing's displacement depends on the excitation force's amplitude and the frequency of the excitation force. At certain excitation frequencies, the response amplitudes are much higher, and these frequencies are called resonance frequencies, and at certain excitation frequencies, the response amplitude approaches zero, and these excitation frequencies are called anti-resonance frequencies. To understand the effect of resonance frequencies and anti-resonance frequencies on the dynamic response of the bearing, it is interesting to express the displacement of the bearing at the location of the sensor $y(t)$ in the frequency domain. This is done by applying Fourier transform on Equation (2.1), as seen below:

$$\mathcal{F}(M\ddot{y}(t) + C\dot{y}(t) + Ky(t)) = \mathcal{F}(f(t)) \tag{2.2}$$

With,

$$\begin{aligned} \mathcal{F}(M\ddot{y}(t)) &= -M\omega^2 y(\omega) \\ \mathcal{F}(C\dot{y}(t)) &= Ci\omega y(\omega) \\ \mathcal{F}(Ky(t)) &= Ky(\omega) \\ \mathcal{F}\big(f(t)\big) &= f(\omega) \end{aligned} \tag{2.3}$$

where $\mathcal{F}$ is the Fourier operator. Equation (2.2) in the frequency domain is given by:

$$-M\omega^2 y(\omega) + Ci\omega y(\omega) + Ky(\omega) = f(\omega) \tag{2.4}$$

In the frequency domain, the equation of the motion with m degree of freedom can be reduced to a set of m decupled second order differential equations of a single degree of freedom system. A signal degree of freedom system in the frequency domain is given by:

$$[-m\omega^2 + ic\omega + k]y(\omega) = f(\omega) \tag{2.5}$$

One of the ways to define FRF $h(\omega)$ is as the dynamic response of the bearing divided by the excitation force, and is given by:

$$h(\omega) = \frac{f(\omega)}{y(\omega)} = \frac{1}{-m\omega^2 + ic\omega + k} \tag{2.6}$$

$$y(\omega) = h(\omega)f(\omega) \tag{2.7}$$

From Equation (2.7), it can be seen that the displacement in the frequency domain $y(\omega)$ of the bearing at the location of the sensor is a product of the excitation pulse in the frequency domain $f(\omega)$ with the bearing's FRF $h(\omega)$.

2.2 Excitation force

In this section, a detailed explanation of the source of excitation in a bearing is given. During the operation of the bearing, the bearing's load is distributed over the contacts between the rolling-elements and the raceway. Any imperfections like spalls on the surface of the raceways result in a force pulse.

The force pulse excites the structure, and therefore it is called the excitation force pulse. For a bearing, the excitation force pulse is dependent on the type of the spall. Based on the length of the spall measured in the running direction of the rolling-element, spalls are classified into two categories:

- small spalls: The spall's length measured in the rolling-element's running direction is less than the Hertzian contact length between the rolling-element and the spall. The passing of the rolling element over the spall results in a single force pulse.
- large spalls: The spall's length in the running direction is more than the Hertzian contact length between the rolling-element and the spall. The passing of the rolling-element results in multiple pulses with varying frequency content.

A detailed explanation of the force pulse generated due to the rolling-element moving a small spall and large spall is given in the next subsections.

2.2.1 Small spall

The pressure distribution in the contact zone between the rolling-element and the raceway is disturbed when the rolling element moves over a small spall. This pressure disturbance results in a rectangular excitation force pulse [26]. From [26], the duration of the excitation force pulse for a small spall is approximated to be:

$$T = \frac{2b}{V} \tag{2.8}$$

where $2b$ is the semi-minor axis of the projected contact ellipse between the rolling-element and raceway of the bearing on which the spall is located, as shown in Figure 2.1. V is circumferential speed with which the contact areas between the rolling-element and the surface of the spall move.

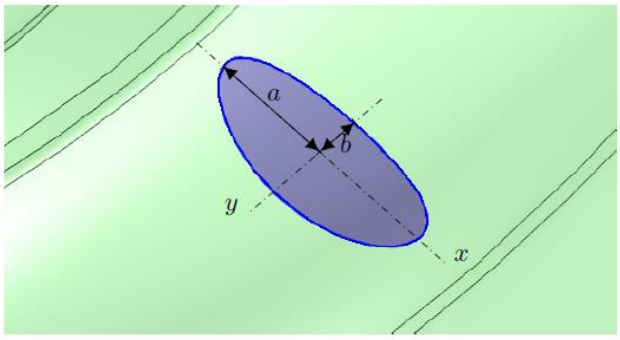

Figure 2.1 Schematic of the contact area between the rolling-element and the raceway. This contact area is in the shape of an ellipse with semi-axes a and b [29].

From Equation (2.8), it can be seen that the Hertzian contact length and the circumferential speed of the rolling-element determine the duration of the contact force disturbance. From reference [27], the half Hertzian contact length is given by:

$$b_l = b_l^* C_l \left[\frac{L}{\Sigma \rho_l}\right]^{\frac{1}{3}} \tag{2.9}$$

b_l (with l= i (inner-ring), o (outer-ring)). b^* and δ^* are dimensionless contact parameters obtained from Table 3 in Appendix A; the curvature-difference $F(\rho)_l$ given by the Equation (2.10); The $\Sigma(\rho)_l$ is a constant related to the geometry of the bearing given by the equation (2.11); C_l is a constant related to the material properties of the bearing of the bearing given by the Equation (2.12). L is the load on each rolling-element given by the Equation (2.13).

$$F(\rho)_l = \frac{\frac{1}{r_l} + \frac{1}{\frac{1}{2}\left[\frac{d_p}{\cos(\alpha)} - D\right]}}{\Sigma(\rho)_l} \tag{2.10}$$

$$\Sigma(\rho)_l = \frac{4}{D} - \frac{1}{r_l} + \frac{1}{\frac{1}{2}\left[\frac{d_p}{\cos(\alpha)} - D\right]} \tag{2.11}$$

$$C_l = \left[\frac{3}{2}\left[\frac{1-v_l^2}{E_l} + \frac{1-v_{re}^2}{E_{re}}\right]\right]^{\frac{1}{3}} \tag{2.12}$$

$$L_l = \left[\frac{C_l^2}{2}\right]^{\frac{-3}{2}} \delta_l^{*\frac{-3}{2}} \Sigma(\rho)_l^{\frac{-1}{2}} \delta_l^{\frac{3}{2}} \tag{2.13}$$

In the above equations, the r_l (with,l= i (inner-ring), o (outer-ring), re (rolling-element)) is the groove curvatures of the inner and outer raceway; *D* is the diameter of the rolling-elements; d_p is the is pitch circle diameter of the bearing; α is the contact angle between the rolling-element and the raceway; v_l is the Poisson's ratio; E_l Young's modulus; the deformation of the contact at the outer and inner ring is represented by δ_l.

From Equations (2.9) to (2.13), it can be seen that the b_l , the half Hertzian contact length in the direction of the rotation depends on the geometry, material, and load on the bearing. Therefore, the duration of the excitation pulse T depends on the geometry, material, load, and rotational speed of the bearing.

2.2.2 Large spall

In reference [7], the authors proposed that the interaction of the rolling-element with the spall resulted in two events, the first event originating from the entry of the rolling-element into the spall (de-stress) as seen in Figure 2.2a and Figure 2.2b, and the second event due to the departure of the rolling-element from the spall (re-stress) as seen in Figure 2.2c and Figure 2.2d. This assumption is proven numerically in [28], analytically in [9], and experimentally in [13].

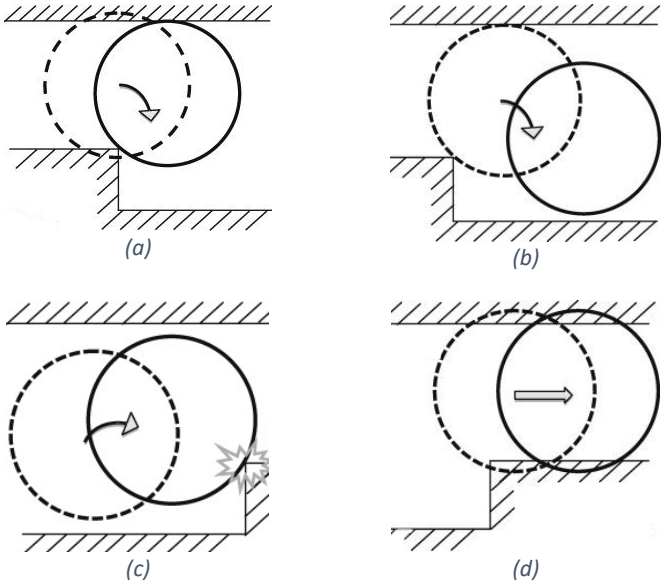

Figure 2.2 Rolling-element and spall interaction [13]

During the entry phase, a gradual de-stressing of the rolling-element into the spall, as seen in Figure 2.2a. Then, the contact between the rolling-element and the spall is released, as shown in Figure 2.2b. During the leaving phase, the rolling-element strikes the spall's exit edge and excites the high-frequency resonance modes of the bearing, as seen in Figure 2.2c. The rolling-element re-stresses between the raceways at the edge of the spall to its normal load carrying capacity, as shown in Figure 2.2d.

Between the de-stressing and re-stressing, the contact between the rolling-element and spall is released, which results in a force pulse. In reference [5], the authors use a quasi-static finite element analysis to approximate the amplitude of force pulse to be equal to the negative of the static load on the rolling-element:

$$f \propto -(\text{stationary load on the rolling element}) \tag{2.14}$$

From reference [5], the duration of the excitation force pulse is given by:

$$T = \frac{2b + L}{V} \tag{2.15}$$

Where $2b$ is the semi-minor axis of the projected contact ellipse between the rolling-element and raceway of the bearing. V is the speed with which the contact areas move through the spall. L is the length of the spall in the direction of rotation. Through the explanation of the Hertzian contact theory in section 2.2.1, it is seen that the Hertzian contact length is dependent on the geometry, material of the bearing, and load on the bearing. Thus, the duration of the excitation force pulse for a large spall depends on the spall size, geometry, material of the bearing, load on the bearing, and rotational speed of the bearing.

2.3 Excitation force spectrum

In this section, the excitation force in the time domain is transformed into the frequency domain, and the properties of the excitation pulse spectrum are discussed. The Fourier transform of the rectangular pulse of small spall and large spall is a sinc function given by the equation:

$$f(\omega) = \mathcal{F}(f(t)) = f \int_{\frac{-T}{2}}^{\frac{T}{2}} e^{-i\omega t} dt \; = \; f\,T \frac{sin\left(\pi T \frac{\omega}{2\pi}\right)}{\pi T \frac{\omega}{2\pi}} \tag{2.16}$$

where T is the duration of the over-roll given by Equations (2.8) and (2.15) for small spalls and large spalls, respectively; f is the amplitude of the excitation pulse; The equation (2.16) tends to zero when $\omega = {}^{n}/_{T}$, where n is a positive integer and T is the duration of the excitation pulse. The frequencies at which equation (2.16) is zero are called 'notch frequency', as seen in Figure 2.3. Notch frequencies are a distinctive feature of rectangular pulse-like excitations.

For a bearing, under a constant load, the increase in the bearing's rotational speed results in a decrease in the excitation force pulse duration. The notch frequency bandwidth is inversely proportional to the duration of excitation. The notch frequency bandwidth increases with an increase in the rotational speed, as seen in Figure 2.3. The left side of Figure 2.3 represents the excitation force pulse produced due to a rolling-element and spall interaction at the speed of 500RPM, 1000RPM, and 1500RPM with 300N force between the rolling-element and raceway. The right side (Column B) contains the respective excitation force pulse in the frequency domain. The notch frequencies are approximately 1900Hz, 3800Hz & 57002Hz at 500RPM, 1000RPM, and 1500RPM, respectively.

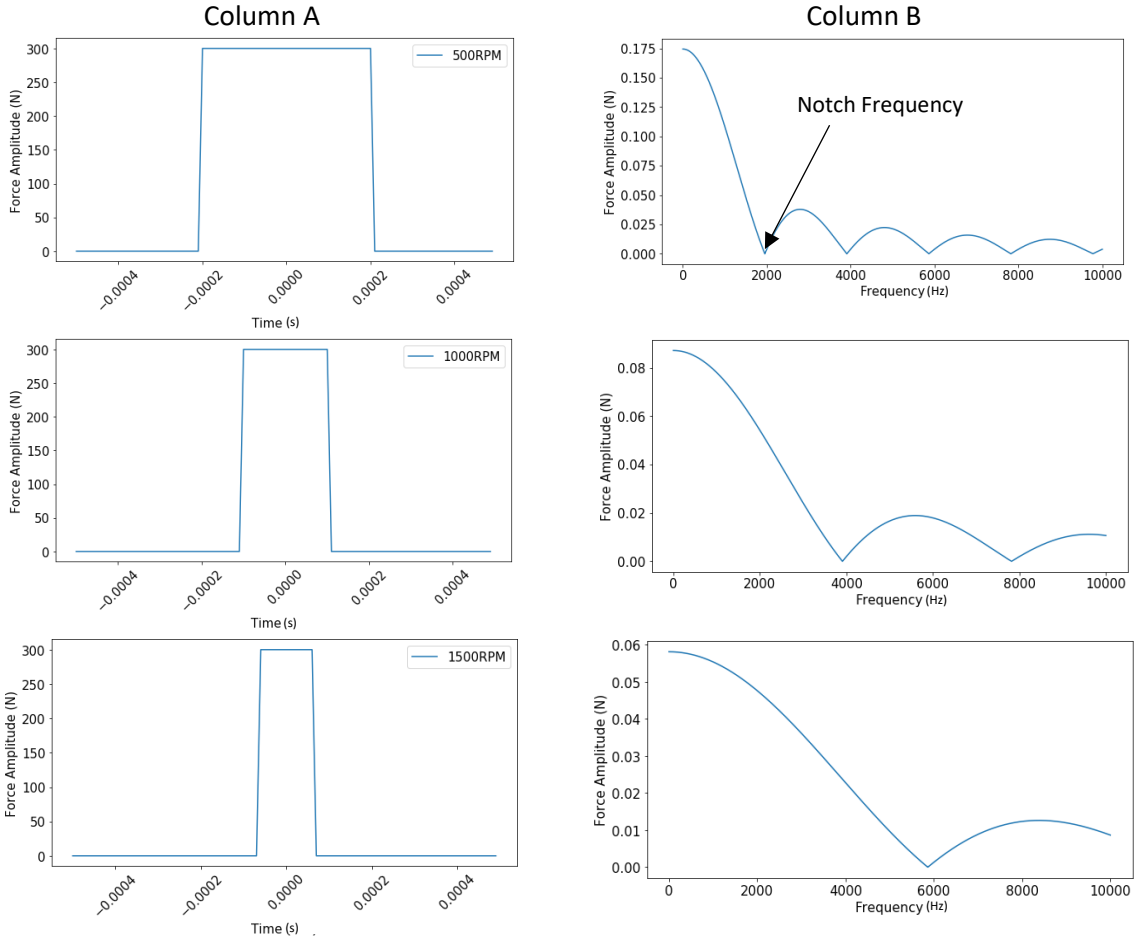

Figure 2.3 Excitation pulse time and frequency domain.

2.4 Frequency response function

In this section, a detailed explanation of the FRF is presented. From Equation (2.7). The frequency response function $h(\omega)$ is defined as the dynamic response of the bearing divided by the excitation force given by:

$$h(\omega) = \frac{y(\omega)}{f(\omega)} = \frac{1}{-m\omega^2 + ic\omega + k} \tag{2.17}$$

Equation (2.17) can be rewritten as:

$$h(\omega) = \frac{y(\omega)}{f(\omega)} = \frac{\frac{1}{k}}{-\frac{m}{k}\omega^2 + i\omega\frac{c}{k} + 1} \tag{2.18}$$

The undamped natural frequency and the damping ratio of a system are given by the equations:

$$\omega_n = \sqrt{\frac{k}{m}} \tag{2.19}$$

$$\xi = \frac{c}{2\sqrt{mk}} \tag{2.20}$$

where ξ is the damping ratio and ω_n is the undamped natural frequency. The undamped natural frequency of a bearing is the frequencies at which the bearing tends to oscillate in the absence of any driving or damping force. By combining the Equations (2.18), (2.19), and (2.20), the FRF can be written as:

$$h(\omega) = \frac{\frac{1}{k}}{-\left[\frac{\omega}{\omega_n}\right]^2 + 2i\xi\left[\frac{\omega}{\omega_n}\right] + 1} \tag{2.21}$$

Equation (2.21) is in the complex domain and can be expressed in terms of magnitude and phase. The equation for the magnitude and phase of Equation (2.21) is given by Equations (2.22) and (2.23), respectively.

$$|h(\omega)| = \frac{\frac{1}{k}}{\sqrt{\left[1 - \left[\frac{\omega}{\omega_n}\right]^2\right]^2 + \left[2\xi\frac{\omega}{\omega_n}\right]^2}} \tag{2.22}$$

$$\angle h(\omega) = -arctan\left(\frac{2\xi\frac{\omega}{\omega_n}}{1 - \left[\frac{\omega}{\omega_n}\right]^2}\right) \tag{2.23}$$

From equation (2.22), the following observations are made

- In an undamped situation, the amplitude of the FRF is infinite at frequencies equal to the natural frequency.
- The maximum amplitude of the FRF is at the frequencies where the derivative of the FRF function is zero. This point where the FRF reaches a maximum is called resonance frequency and is the damped natural frequency:

$$\omega_r = \omega_n\sqrt{1 - 2\xi^2} \tag{2.24}$$

- The magnitude at the location of the resonance frequencies is given by:

$$|h(\omega_r)| = \frac{\frac{1}{k}}{2\xi\sqrt{1-\xi^2}} = \frac{m}{c\sqrt{mk - \frac{1}{2}c^2}} \tag{2.25}$$

Equation (2.25) shows that the FRF is dependent on the mass, stiffness, and damping of the system (system: bearing, housing, and the location of the sensors). The stiffness, damping, and mass of no two systems are the same as the bearings, housing, and location of the sensors are manufactured and integrated with a certain tolerance. Therefore, the FRF of no two systems is the same.

In reference [27], the authors proposed an experimental modal analysis to estimate the FRF of fault-free bearing under the different rotating speed of the bearing. It was seen that the variation in the FRF of the bearing caused by varying speed was comparable to the variation in the FRF estimated at the same speed. Similar results can be seen in references [28] and [29]. So, it is safe to assume that the bearing's FRF is independent of speed.

The FRF under different loading conditions is similar because the change in the stiffness because of the applied load is negligible compared to the bearing's mass. The stiffness increase is $10^{-7}m^{-1}$ (from simpro simulation) for a 100N increase in the load. The mass of the 6206 bearings is approximately 0.2kg. Thus, the increase in stiffness is negligible compared to the mass of the 6206 bearings. As the stiffness increase is negligible compared to the bearing's mass, the FRF is expected to remain the same for a 6206 bearing with an increase in the load of 100N.

2.5 Kinematics of the bearing

The excitation force pulse generated by the rolling-element and spall interaction is not a single event, but a cyclo-stationary event as a bearing has a set of the rolling-elements which interacts with the spall in a specific time interval. This interval between two consecutive interactions is derived by studying the kinematics of the bearing. This frequency of the rolling-element and spall interaction for a stationary outer-ring when then spall is located on the outer-ring raceway, inner-ring raceway, and the rolling-element is given by equation (2.26), (2.27), and (2.28), respectively [29].

$$f_{ord} = \frac{z f_{ir}\left[d_p - d_{re}\cos(\alpha)\right]}{2d_p} \tag{2.26}$$

$$f_{red} = \frac{z f_{ir} d_{re}}{d_p}\left[1 - \frac{d_{re}}{d_p}\right]^2 cos^2(\alpha) \tag{2.27}$$

$$f_{ird} = \frac{z f_{ir}\left[d_p + d_{re}\cos(\alpha)\right]}{2d_p} \tag{2.28}$$

Where f_{ord}, f_{ird}, and f_{red} outer-ring defect frequency, inner-ring defect frequency, and rolling-element defect frequency, respectively; z is the number of rolling-elements in the bearing; d_{re} is the diameter of the rolling element; d_p is pitch diameter of the bearing; f_{ir} the rotational speed of inner-ring in Hz. α is the contact angle between the rolling element and raceway.

3 Methods to estimate the frequency response function

In this chapter, three different algorithms (Mean Filter, Kalman filter implementation, and Ensemble Kalman filter implementation) in estimating the FRF by processing a defective bearing's dynamic response are explained with the help of synthetic data. The synthetic data set is described in the Appendix B. These algorithms are implemented based on the properties of the excitation pulse spectrum and the FRF presented in Chapter 2.

3.1 Mean Filter Implementation

The dynamic response of the bearing when the rolling-element moves over a spall at speed-step s, as described in Section 2.1 is given by:

$$y_k = F_k h_k + \eta_k \tag{3.1}$$

where y_k is a $n \times 1$ vector of the dynamic response spectrum to a rolling-element moving over a spall, n is the number of frequency bins in the dynamic response spectrum; F_k is a diagonal matrix ($n \times n$ matrix) with excitation pulse spectrum f_k as the elements of the diagonal matrix and h_k is the FRF of the system; η_k is the measurement noise.

The mean of all the measured vibration response spectrum over different speed is given by:

$$\bar{y} = \frac{1}{k}\left[\sum_{k=1}^{20} y_k\right] = \bar{F}h \tag{3.2}$$

where $\bar{y}$ is the mean of the measured dynamic response spectrum over a speed-step 1 to speed-step 20. $\bar{F}$ is the mean of the excitation pulse spectrum over a speed-step 1 to speed-step 20. h is the FRF, which is independent of speed. The mean of the excitation pulse spectrum ($\bar{F}$) results in a function that is decreasing in magnitude with an increase in frequency, as shown in Figure 3.1. Thus, taking the mean of the dynamic response spectrum smoothens the notches and peaks caused by the excitation pulse. It retains the notches and peaks caused by the anti-resonance and the resonance of the system.

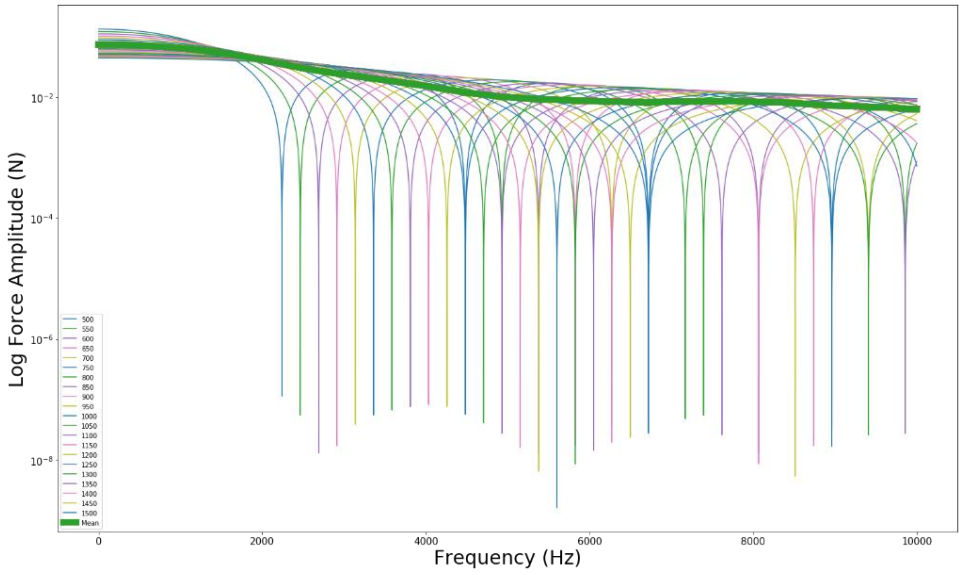

Figure 3.1 Mean of the excitation pulse spectrum.

Figure 3.2 compares the actual FRF (ground truth) and the Mean Filter estimate of the FRF of synthetic data. It is seen that:

- the estimated FRF has a similar shape (peaks and notches) compared to the actual FRF.
- the estimated FRF has a shift in its amplitude. This shift in the amplitude is equal to the amplitude of the mean of the excitation pulse spectrum.
- that the unit of the estimated FRF (m) is not the same as that of the actual FRF (m/N).

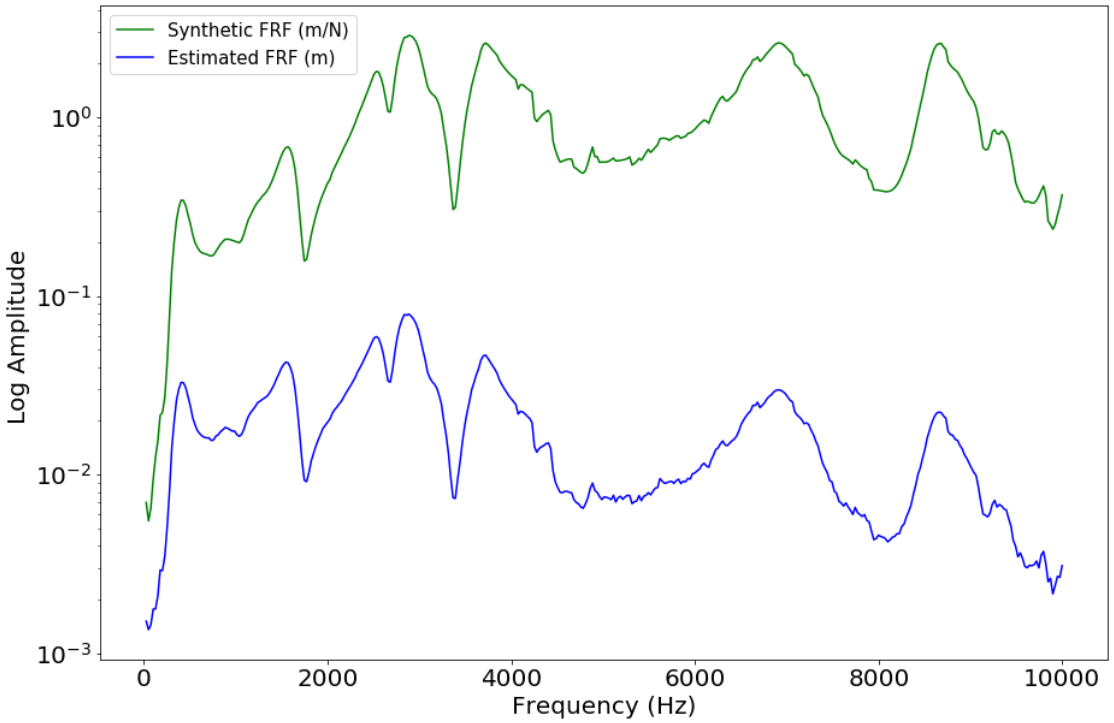

Figure 3.2 Estimated & Actual FRF of the synthetic data.

3.2 Kalman Filter Implementation

Kalman filter is an optimum linear filter invented in 1960 by Kálmán [30]. The Kalman filter estimates the unmeasured state of a system based on the knowledge of the system dynamics and the available noisy measurements. Thus, the Kalman filter is selected as one of the techniques to determine the unmeasured internal state of the FRF from the noisy measured data. It is also interesting to note that most of the Kalman filter parameters can be calculated offline, reducing the time required to operate the algorithm online in real-time application [31].

An overview of the first complete loop of the Kalman filter implementation to estimate the FRF is shown in Figure 3.3. The Kalman Filter is a recursive linear filter. The Kalman filter is first initialized by assuming an initial estimate of the FRF with mean $\bar{h}_0^+$ and covariance P_0^+ before the availability of the measured data at the first speed-step. The initial estimate of the FRF ($\bar{h}_0^+$ and P_0^+) is propagated to the first speed-step using the prediction equations, and the predicted estimate of the FRF at the first speed-step is given by mean $\bar{h}_1^-$ and covariance P_1^-. The predicted estimate of the FRF ($\bar{h}_1^-$ and P_1^-) at the first speed-step is updated with noisy measurement data y_1 to obtain an updated estimate of the FRF ($\bar{h}_1^+$ and P_1^+) at the first speed-step. This updated estimate at the first speed-step will be used as an initial estimate for the second speed-step. This complete process continues for all the measured data. A detailed description of the assumptions at each step of the Kalman filter implementation to estimate the FRF is presented in the next subsections.

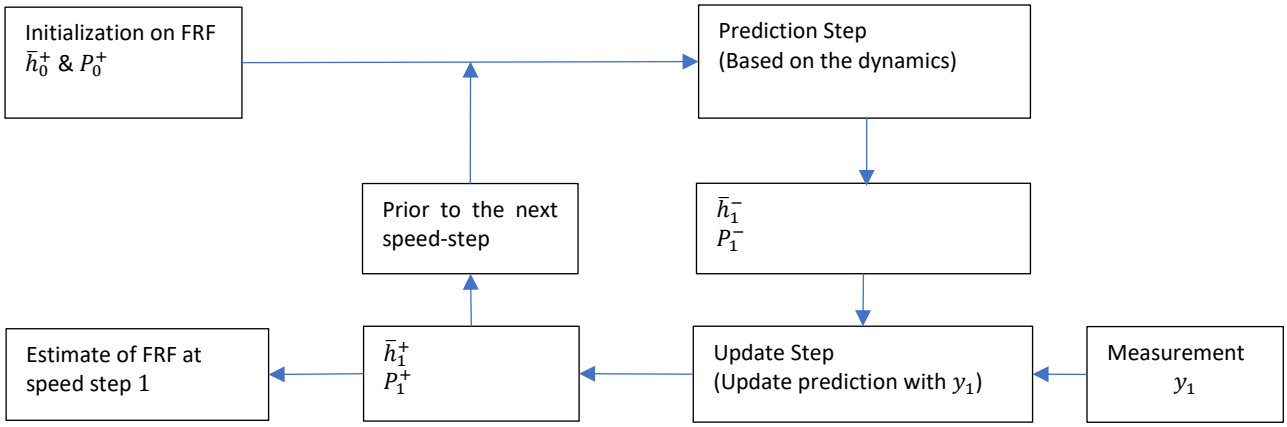

Figure 3.3 Kalman Filter overview of the first loop.

3.2.1 Initialization

The Kalman filter is initialized by assuming the initial estimate of the FRF $\bar{h}_0^+ (n \times 1$ vector). n is the number of frequency bins in the measured dynamic response spectrum. This is because it is convenient to have an FRF (state vector) with the same frequency resolution as the measured dynamic response spectrum. The P_0^+ is the covariance matrix of $n \times n$ dimension of the initial state estimate of the FRF. If the initial state is perfectly known, then $P_0^+ =$ zero matrix. If there is absolutely no idea of the initial state, $P_0^+ =$ identity matrix.

As there is no reasonable initial estimate of the FRF of the synthetic data, the FRF is assumed to be a zero vector with a covariance matrix of unit magnitude. The initial estimate of the FRF and its covariance is given by:

$$\begin{aligned} E(h_0) &= \bar{h}_0^+ = \text{Zero vector} \\ P_0^+ &= E\left(\left(h_0 - \bar{h}_0^+\right)\left(h_0 - \bar{h}_0^+\right)^T\right) = \text{Identity matrix} \end{aligned} \tag{3.3}$$

3.2.2 Prediction step

The initial estimate of the FRF ($\bar{h}_0^+$ and P_0^+) is propagated to the first speed-step using the prediction equations. The prediction equations are given by:

$$\begin{aligned} \bar{h}_1^- &= S\bar{h}_0^+ \\ P_1^- &= SP_0^+S^T + Q \end{aligned} \tag{3.4}$$

where the mean $\bar{h}_1^-$ and the covariance P_1^- is the predicted estimate of the FRF at the first speed-step based on the dynamics of the system. S is the state transition matrix, which defines how the FRF varies with speed**.** As the FRF is independent of speed, S is assumed to be a unit matrix of $n \times n$ dimension. Q is the modelling error covariance matrix. The modelling error covariance matrix represents the uncertainty in the assumed system dynamics, and the calculation of the modelling error covariance is explained in Section 3.2.4.

This reasoning of propagating the initial estimate of the FRF to the first speed-step presented in Equation (3.4) can be extended to obtain the following more general equation at speed-step k:

$$\begin{aligned} \bar{h}_k^- &= S\bar{h}_{k-1}^+ \\ P_k^- &= SP_{k-1}^+S^T + Q \end{aligned} \tag{3.5}$$

3.2.3 Update step

The predicted estimate of the FRF ($\bar{h}_1^-$ and P_1^-) at the first speed-step is updated with noisy measurement data using the update equation. The update equation is given by:

$$\begin{aligned} \bar{h}_1^+ &= \bar{h}_1^- + G_1\left[y_1 - F_1\bar{h}_1^-\right] \\ P_1^+ &= [I - G_1F_1^-]P_1^- \end{aligned} \tag{3.6}$$

where $\bar{h}_1^+$ is the updated estimate of the FRF at the first speed-step and P_1^+ is the uncertainty in the updated estimate of the FRF; F_1 is a diagonal matrix ($n \times n$ matrix) with excitation pulse spectrum at the first speed-step f_1 as the elements of the diagonal matrix. The size of the spall in the bearing is unknown, so the excitation pulse spectrum F_1 which is the function of the size of the spall is taken to be a spectrum of unit magnitude for simplicity of implementation of the Kalman Filter. F_1 is represented by an $n \times n$ unit vector. G_1 is the Kalman gain value given by:

$$G_1 = P_1^-{F_1}^T\left[F_1P_1^-{F_1}^T + R\right]^{-1} \tag{3.7}$$

where R is the measurement error covariance matrix. The measurement error covariance matrix represents the uncertainty in the measured data. The calculation of the measurement error is explained in the next section.

The reasoning in Equation (3.6) and (3.7) can be extended to obtain the following more general update equation at speed-step k:

$$\begin{aligned} \bar{h}_k^+ &= \bar{h}_k^- + G_k\left[y_k - F_k\bar{h}_k^-\right] \\ P_k^+ &= [I - G_kF_k^-]P_k^- \end{aligned} \tag{3.8}$$

$$G_k = P_k^-{F_k}^T\left[F_kP_k^-{F_k}^T + R\right]^{-1} \tag{3.9}$$

3.2.4 Selection of the measurement error and modelling error covariance matrix

In this section, a detailed explanation on the estimation of the modelling error covariance (Q) and measurement error covariance (R) matrices is presented. The variation in the Q and R matrices results in the variation in Kalman gain's value, as seen in Equation (3.9). The diagonal of the R and Q represents the variance at each frequency bin. The off-diagonal elements represent a measure of the variance between two frequency bins.

For the simplicity of the selection of the R and Q, the off-diagonal elements are assumed to be zero. The R is assumed to be $n \times n$ identity matrix multiplied by an integer r. The Q is assumed to be $n \times n$ Identity matrix multiplied by an integer q. The magnitude of the diagonal elements of Q and R is varied by varying the magnitude of q and r , respectively.

$$\begin{aligned} R &= Ir \\ Q &= Iq \end{aligned} \tag{3.10}$$

If the magnitude of the r is high compared to the q, the Kalman gain value is low for the first speed step and reduces to a near-zero value in the second speed-step, as seen in Figure 3.4a. From Equation (3.8), it is seen that, for a near-zero Kalman gain value G_k, the updated estimate $\bar{h}_k^+$ becomes confident on the predicted estimate of the FRF, and the FRF does not learn from the measurement data. Therefore, the estimated FRF is close to the measurement data at the first speed step, as seen in Figure 3.4b.

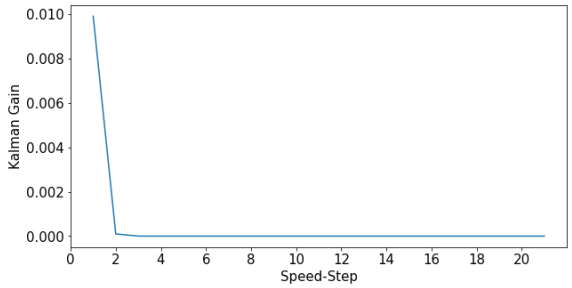

(a) Kalman gain propagation through speed-step.

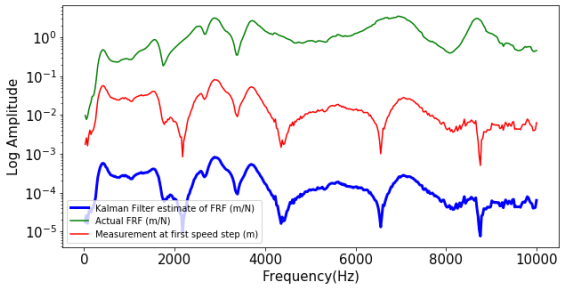

(b) Mean of the FRF of the synthetic data.

Figure 3.4 The Kalman filter estimate of the FRF of the synthetic data for a low Kalman gain value.

If the magnitude of r is low compared to q, it results in a high Kalman gain value, as seen in Figure 3.5a. From Equation (3.8), it is seen that for a high Kalman gain value, the updated estimate $\bar{h}_k^+$ becomes extremely confident on measured signal and would overlearn from the measurement data. The resulting estimate of the FRF is close to the measured data at the last speed step, as seen in Figure 3.5b.

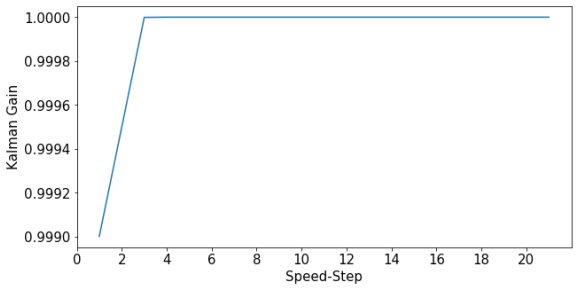

(a)The Kalman gain propagation through speed-step.

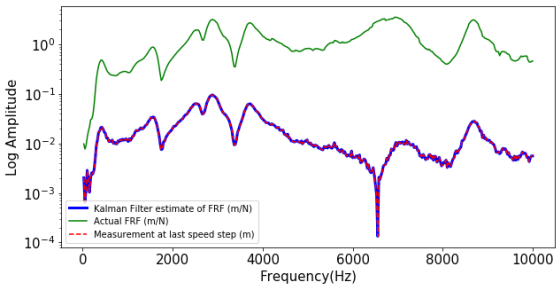

(b) Mean of the FRF of the synthetic data.

Figure 3.5 The Kalman filter estimate of the FRF of the synthetic data for a high Kalman gain value.

To obtain an optimal estimate of the FRF, the magnitude of the q, and the magnitude of the r is varied, such that:

- the estimated FRF is smooth and not overfitting the measurement data.
- the error covariance matrix P_k^+ is reducing after every speed-step. If the covariance matrix P_k^+ is increases after every speed-step, it means that the primary assumption of the Kalman filter is not satisfied. This increase is caused if the initial assumption, modelling error, or measurement error is not correctly defined [31].

The value of q and r was varied in the range of 0 to 100 to obtain an estimate of the FRF, which satisfies the criteria mentioned above. The optimal value of r and q is found to be 1 and 0.01, respectively. As the estimated FRF is not overfitting the measurement data as seen in Figure 3.6a, and the error covariance matrix P_k^+ is reducing with every speed-step, as seen in Figure 3.6b. Therefore, the magnitude of q and r is chosen to be 0.01 and 1, respectively.

Figure 3.6a shows that the amplitude of the Kalman filter estimate of the FRF and the actual FRF is not the same. This is because the f_k is assumed to be a spectrum of unit magnitude and the measurement error to be zero mean, but the magnitude of the f_k is a sinc function with a specific magnitude. The magnitude of f_k is not considered; thus, resulting in the difference in magnitude between the estimated and the actual FRF.

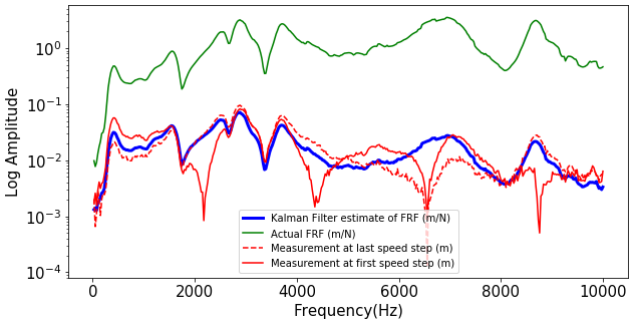

(a) Mean of the Kalman Filter estimate of the FRF.

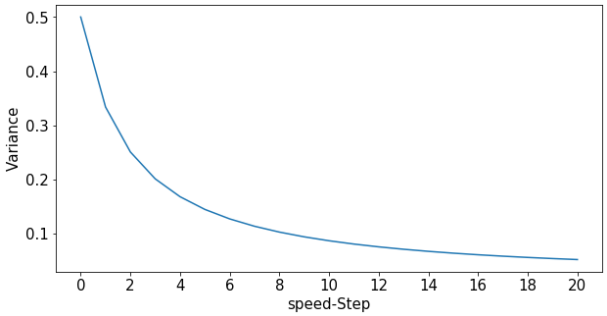

(b)Variance of the Kalman Filter estimate of the FRF.

Figure 3.6 Mean and variance of the Kalman Filter estimate of the FRF when r is 1 and q is 0.01.

3.3 Ensemble Kalman Filter Implementation

In the Ensemble Kalman Filter (EnKF) implementation, the mean and the variance of the state is represented by an ensemble of N<n (n is the number of frequency bins) H_k^{N} [32, 33]. This ensemble (H_k^{N}) is then propagated forward through time and updated when new data become available. In the notation that follows, H_k^{N} is an ensemble of n × N matrix with columns $\left\{h_k^{(i)}\right\}_{i=1}^{N}$.

An overview of the EnKF's process is given in Figure 3.7. The EnKF is first initialized by assuming the initial ensemble of the FRF ($H_0^{\mathrm{N}+}$) before the availability of the measured data at the first speed-step. This ensemble of the FRF ($H_0^{\mathrm{N}+}$) is propagated to the first speed-step using the prediction equations. The predicted FRF is given by $H_1^{\mathrm{N}-}$. The predicted estimate of the FRF ($H_1^{\mathrm{N}-}$) at the first speed-step is updated with noisy measurement data y_1 to obtain an updated estimate of the FRF ($H_1^{\mathrm{N}+}$). This updated estimate at the first speed-step is the initial estimate for the second speed-step. This process of predicting and updating the FRF continues for all the measured data. A detailed description of the assumptions at each step of the EnKF implementation to estimate the FRF is presented in the next subsections.

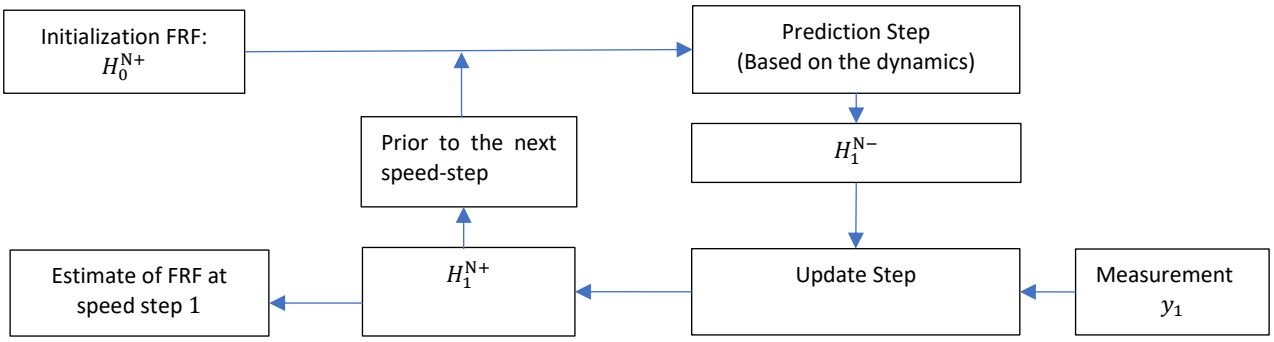

Figure 3.7 Ensemble Kalman Filter.

The ensemble H_k^{N} at the speed-step k is processed such that the mean and the covariance of the ensemble state vector is given by:

$$\bar{h}_k = \frac{1}{N}\sum_{i=1}^{N} h_k^{(i)}$$
$$P_k = \frac{1}{N-1}\sum_{i=1}^{N}\left(h_k^{(i)} - \bar{h}_k\right)\left(h_k^{(i)} - \bar{h}_k\right)^T \qquad (3.11)$$

3.3.1 Initialization

The Ensemble Kalman filter is initialized by assuming the initial estimate of the FRF $H_0^{\mathrm{N}+}$. The ensemble $\left\{h_0^{(i)}\right\}_{i=1}^{N}$ is generated with mean 0 and variance 1, as we do not have a reasonable estimate of the FRF.

$$\left(h_0^{(i)}\right)_{i=1}^{N+} = \mathcal{N}(0,1)$$

3.3.2 Propagation

The initial estimate of the FRF (H_0^{n+}) is propagated to the first speed-step before the availability of the measurement data at the first speed-step using the prediction equation. The prediction equations are given by:

$$H_1^{\mathrm{N}-} = SH_0^{\mathrm{N}+} \tag{3.12}$$

where $H_1^{\mathrm{N}-}$ is the predicted estimate of the FRF at the first speed-step. S is the state transition matrix, which relates how the FRF propagates between speed-steps. As described in section 2.4, the FRF is independent of speed. Therefore, the state propagation matrix S is described by an $n \times n$ identity matrix.

The initial estimate of the state $H_0^{\mathrm{N}+}$ is propagated to speed-step k=1 using the Equation (3.12). This reasoning can be extended to obtain the following more general equation at speed-step k:

$$H_k^{\mathrm{N}-} = SH_{k-1}^{\mathrm{N}+} \tag{3.13}$$

3.3.3 Measurement Update

Next, the predicted estimate of the FRF is updated with the measurement data at the first speed-step to obtain an updated estimate of the ensemble H_1^{N+}. The update equation for the estimation of the FRF is given by:

$$\begin{aligned} Y_1^{N-} &= M_1 \circ H_1^{N-} \\ H_1^{N+} &= H_1^{N-} + G_1(y_1\mathbb{I} - Y_1^{N-}) \end{aligned} \tag{3.14}$$

Where $\mathbb{I} = [1, \ldots, 1]_{1*N}$ is the N-dimensional vector, y_1 is the measured vibration signal at the first speed-step. M_1 is the ensemble of excitation pulse spectra f_1. The notch frequency with uncertainty is estimated from the measured dynamic response spectrum. The uncertainty in the notch frequency is caused by the error in rotational speed and Hertzian contact length. The excitation pulse spectrum is reconstructed from the measured notch frequency. The uncertainty of the pulse spectrum is represented by the ensemble of the pulse spectrum M_1. Where each column of the ensemble of the pulse spectrum $\left\{f_1^{(i)}\right\}_{i=1}^{N}$ represents the excitation pulse spectrum with a notch frequency taken from a normal distribution. G_1 is the Kalman gain value given by:

$$G_1 = P_{H_1^{\mathrm{N}-}Y_1^{\mathrm{N}-}}(P_{Y_1^{\mathrm{N}-}Y_1^{\mathrm{N}-}} + R)^{-1} \tag{3.15}$$

$$P_{H_1^{\mathrm{N}-}Y_1^{\mathrm{N}-}} = H_1^{\mathrm{N}-}(Y_1^{\mathrm{N}-})^T \tag{3.16}$$

$$P_{Y_1^{\mathrm{N}-}Y_1^{\mathrm{N}-}} = Y_1^{\mathrm{N}-}(Y_1^{\mathrm{N}-})^T \tag{3.17}$$

where R is the modelling error covariance matrix. The measurement error covariance matrix represents the uncertainty in the assumed dynamics of the system, and the calculation of the measurement error is explained in the next section.

This reasoning of updating the predicted estimate of the FRF can be extended to obtain the following more general equation at speed-step k:

$$Y_k^{N-} = M_k \circ H_k^{N-} \tag{3.18}$$

$$H_k^{N+} = H_k^{N-} + G_k(y_k\mathbb{I} - Y_k^{n-})$$

$$G_k = P_{H_k^{N-}Y_k^{N-}}(P_{Y_k^{N-}Y_k^{N-}} + R)^{-1} \tag{3.19}$$

3.3.4 Selection of the measurement error covariance (R)

A detailed explanation of the estimation of measurement error covariance matrix (R) is presented in this section. The variation in the magnitude of R results in the variation in Kalman gain's value, as seen in Equation (3.19). The diagonal of the R represents the variance at each frequency bin, and off-diagonal elements represent a measure of the variance between two frequency bins.

For the simplicity of the selection of the R, the off-diagonal elements are assumed to be zero. R is assumed to be a product of $n \times n$ identity matrix and an integer r. The magnitude of diagonal elements of R is varied by varying r.

$$R = Ir \tag{3.20}$$

The high magnitude of the measurement error results in a lower Kalman gain value, as the Kalman gain value is inversely proportional to the measurement error covariance matrix. From equation (3.18), it is seen that for a low Kalman gain value G_k the estimate H_k^{N+} becomes extremely confident on the initial estimate of the FRF, as seen in Figure 3.8.

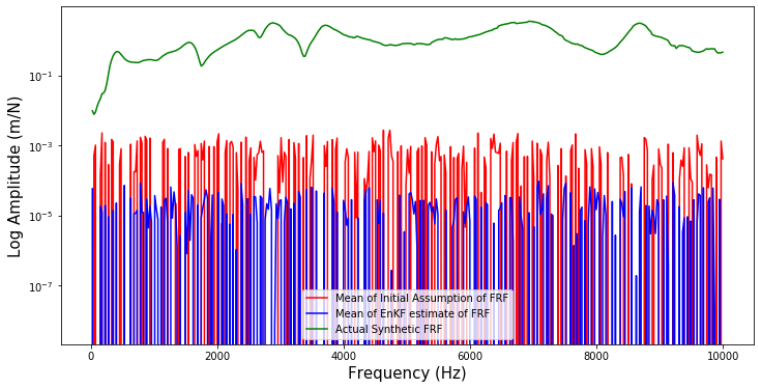

Figure 3.8 The Mean of the EnKF estimate of the FRF of the synthetic data for a high Kalman gain value r=0.1.

The low magnitude of r results in a higher Kalman gain value. For a high Kalman gain value G_k the updated estimate H_k^{N+} becomes extremely confident on measured signal and would overfit to the measured data and noise as seen in the figure below.

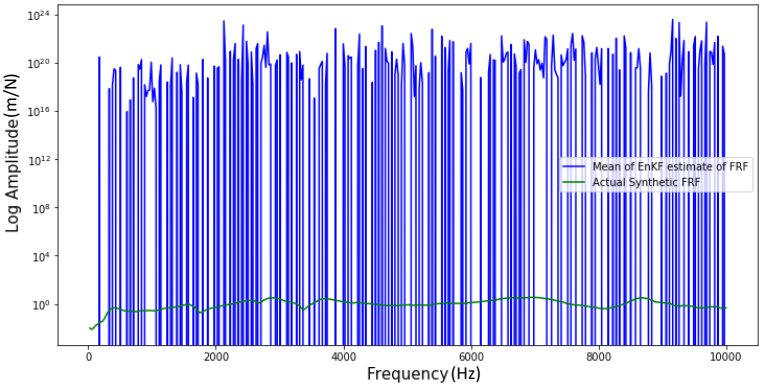

Figure 3.9 The Mean of the EnKF estimate of the FRF of the synthetic data for a low Kalman gain value ($r = 10^{-30}$).

From Figure 3.8 and Figure 3.9, it can be seen that for either a low or a high value of the measurement error, the estimated FRF is extremely noisy. Therefore, the magnitude of r is varied to obtain an optimal estimate of the FRF, such that the estimated FRF is smooth.

When the magnitude of r is 10^{-15}, it can be seen that the estimated FRF is smooth. The estimated FRF has a similar shape (peaks and notches) and magnitude compared to the actual(synthetic) FRF. Thus, based on the smoothness of the estimated FRF, a r value equal to 10^{-15} is chosen for this application to estimate the FRF.

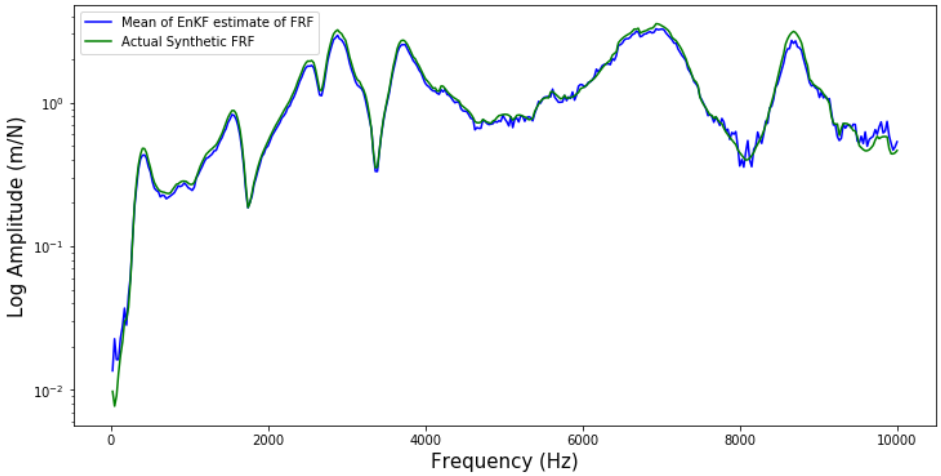

Figure 3.10 FRF estimation from the EnKF when the magnitude r is 10^{-15}

Figure 3.11 shows peaks in the variance of the estimated FRF at specific frequencies. These peaks correspond to the uncertainty induced into the estimated FRF due to the notches in the measured dynamic response caused by the excitation pulse. The peaks caused by the notches of the latest measurement data are more prominently seen because the peaks (uncertainty) caused by the notches of initial measurements have reduced through the recursive process of the EnKF implementation, as shown in Figure 3.12.

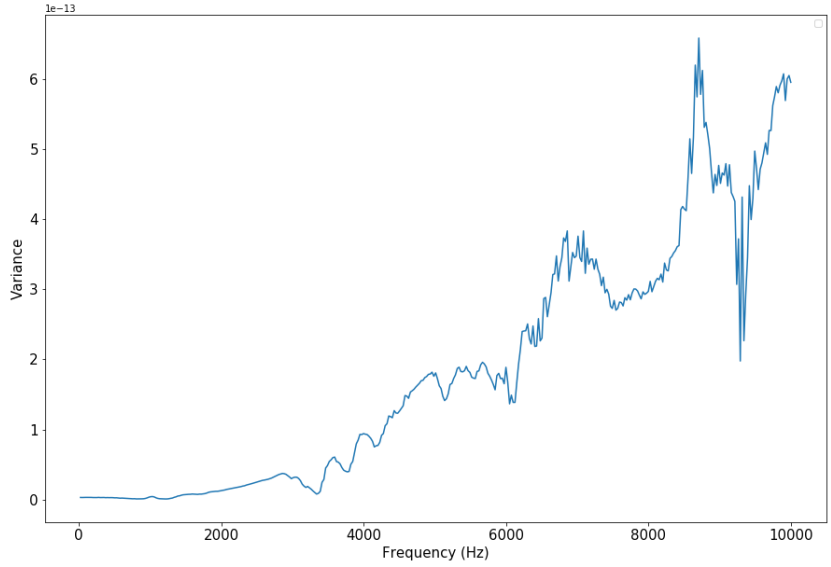

Figure 3.11 Variance of the estimated FRF of the FRF using EnKF implementation

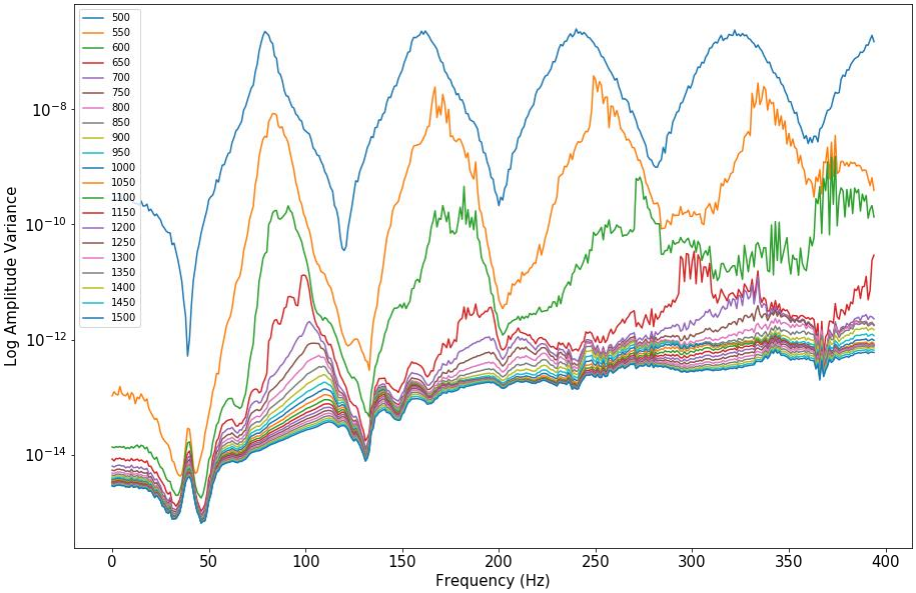

Figure 3.12 Propagation of the Variance of the estimated FRF at every speed-step

4 Experimental Setup and Signal processing

In this chapter, the steps involved in measuring the defective bearing's vibration response are presented in section 4.1, and the processing of the measured vibration response to extract the dynamic response of the bearing to the rolling-element moving over the spall is presented section4.2.

4.1 Defective bearing's dynamic response measurement system

The steps involved in preparing a defective bearing to measure the vibration response are:

1. Sample preparation: The defective bearings were prepared with artificial rectangular spalls of different sizes on the bearing's outer-ring.
2. Experimental setup: An experimental setup is developed to rotate the bearing at different speeds and loading conditions.
3. Vibration response recordings: A measurement system is developed to record the bearing's vibration response at different rotational speeds and loading conditions.
4. Experiment Plan: It is done to validate the theory presented in Chapter 2 and Chapter 3.

4.1.1 Sample preparation

The bearings used in this research work for testing are 6206 ETN9/C3 deep groove ball bearing (see Figure 4.1a). The 6206 bearing is selected as it has a polymer cage. A polymer cage facilitates the disassembly of a bearing without damaging the bearing. A disassembled 6206 bearing is shown in Figure 4.1b.

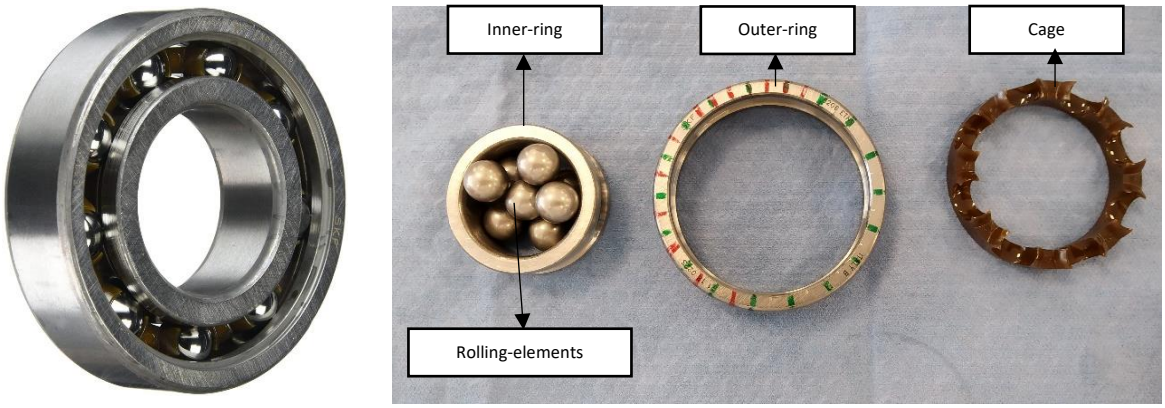

(a) 6206 ETN9/C3 deep groove ball bearing.

(b) Disassembled 6206 ETN9/C3 bearing.

Figure 4.1 Assembled and disassembled 6206 ETN9/C3 bearing.

A 6206 ETN9/C3 bearing is referred to as a 6206 bearing in this report for convenience. The specifications of the 6206 bearings are presented in the table below:

Table 1 bearing data

Number of rolling element	8
Pitch diameter	46.2 mm
Rolling-element diameter	11.112 mm
Inner-ring groove radius	5.67 mm
Outer-ring groove radius	5.894 mm

The bearing is disassembled to make rectangular-shaped spalls on the surface of the outer-ring. A grinding process is used to make the rectangular-shaped spalls. The rectangular spall profile is calculated and generated based on the bearing's pitch diameter, outer ring groove radius, and spall length in the rotation direction [34]. The profile is then read into the CNC grinding machine to engrave the spall on the outer-ring. Figure 4.2 represents the CNC grinding machine used to make the spall on the bearing.

Figure 4.2 CNC grinding machine.

Figure 4.3 shows the 3mm and 5mm spalls engraved on the outer-ring of a bearing using the CNC grinding machine. The CNC grinding system is based on three actuators, two linear (X-axis and Y-axis) and one rotating actuator (Rotation Vice). The workpiece (the outer-ring to be modified) is mounted on the rotation vice and rotated with a precision motor. This rotation forms the 1st degree of freedom of the CNC grinding tool. The X-axis actuator has a stroke length of 100mm (2nd degree of freedom), and the Y-axis actuator has a stroke length of 200mm (3rd degree of freedom). The X-axis actuator and the Y-axis actuator moves the grinding head in the two linear degrees of freedom.

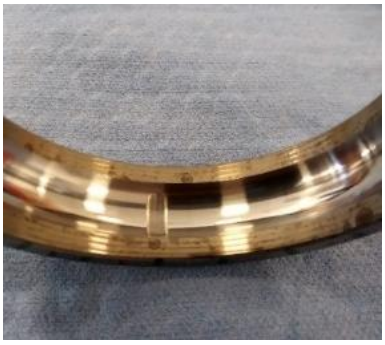

(a) 3mm spall

(b) 5mm defect

Figure 4.3 Large surface artificial spall on the outer-ring of a 6206 bearing.

Small-spalls of 0.1mm, 0.25mm & 0.5mm in the direction of the rotation were outsourced due to the grinding tool's precision constraints. The bearing's profile with 0.1mm & 0.5mm spalls is shown in Figure 4.4.

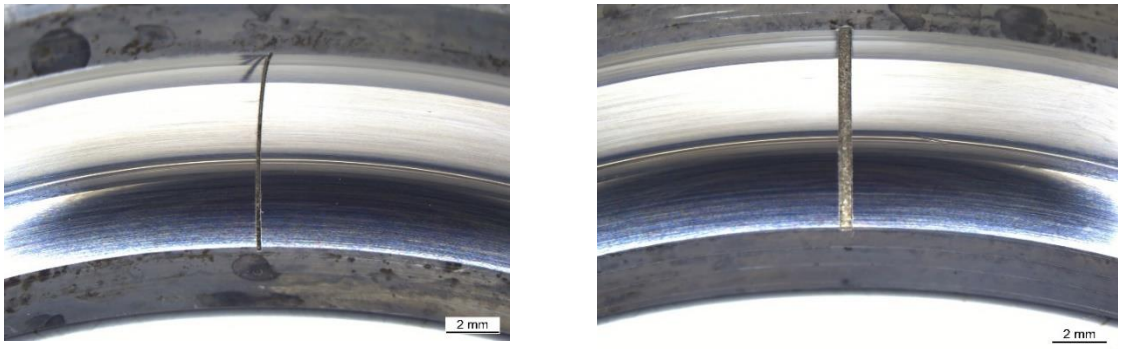

(a) 0.1mm spall.

(b) 0.5mm spall.

Figure 4.4 Small Spalls on the outer-ring of the bearing.

The high pressures at the contacts of the rolling-element and the raceway of the axle bearings do not allow much deviation from the ideally smooth surface in a bearing; any small debris caused by the grinding process would damage the bearing and cause additional vibration. To remove the debris caused by the grinding process, the outer ring is cleaned by placing it in an ultrasonic bath for 10 minutes. An ultrasonic bath uses cavitation bubbles induced by high-frequency waves to agitate a liquid. This agitation produces high forces on debris adhering to the surface of the outer-ring of a bearing, thus removing the adhering debris and the lubrication from the outer-ring's surface.

The rolling-element, the outer-ring, the inner-ring, and the cage are assembled. After the ultrasonic bath, the bearing is lubricated again with oil shell T32, as the ultrasonic bath would have removed the lubrication of the bearing.

4.1.2 Experimental setup

The bearing with a spall engraved on the outer ring is placed in a housing. The housing is designed to fit two 6206 bearings. Therefore, bearing with a spall is coupled with an outer-ring of a 6206 bearing. The outer-ring of a 6206 bearing is used as a filler sleeve to fill the housing gap, as seen in Figure 4.5a. A mandrel is connected to the defective bearing's inner ring and then placed inside a housing with a filler sleeve, as shown in Figure 4.5b.

(a) Housing with filler sleeve.

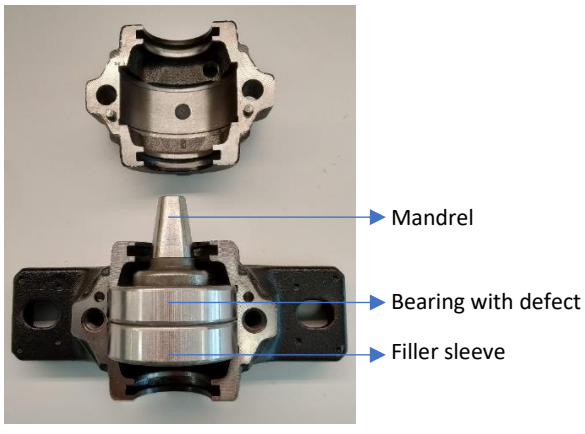

(b) Housing with filler sleeve, defective bearing, and mandrel.

Figure 4.5 Housing and defective bearing integration.

The housing with the defective bearing is connected to the motor, as shown in Figure 4.6. The flexible-clutch connects the mandrel from the housing to the motor. Thus, the motor drives the bearing's inner

ring, and the outer ring of the bearing is kept constant. The flexible-clutch is used between the housing and the motor because:

- the flexible clutch intercepts any possible misalignment between the motor shaft and the mandrel shaft.
- the aluminium 'U' profile of the flexible clutch holds two high precision bearings that allow a high vertical load on the housing without damaging the drive motor's air spindle.

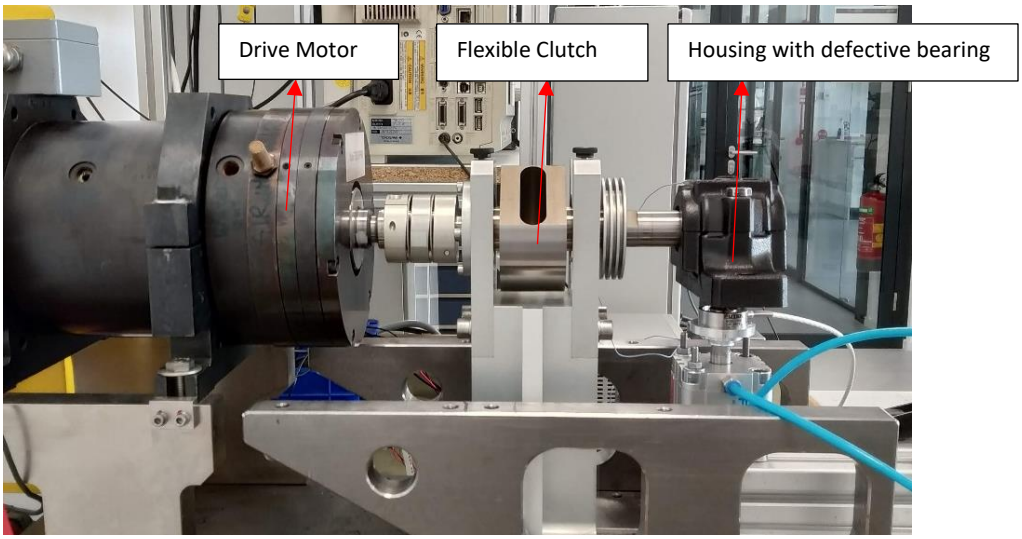

Figure 4.6 VKL experimental setup.

The flexible-clutch is integrated into the shaft of the drive motor. An air bearing supports the shaft of the drive motor. The advantages of using air bearing are that it reduces the shaft vibration and allows high rotational speed. The air bearing pressure is controlled using an air pressure adjustment valve (Festo) installed under the table.

A control system is developed to control the rotation speed of the motor. An IMC C-SERIES data acquisition system is calibrated to control the rotational speed and the duration between the speed change. The IMC C-SERIES device is programmed using the IMC software. The software takes in two inputs:

1. Speed iteration: it is a column vector with the list of speeds that the motor should run.
2. Duration: the duration time between the change of speed.

The IMC C-SERIES device controls the drive motor's speed by varying the supplied DC voltage to the ABB frequency controller. The ABB frequency controller is the interface between the IMC C-SERIES and the motor.

An axial point load is applied to the bearing using a double-acting compact Festo pneumatic cylinder, as seen in Figure 4.7b. A pneumatic cylinder is a mechanical component that uses compressed gas to produce force through the piston rod in only one direction. The force at the piston rod in the pneumatic cylinder depends on the pressure in the cylinder. The piston rod transfers the force it develops to the housing of the defective bearing.

A pneumatic cylinder is used because the test rig already had connections for an air pressure line and a pressure valve to control the pressure. The pressure in the air pressure line is controlled with the air pressure adjustment valve (Festo) installed under the table, as seen in Figure 4.7a.

A load cell is placed between the piston rod and the defective bearing's housing, as shown in Figure 4.7b. The load cell applies a point load to the center of the defective bearing's housing base. This load

cell is connected to the IMC device, and with the help of the IMC software, the applied force is recorded.

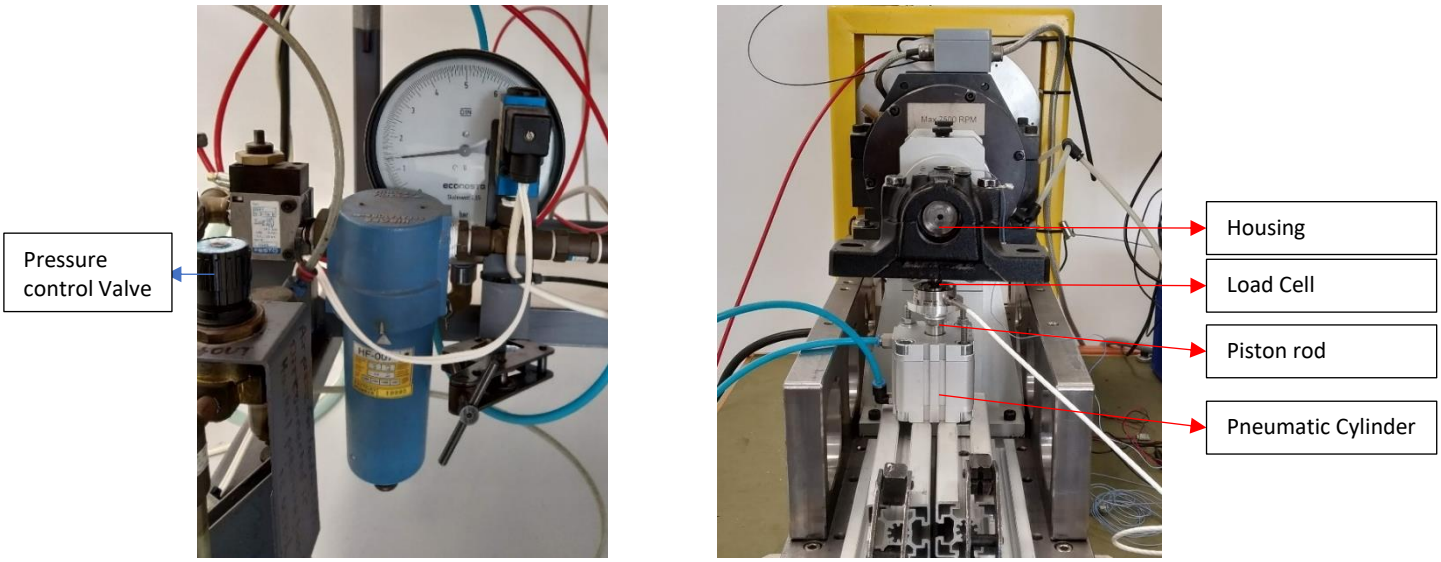

(a) Axial load air pressure control unit. *(b) Axial load on the housing.*

Figure 4.7 Axial loading system.

4.1.3 Vibration response measurement

The data acquisition is carried out with the accelerometer connected to a Yokogawa DL750 oscilloscope. The accelerometer is placed on top of the housing, as shown in Figure 4.8. The accelerometer is connected to a 701251 channel analog plugs of the Yokogawa DL750 oscilloscope.

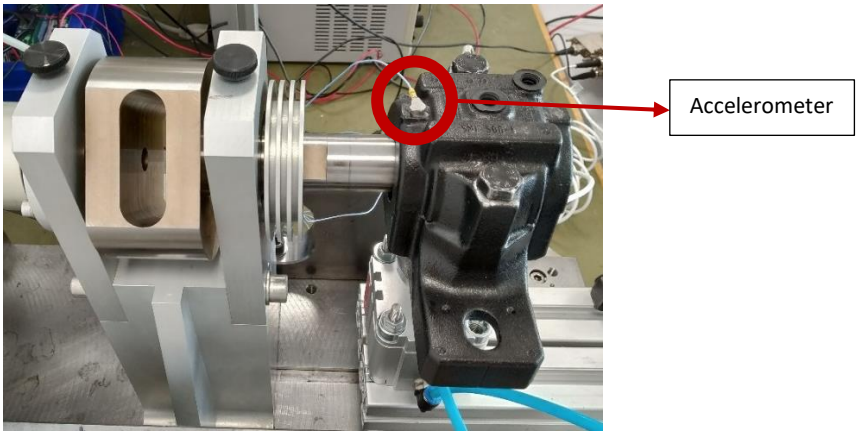

Figure 4.8 Accelerometer placement.

The Yokogawa DL750 is triggered by the IMC device to record the vibration signal from the accelerometer. The IMC is connected to trig-in (on the left panel of the oscilloscope) of the Yokogawa DL750. The IMC software programmed to control the speed is also programmed to trigger the Yokogawa recorder 30 seconds after the motor changes' its rotational speed. This is because the motor requires approximately 30 seconds to stabilize after the speed change. The IMC device triggers the Yokogawa recorder by sending a pulse to the Yokogawa recorder.

The Yokogawa records the vibration signal at a frequency of 10^5 Hz, and the recording length is 10^6 samples. The record length is constant with varying speed because the IMC device used to control the speed and trigger the recording cannot control the record length. This is because the Yokogawa DL750 does not have an option to use an external device to control the record length. As a consequence of

keeping the record duration constant, the total energy of the measured vibration response of a defective bearing increases with speed. This is because the number of excitations increases with increasing speed, causing the measurement signal's total energy to increase.

4.1.4 Experiment plan

The experimental setup has three control variables:

- Defect size in the running direction.
- Rotational speed.
- Radial load.

Defect size in the running direction: The spall engraved on the bearing's outer ring is rectangular. This rectangular shape makes the leading edge of the spall the same as the lagging edge. This makes the test insensitive to the rolling direction.

All spalls are engraved on the outer-ring as the spall's location is constant with respect to the location of the sensor. The amplitude and phase of the FRF change if the spalls are engraved on the inner-ring or the rolling-element, as the location of the spall is changing with respect to the sensor. Therefore, all spalls are engraved on the outer-ring of the bearing to maintain a constant amplitude and phase of the FRF.

The defect size is varied from small spalls (see Section 2.2.1) to larger spalls (see Section 2.2.2). This variation will validate the analytical approximation explained in Section 2.2. The experiments planned shall reveal how the frequency content of the bearing's vibration response varies with the size of the spall.

Rotational speed: The speed capability of the drive motor limits the bearing's rotational speed variation. The minimum stable speed is found to be approximately 500RPM, and the maximum speed is 1500RPM with a variation of approximately $\pm$10RPM. The speed is increased linearly in steps of 50RPM. The experiments planned shall reveal how the vibration response's frequency content varies with speed, as explained in Chapter 2. This speed variation is needed to extract the FRF using the methods developed in Chapter 3.

Radial load: The load capability of the drive motor limits the bearing's rotational speed variation. 600N is the maximum axial load that can be applied to the bearing without damaging the drive motor. Therefore, the load range is from 300N to 600N in the steps of 100N.

The stiffness increase is 10^{-7} m^{-1} (from simpro simulation) for a 100N increase in the load, and the mass of the 6206 bearings is 0.2kg. As the stiffness increase is negligible compared to the bearing's mass, the FRF's shape is expected to remain the same. The fact that the FRF remains constant is used to validate the methods proposed to estimate the FRF of the defective bearing.

4.2 Signal processing

In this section, the steps involved in the pre-processing and post-processing of the vibration signal of a defective bearing to extract the bearing's dynamic response to a cyclo-stationary force pulse produced by the rolling-element moving over a spall explained. The dynamic response of a bearing to the cyclo-stationary force pulse is required to estimate the FRF of the bearing using the methods presented in chapter 3.

First the steps involved in pre-processing the raw vibration signal of the defective bearing are explained. Later, the technique used to extract the dynamic response is presented.

4.2.1 Pre-processing of the vibration signal

The vibration signal is normalized with speed to filter the global change in the vibration response's energy due to speed variation. This research aims to extract the FRF, which is independent of speed. Therefore, it is crucial to filter the increase in energy as a consequence of the speed. The energy of the vibration response of the defective bearing changes with speed because for two reasons:

1. The duration of the recording of the vibration response is constant (10s); therefore, increasing speed results in an increase in the number of rolling-element and spall interactions in the recording period. The increase in the number of excitations with increasing speed results in an increase in the energy of the vibration signal.
2. The vibration sensors measure the acceleration of the outer ring, and the acceleration of the outer-ring at the location of the sensor is given by the equation:

$$\frac{d^2y}{dt^2} = -\omega^2 \, \mathrm{r} \cos(\omega t) \cos(\pi - \alpha) \tag{4.1}$$

where ω is the angular velocity of the inner ring of the bearing; α is the smallest angle between the sensor and the spall; y is the displacement of the outer-ring of the defective bearing at the location of the spall. From equation (4.1), it is seen that the amplitude of the acceleration signal increases with the square of the amplitude of angular velocity (ω^2) with an increase in speed.

To filter the change in the energy of the vibration response as a consequence of change number of excitation pulse in the signal, the measured vibration signal's duration is varied to contain a constant number of excitation pulses. The number of the pulse generated at the minimum speed (500 RPM) is taken as the maximum number of pulses that all the reading can contain to maintain constant energy. At 500RPM, the measured signal contains 250 excitations in 10 seconds. Every measurement's duration is varied (reduced) by taking only a part of the measured signal to contain precisely 250 excitations to maintain constant energy in the signal.

To filter the change in the energy of the vibration response as a consequence of a change in the amplitude of the vibration signal (acceleration signal). The measured signal is divided by the square of the amplitude of angular velocity (ω^2). Dividing the signal with ω^2 is equivalent to integrating the measured acceleration signal twice, resulting in the displacement of the outer-ring at the location of the sensor, and the displacement is given by:

$$\mathrm{y} = \mathrm{r}\cos(\omega t) \cos(\pi - \alpha) \tag{4.2}$$

Figure 4.9 shows the normalized vibration response signal over different rotational speeds. It can be seen that the normalized vibration response signals are not entirely overlapping in amplitude; this is a consequence of an error in the rotational speed of the bearing.

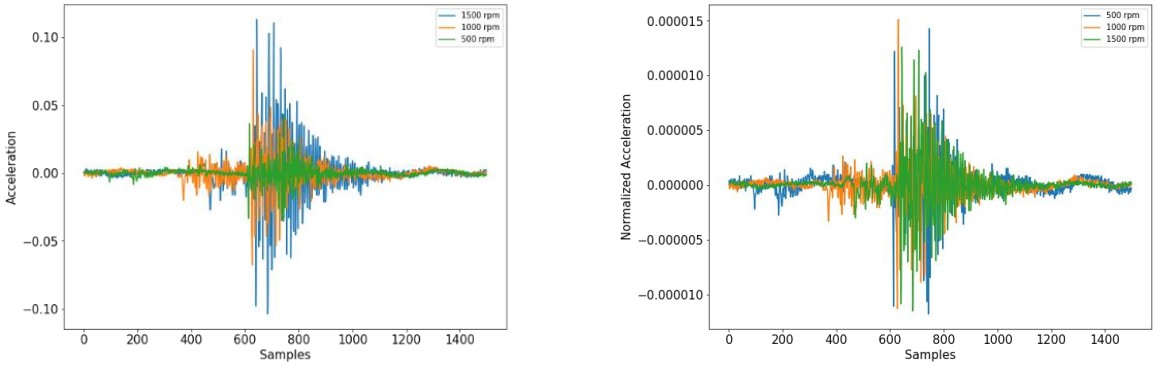

(a) Acceleration vs sample.

(b) Normalized acceleration vs. samples.

Figure 4.9 Response of a defective bearing.

4.2.2 Post-processing to extract the dynamic response

The Repetitive Fourier Transform (RFT) technique is used to detect the pulse that manifests itself at specific repetition frequencies. The dynamic response of bearing to a rolling-element moving over a spall has a specific repetition frequency. Thus, an RFT technique is used to extract the repetitive frequency.

In reference [5], this method was implemented to extract the dynamic response of the bearing in the frequency domain to a rolling-element rolling over spall. Reference [39, 40] proposed similar methods to extract the dynamic response of a bearing to a rolling element moving over a spall. RFT is a two-step process; first, the time signal is transformed into a time-frequency signal using Short-Time Fourier transform, next the time-frequency signal is transformed to a frequency-frequency signal using Fourier transform.

Step1: Short-Time Fourier Transform (STFT)

The pre-processed vibration response of the bearing $y(t)$ is a time-discrete signal. A Short Time Fourier transform is applied to the signal $y(t)$ to obtain a time-frequency spectrum. This spectrum is the collection of regularly spaced time-frequency signals $y(\tau, \omega_N)$, represent the amplitude of the vibration signals as a function of time and frequency.

The spectrum is obtained by sliding a window $w(t)$ over the time signal $y(t)$. After this, the frequency spectrum at each position τ is obtained by Fourier transforming the section of signal that lies in the window, and this results in the spectrogram given by:

$$y(\tau, \omega_l) = \mathcal{F}\big(y(t)\omega(t-\tau)\big) \tag{4.3}$$

In which ω_l is the index of the frequency within the frequency spectrum of the window with length l. The frequency resolution of the STFT depends on the sampling frequency and window length. The window length l is a compromise between the frequency resolution and the blurring in the spectrogram's time domain.

The optimal window length should be smaller than the repetition time t_{ord} of the repetitive excitation pulse of the defective bearing to avoid the blurring of the time-frequency signal. With the increase in speed, the duration between consecutive pulses will reduce. Thus, the optimal window length of the STFT will reduce with speed.

As the bearing's sampling frequency is constant for all the speeds, the time-frequency spectrum at higher speeds has a lower frequency resolution. To simplify the implementation of the methods presented in Chapter 3, it is vital to maintain a constant frequency resolution of the STFT at all speeds.

The largest window size applicable for all speeds without the loss of the spectrum's time resolution is the optimum window size at the bearing's highest speed. The highest speed of the bearing for this experimental setup is 1500RPM; the window length of the STFT is calculated for 1500RPM and kept constant for all the speed to maintain a constant frequency resolution.

Figure 4.10 shows an example of the STFT of the pre-processed vibration response of 6206 deep groove ball bearing with a 3mm spall on the outer-ring with the bearing rotating at 500RPM. From the spectrum, the dynamic response of bearing to the repetitive excitation pulse caused by the rolling-element moving over a spall is seen along the vertical axis with a repetition frequency of approximately 25Hz.

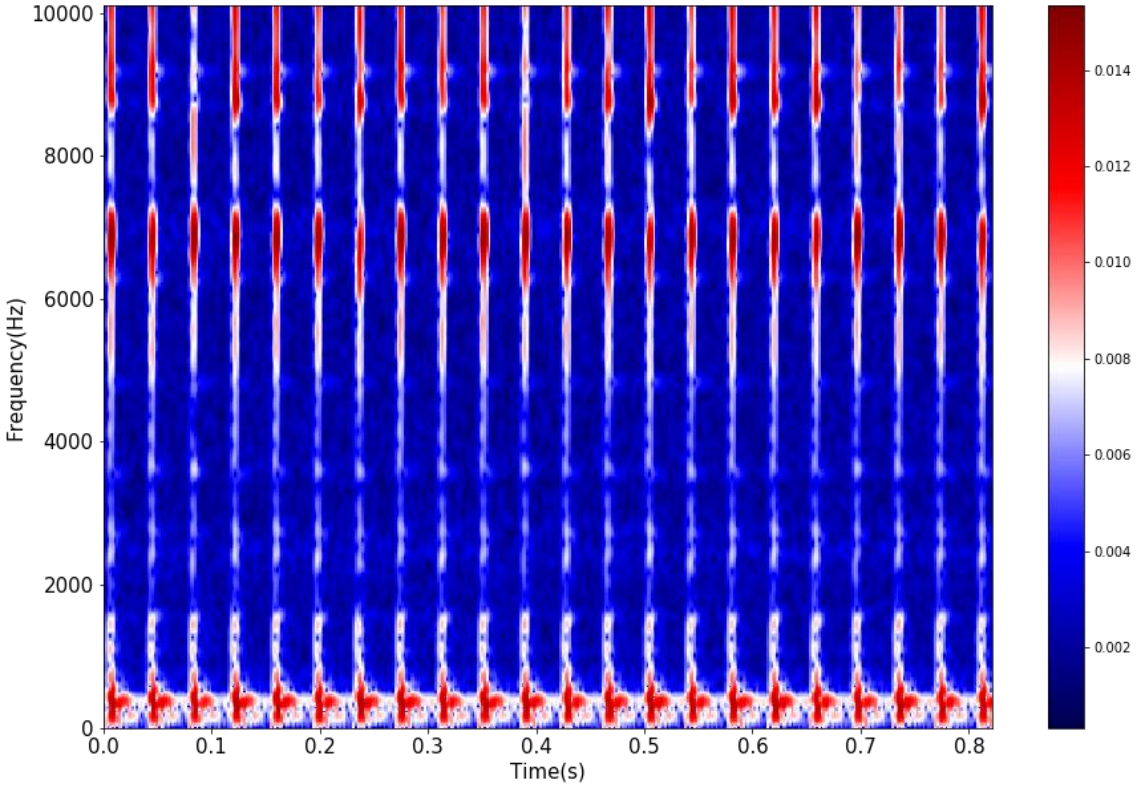

Figure 4.10 STFT of a defective bearing with 3mm spall on the outer-ring

Step2: Fourier transfer

For a defective bearing, typical repetition frequencies are outer-ring defect frequency, inner-ring defect frequency, and rolling-element defect frequency (see section2.4). To detect these typical repetitive excitations of the defective bearing from the measured time-frequency spectrum, a second Fourier transform is applied to the time-frequency spectrogram obtained in the previous step with respect to the time position τ:

$$y(\omega_{rep}, \omega_N) = \mathcal{F}(y(\tau, \omega_N))$$

where ω_{rep} is the repetition frequency and $y(\tau, \omega_N)$ is the STFT of the time signal $y(t)$.

The energy of all the non-repetitive components of signals is put at a repetition frequency of zero. This is a clear advantage of the RFT since all background signals, which have a non-repetitive signal contents, are 'filtered out'. The RFT only presents the elements of the signal, which consists of pulses with a repetitive character. In Figure 4.11a, the response of a bearing to the pulses generated as a consequence of a rolling-element moving over a spall can be seen as lines at multiples of the repetition frequency, which is 25Hz for an outer-ring defect of a 6206 bearings.

Figure 4.11b is the cross-section of the RFT integrated RMS-wise over all of the excitation frequency. The actual repetition frequency of the excitation pulse is the frequency at which the energy in Figure 4.11b is reaching its first maxima.

Based on the extracted repetition frequency, the dynamic response is extracted from the frequency-frequency RFT spectrum. The cross-section of the RFT is taken at the extracted repetition frequency. Figure 4.11c represents the pulse spectrum extracted at the actual repetition frequency from the spectrum calculated using the RFT of a 6206 bearing with a 3mm defect on the outer ring.

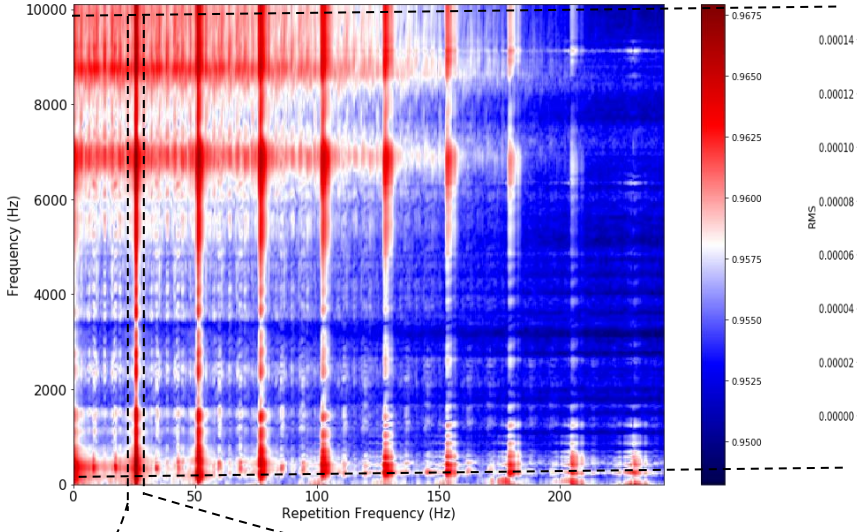

(a) RFT spectrum

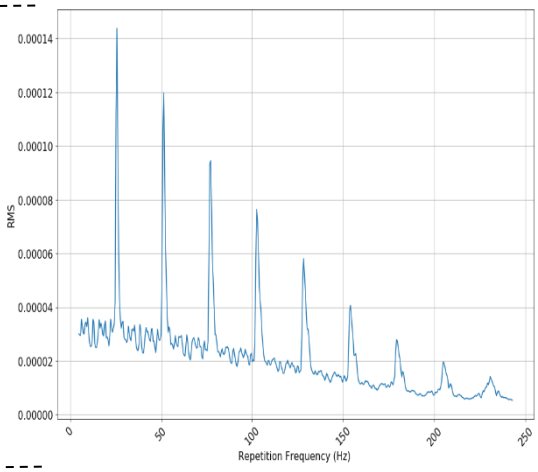

(b) Envelop spectra of the RFT

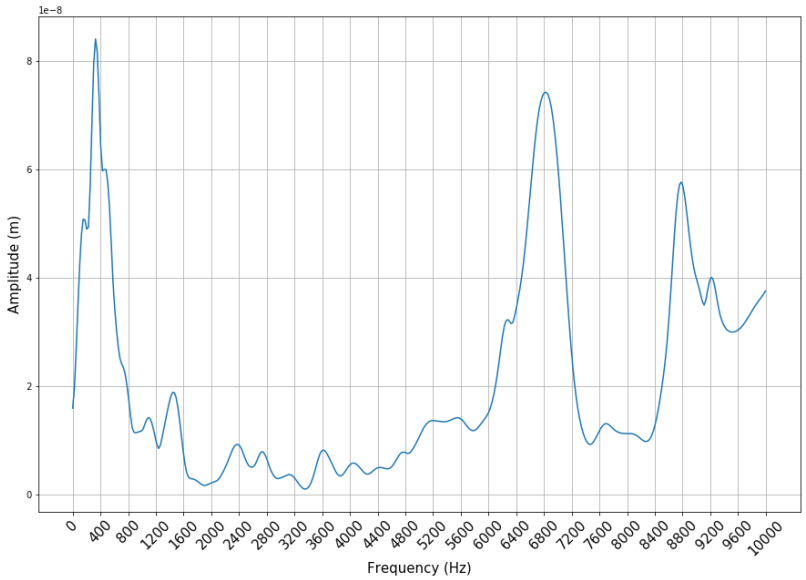

(c) Excitation pulse spectrum extraction

Figure 4.11 Excitation pulse spectrum extraction

5 Results and discussion

In this chapter, the theory on the vibration response of the bearing in the time domain to a rolling-element moving over a small and a large spall is discussed and validated using the experimental data in Section 5.1. Similarly, the theory on the vibration response of the bearing in the frequency-domain is discussed and validated using the experimental data in Section 5.2. Next, the results of the three methods developed in Chapter 3 to estimate FRF from the measured vibration response of the bearing are discussed in Section 5.3. The chapter then concludes by comparing the three methods developed to estimate the FRF of a defective bearing in Section 5.4.

5.1 The time-domain vibration response

Figure 5.1 represents the time-domain vibration response of rolling-element moving over a small spall (0.25mm) located on the 6206 bearing's outer-ring. From the figure, it can be seen that the rolling-element moving over a small spall results in a single pulse, as explained from a theoretical perspective in Section 2.2.1.

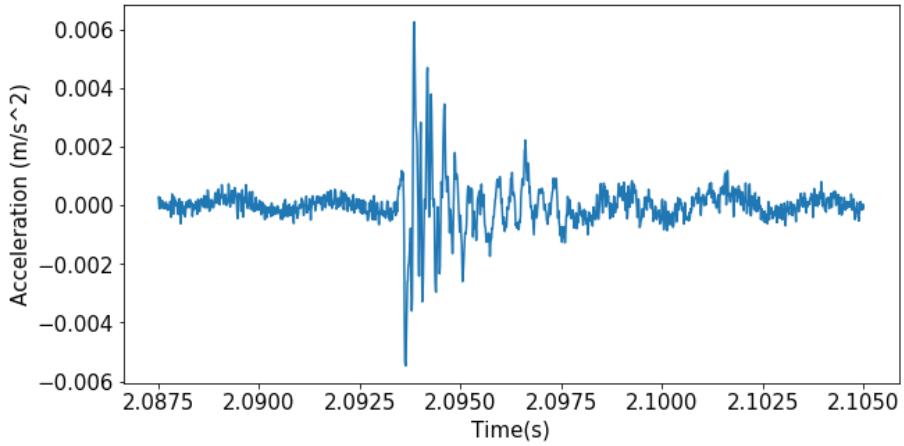

Figure 5.1 Vibration response of a small spall (0.25mm) rotating at 1000RPM.

Figure 5.2 represents the time-domain vibration response of rolling-element moving over a large spall (8mm) located on the bearing's outer-ring. Figure 5.2 shows that the rolling-element moving over a large spall result in two events, the first event originating from the entry of the rolling-element into the spall (de-stress), and the second event due to the departure of the rolling-element from the spall (re-stress), as proposed in a theoretical perspective in Section 2.2.2.

During the entry phase, a gradual de-stressing of the rolling-element into the spall is seen between point 'a' and point 'b' of Figure 5.2. After the de-stressing of the rolling element into the spall, the contact between the rolling-element and spall is released, and the vibration response of the bearing to this event is seen between point 'b' and point 'c' of Figure 5.2. During the leaving phase, the rolling element strikes the edge of the spall at the exit and excites the bearing's high-frequency resonance modes, as seen at point 'c' of Figure 5.2. Next, the rolling element re-stresses between the raceways at the edge of the spall to its normal load-carrying capacity. The vibration response to the re-stressing of the rolling element to its normal load-carrying capacity is seen at point 'd' in Figure 5.2.

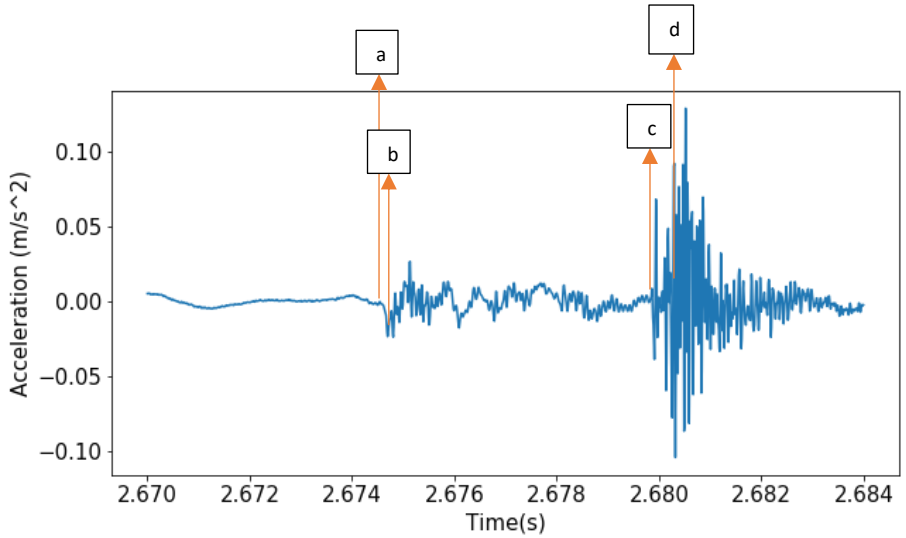

Figure 5.2 Vibration response of large spall (8mm) rotating at 1000RPM.

Figure 5.3 and Figure 5.4 shows the vibration response of a bearing rotating at a speed of 1000RPM over a period of five rotations with small (0.25mm) and large (8mm) spalls, respectively. It can be seen that the amplitude of the vibration response varies with time; this is because of the shape deviation (rolling-element and inner-ring) of the bearing from its perfectly round shape and the variation in the rotational speed of the bearing.

The shape deviation of the inner-ring and the rolling-element is due to the tolerance in bearing manufacturing and the defective bearing preparation process. This shape deviation changes the bearing's contact forces between each rolling-element and the raceway. Therefore, the bearing's load distribution varies with time and results in the variation of vibration response's amplitude.

The experimental setup has a variation of approximately $\pm$10RPM. The variation in the rotational speed results in the variation of the amplitude of acceleration signal response to the rolling-element moving over the spall. From equation (4.1), it is seen that the amplitude of the acceleration signal changes with the square of the amplitude of angular velocity (ω^2).

Therefore, due to the shape deviation and variation in the rotational speed, the amplitude of the defective bearing's acceleration signal varies with time.

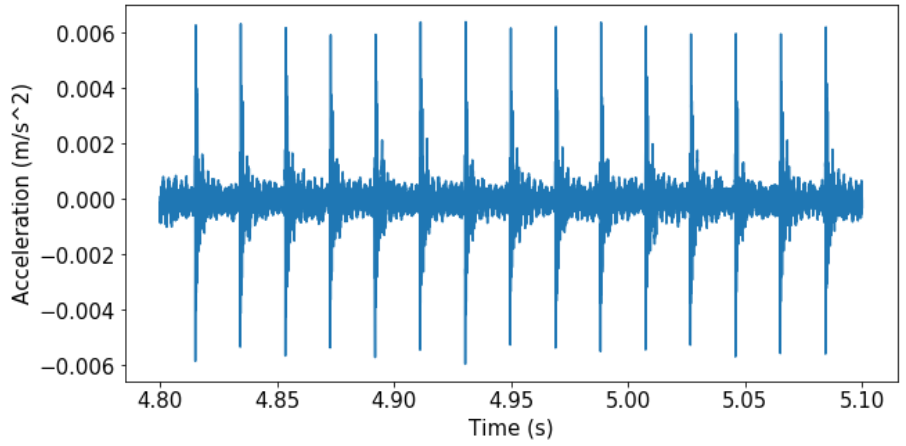

Figure 5.3 Vibration response of a bearing with small spall on the bearing's outer-ring.

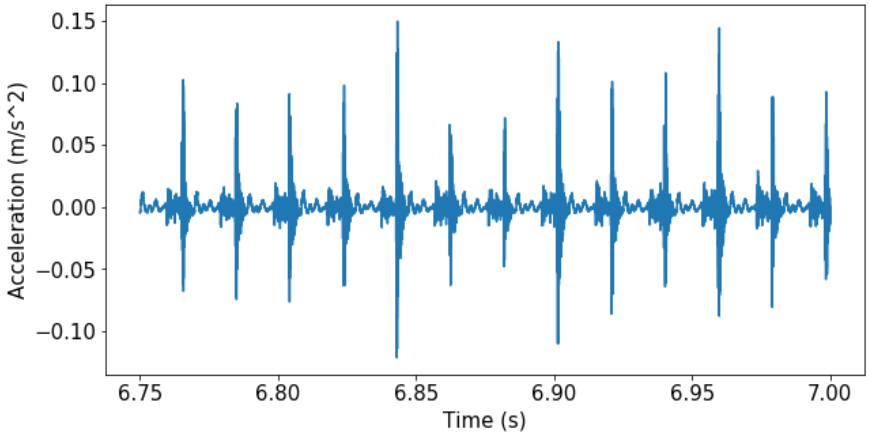

Figure 5.4 Vibration response of a bearing with large spall in the bearing's outer-ring.

The frequency at which the excitation pulse repeats itself depends on the type of the bearing, the rotational speed of the bearing, and the location of the spall (inner-ring, outer-ring, and rolling element). During this thesis, the experimental work is done on a 6206 bearing with an outer-ring spall. Therefore, the repetition frequency depends on the bearing's rotational speed, as the type of bearing and location of the spall remains constant throughout the experimental work.

The theoretical repetition frequency of the excitation pulses is calculated using Equation (2.26) for the defective bearing at the speed at which the experimental setup was set during the recording of vibration data. The actual repetition frequency of the excitation pulse of the experimental vibration response of the defective bearing is estimated, as explained in Section 4.2.

Figure 5.5 shows the difference between the actual repetition frequency and the theoretical repetition frequency for a bearing with 0.25mm spall. This difference between the actual and the theoretical is in the range of $\pm$0.6Hz.

A difference between the theoretical repetition frequency and the actual repetition frequency is because the experimental setup has a variation of approximately $\pm$10RPM. Based on the theory presented in Section 2.5, a variation of $\pm$10RPM in the rotational speed results in a variation of $\pm$0.55Hz in the repetition frequency of the excitation pulse.

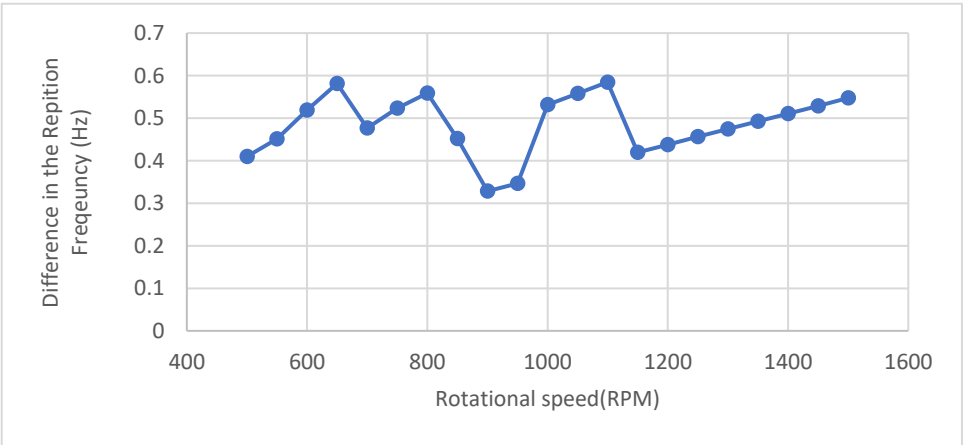

Figure 5.5 Error in repetition frequency as a function of speed.

5.2 The frequency-domain vibration response

In this section, the theory on the vibration response of a bearing in the frequency-domain with small and large spalls is validated with the experimental vibration response of a bearing with 0.25mm (small) and 8mm (large) spalls on the bearing's outer ring.

Figure 5.6 compares the excitation pulse spectrum and dynamic response spectrum to a rolling-element moving over a 0.25mm spall located on the bearing's outer-ring. The excitation pulse spectrum is analytically calculated using Equation (2.8) and Equation (2.16) for a bearing with 0.25mm outer-ring spall. The Repetitive Fourier transform technique (presented in Section 4.2) is used to extract the dynamic response spectrum from the measured vibration response of a bearing with 0.25mm spall on the bearing's outer-ring.

Figure 5.6 shows a small variation between the notch frequency of the analytical excitation pulse spectrum and the notch frequency of the measured dynamic response spectrum. This variation is explained in detail in the latter part of this section.

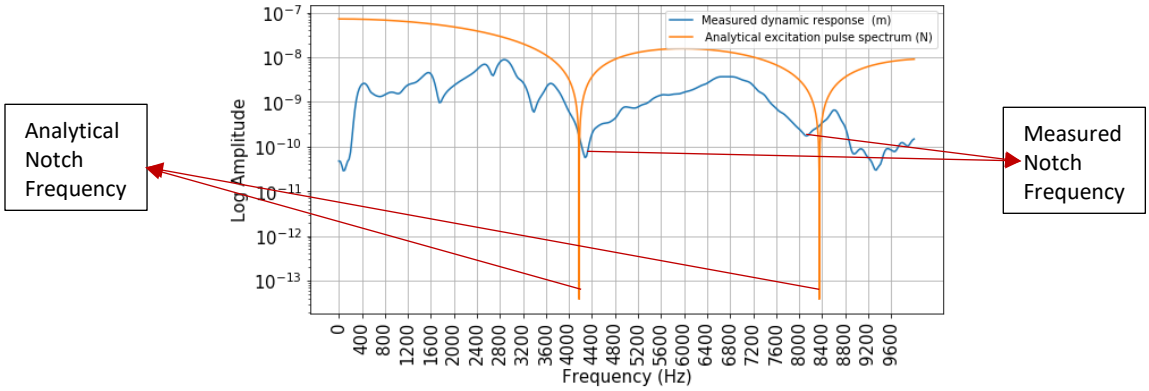

Figure 5.6 Dynamic response of the bearing with 0.25mm outer-ring spall.

Figure 5.7 compares the excitation pulse spectrum and dynamic response spectrum to a rolling-element moving over a spall of 8mm on the bearing's outer-ring. The analytical excitation pulse spectrum is calculated using Equation (2.15) and Equation (2.16).

Figure 5.7 shows that the notches in the measured dynamic response spectrum start to disappear at frequencies greater than 2000Hz. The damping effect of the lubrication causes the sinc shape of the excitation pulse spectrum to damp out with an increase in frequency [29]. This disappearance of the sinc shape of the excitation pulse spectrum results in the disappearance of the notches in the dynamic response spectrum. Similar results are seen in the report [26]; in this report, a series of simulations of a defective bearing under different lubrication conditions were presented to understand the lubrication's effect on the excitation pulse.

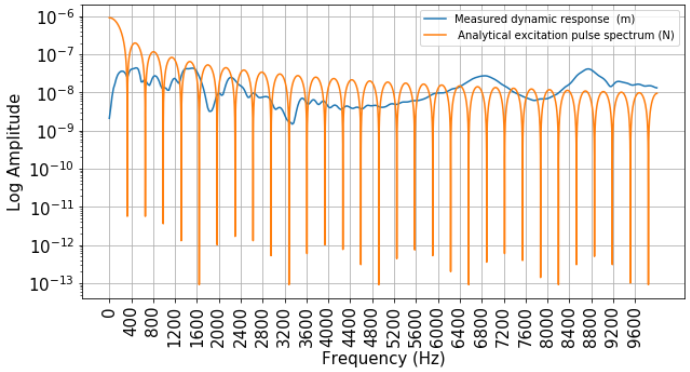

Figure 5.7 Dynamic response of the bearing with 8mm outer-ring spall.

From Figure 5.6 and Figure 5.7, it is seen that there is a small variation between the analytical notch frequency and the measured notch frequency of the dynamic response spectrum. This variation is caused by the error in the assumed value of:

- rotational speed
- Hertzian contact length

Next, the variation between the analytical notch frequency and the measured notch frequency from the spectrum is explained in relation to the error in the rotational speed and the Hertzian contact Length.

5.2.1 Error in Rotational speed and Frequency resolution

Figure 5.8 shows the difference between the measured notch frequency and the analytical notch frequency of a bearing with 0.25mm spall and under a load of 600N. From Figure 5.8, a difference of approximately $\pm$60Hz is seen. This difference is caused by the variation in the bearing's rotational speed ($\pm$10 rpm) and the RFT technique's frequency resolution (25Hz).

From equation (2.16), the $\pm$10RPM variation in the rotational speed results in a variation of $\pm$35Hz in the notch frequency when the bearing is under a load of 600N. The frequency resolution of the RFT technique used to extract the defective bearing's dynamic response in the frequency domain is $\pm$25Hz. Thus, the variation in the rotational speed and the frequency resolution results in a total variation of approximately $\pm$60Hz between the measured notch frequency and the analytical notch frequency.

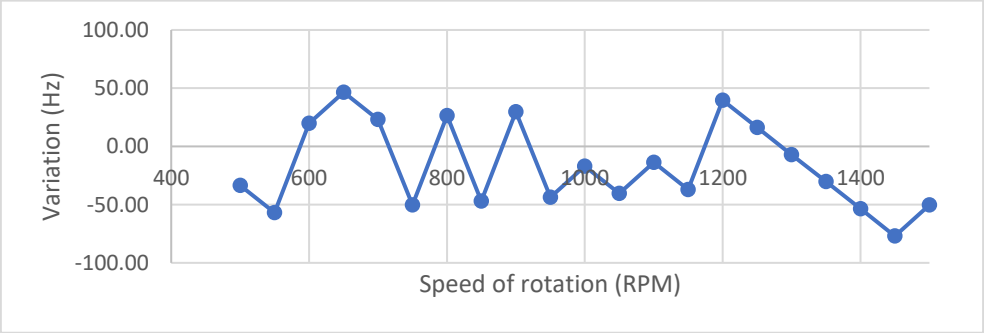

Figure 5.8 Variation in Notch frequency as a function of speed with 600N load and 0.25mm spall.

5.2.2 Error in the Hertzian contact length

Figure 5.9 shows the difference between the analytical notch frequency and the measured notch frequency for a bearing with spall of 0.1mm, 0.25mm, 0.5mm, 3mm, 5mm, and 8mm on its outer ring.

Figure 5.9 shows that bearings with spall size 0.1mm, 0.25mm, 3mm, 5mm, and 8mm have a small difference between measured notch frequency and the calculated analytical notch frequency. This difference between the theoretical notch frequency and the measured notch frequency is comparable to the variation caused by the error in the speed and the frequency resolution of the RFT technique used to extract the defective bearing's dynamic response in the frequency domain.

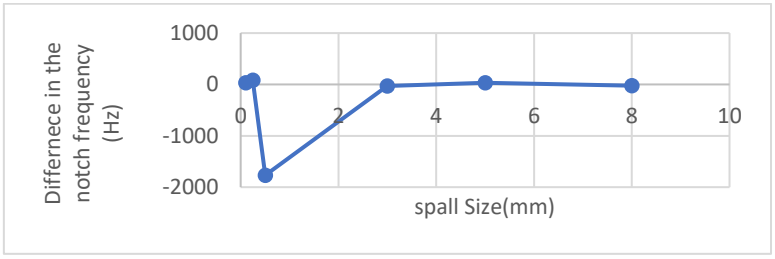

Figure 5.9 Difference between the notch frequency as a function of spall size.

Figure 5.9 shows that a bearing with a 0.5mm spall has a difference of approximately 1800Hz between the measured notch frequency and the calculated analytical notch frequency.

The Hertzian contact length is 0.52mm for bearings under the load of 600N. The size of the spall is smaller than the Hertzian contact. Therefore, the notch frequency is dependent on the Hertzian contact length and rotational speed. Thus, the variation should be caused either by a variation in speed or a variation in the Hertzian contact. The difference between the analytical and the measured notch frequency is considerably more than the variation caused by the variation in speed; the variation in Hertzian contact should be the reason for the cause of this error.

The difference between the analytical and the measured notch frequency for a bearing with a 0.5mm spall can be explained by the Hertzian contact error. The bearing's Hertzian contact length depends on the bearing parameters and load on the bearing. The variation in the bearing parameter is caused by the variation in the defective bearing preparation process. The process of preparing the defective bearing may have caused the shape and the clearance of the bearing to change, causing the detective bearing to have a smaller Hertzian contact length. However, further research is required to precisely quantify the variation of the notch frequency as a function of the variation in the bearing parameters and quantify the effect of the defective bearing parameters resulting from disassembling and assemble of bearing.

5.3 Frequency response function

In this section, the methods developed in Chapter 3 to estimate the FRF are validated and discussed using the measured experimental data.

The change in the stiffness due to the change in the applied load of 100N is negligible compared to the bearing's mass, as explained in Section 2.4. Therefore, the FRF of a bearing remains constant for a change in the load of 100N. However, the excitation pulse is load-dependent, as explained in section 2.2. If the shape of the estimated FRF changes with the load, then it would mean that the estimated FRF represents the excitation pulse and not the actual FRF of the bearing. This property of the FRF and the excitation pulse of the bearing is used to validate the methods developed to estimate the FRF of the bearing in Chapter 3.

5.3.1 Mean Filter

Figure 5.10 and Figure 5.11 represent the FRF of a bearing with a small spall (0.25mm) and large spall (8mm), extracted from its measured vibration signal using the Mean Filter method. From the figures, it is seen that the shape (peaks and notches) of the FRF under different loads is similar. This similar shape of the estimated FRF validates the Mean Filter method of estimating the FRF of a bearing from a uni-axial vibration signal.

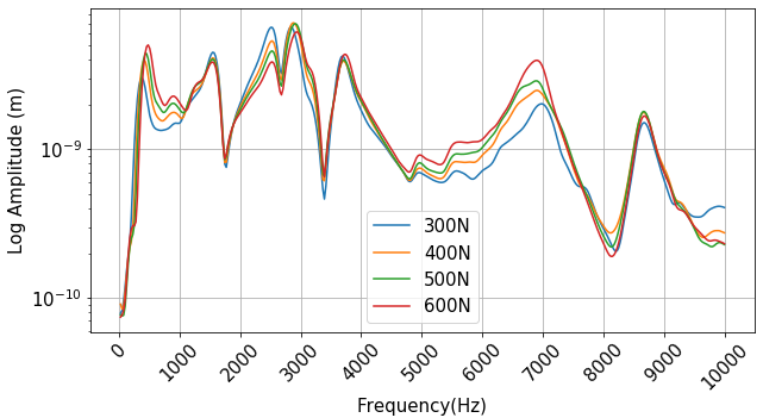

Figure 5.10 Mean Filter estimate of FRF of a bearing with 0.25mm spall.

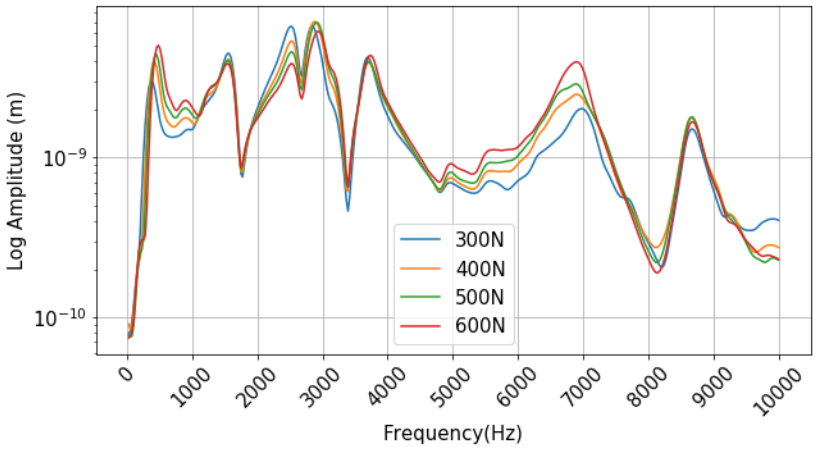

Figure 5.11 Mean Filter estimate of FRF of a bearing with 8mm spall bearing.

Figure 5.10 and Figure 5.11 shows an increase in the estimated FRF's amplitude with an increase in the load. The increase in load increases the amplitude of the measured vibration response. As the amplitude of the Mean Filter estimate of the FRF only depends on the amplitude of the measured vibration response, the estimated energy of the FRF increases with load.

However, in Figure 5.10**,** between the frequency range of 2000Hz to 3500Hz, the amplitude of the FRF decreases with an increase in the load. This is because the Hertzian contact length increases, and the notch frequency bandwidth decreases with the increased load. Thus, the number of notches between the 2000Hz and 3500Hz increases with the load, as seen in Figure 5.12 and Figure 5.13. Thus, the dynamic response spectrum's energy decreases between 2000Hz and 3500Hz, with an increase in load. Therefore, the amplitude of the FRF decreases with an increase in the load between 2000Hz and 3500Hz because the energy of the excitation pulse decreases.

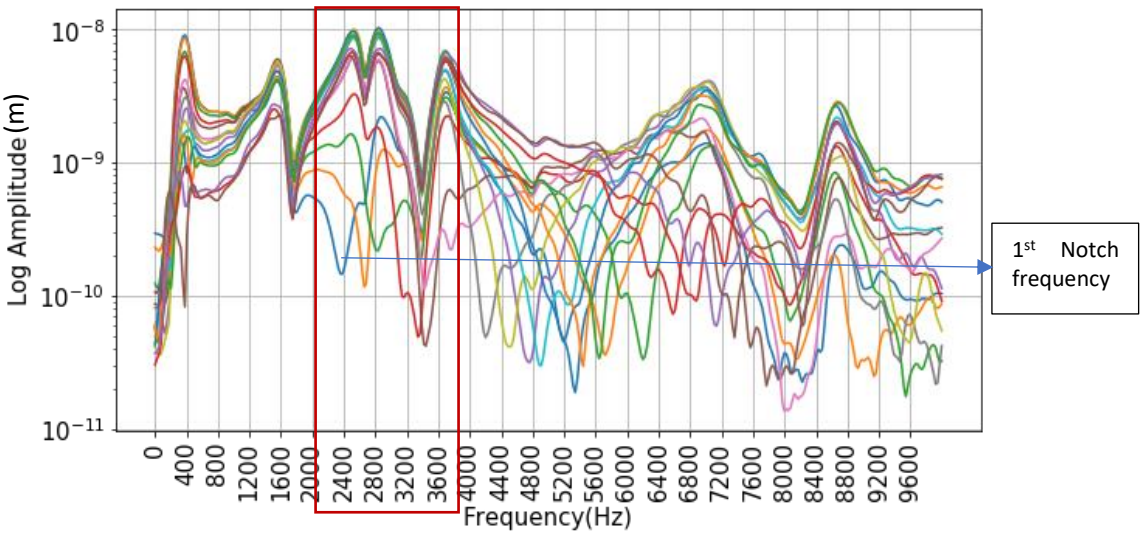

Figure 5.12 The measured dynamic response spectrum of a bearing with 0.25mm, 300N load.

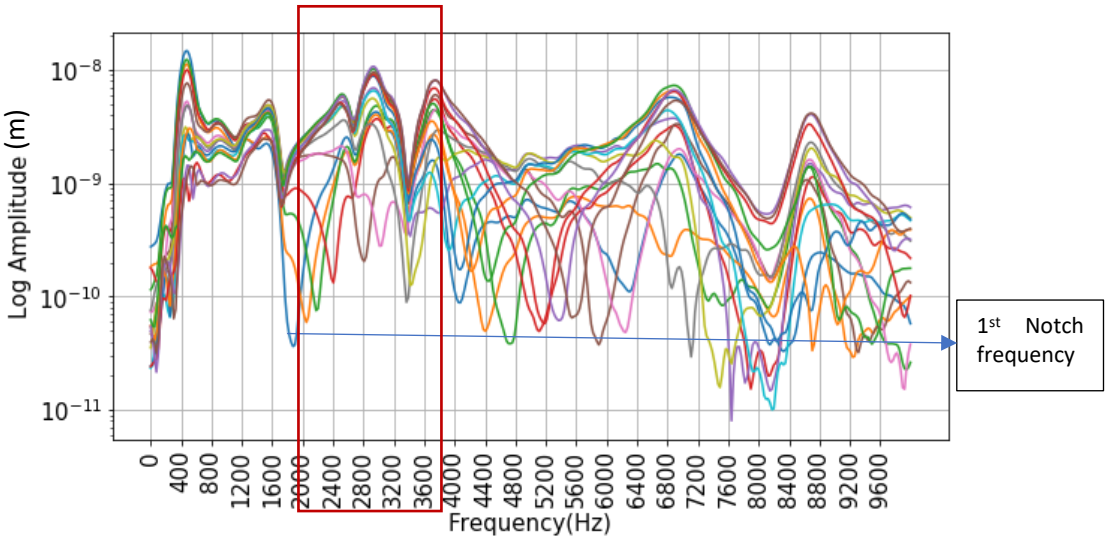

Figure 5.13 The measured vibration response in the frequency domain of a bearing with 0.25mm, 600N load.

Figure 5.14 compares the Mean Filter estimate of FRF for small spall (0.25mm) and large spall (8mm). The figure shows an increase in the overall energy of the FRF with an increase in the size of the spall. This increase in the energy is caused by the increase in the amplitude of the excitation pulse spectrum with the increase in the spall's size, as explained in Section 2.

The first resonance at 200Hz is seen more prominently seen for bearings with larger spalls because of the local maxima of the excitation pulse spectrum, as seen in Figure 5.14. For bearings with small spalls, the maxima of the first lobe of the excitation pulse spectra corresponding are approximately in the range of 1000Hz-2000Hz. For a bearing with large spalls, the maxima of the first lobe of the excitation pulse spectrum are in the lower frequency range (100Hz-300Hz) and excite the low-frequency resonance at 200Hz. Therefore, the first resonance mode at 200Hz is more prominently excited for larger defects

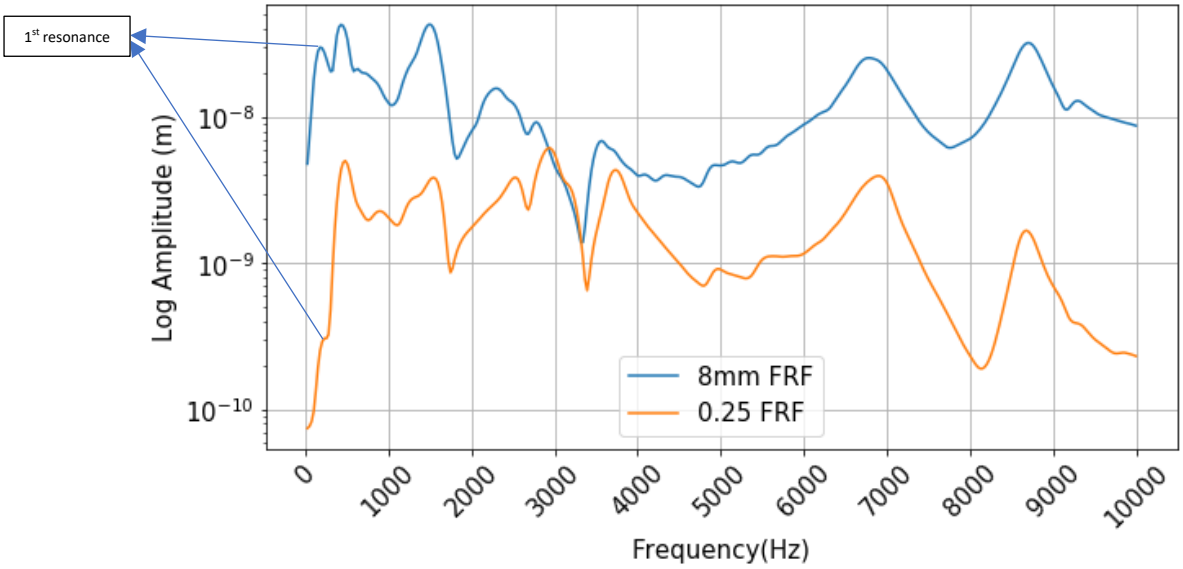

Figure 5.14 Comparison of the FRF of small (0.25mm) and large (8mm).

5.3.2 Kalman filter

Figure 5.15 and Figure 5.16 represent the FRF of a bearing with a small spall (0.25mm) and large spall (8mm), extracted from its measured vibration signal using the Kalman Filter method under a radial load 300N, 400N, 500N, and 600N. The figures show that the shape (peaks and notches) of the

estimated FRF under different loads is similar. This is because the change in the stiffness because of the change in the applied load is negligible compared to the bearing's mass. This similar shape of the estimated FRF validates the Kalman Filter implementation to estimate the FRF of the bearing.

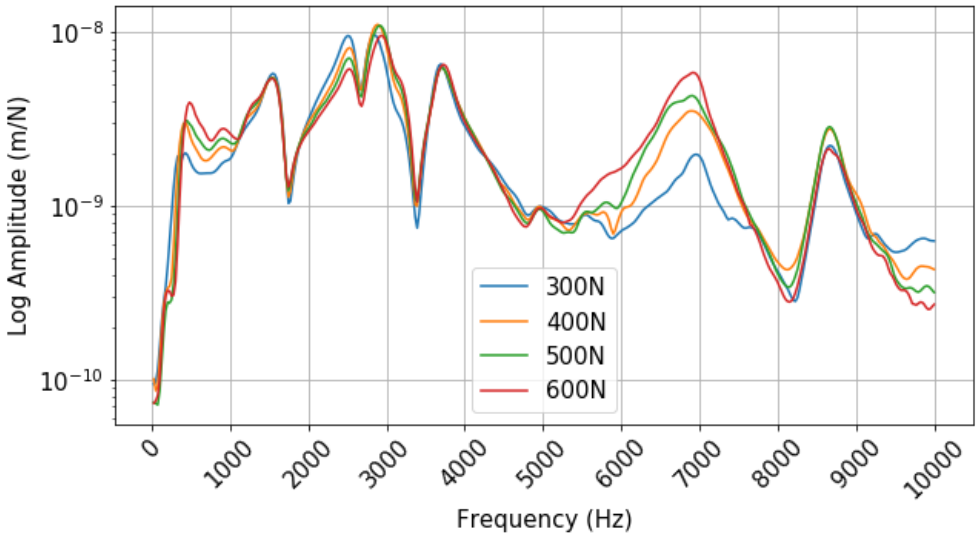

Figure 5.15 Kalman Filter estimate of FRF of bearing with 0.25mm spall.

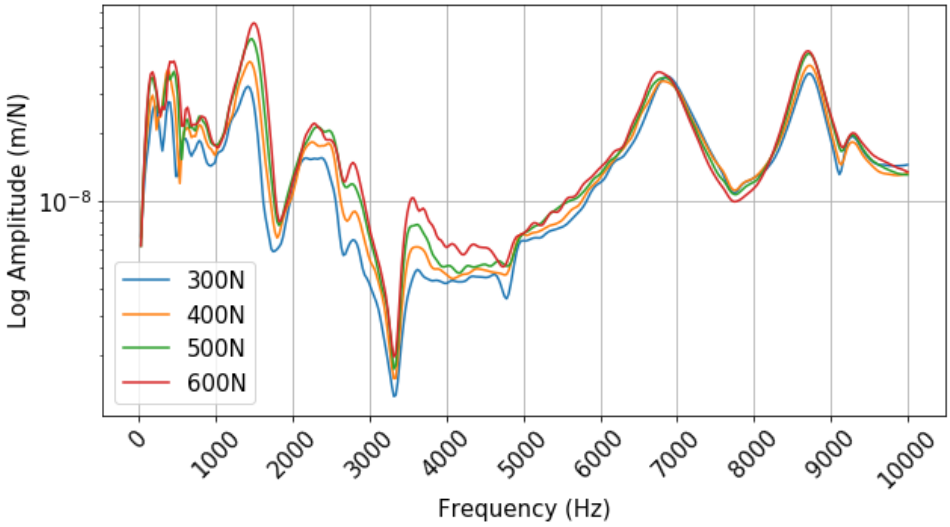

Figure 5.16 Kalman Filter estimate of FRF of bearing with 8mm spall

Figure 5.15 and Figure 5.16 shows an increase in the amplitude of the estimated FRF with an increase in the load. The Kalman filter implementation to estimate the FRF from the vibration response of a bearing is developed under the assumption that the excitation pulse spectrum is constant and is of unit magnitude irrespective of the bearing's load. Thus, the implementation of the Kalman filter estimate of the FRF depends only on the amplitude of the bearing's measured vibration response, as explained in Section 3.2 . The bearing's load increases the amplitude of the measured vibration response. Thus, the estimated FRF's energy increases with the increase in the applied load.

Figure 5.17, the first resonance at 200 Hz, is more prominently seen in bearing with larger spalls than at smaller spall. For large spalls (8mm), the maxima of the first lobe of the excitation pulse spectra are in the lower frequency range (100-300Hz) and excite the low-frequency resonance at 200Hz. The increase in the overall amplitude of the FRF is caused by the increase in the amplitude of the excitation force with the increase in the size of the spall, as explained in section 2.2 and section 2.3

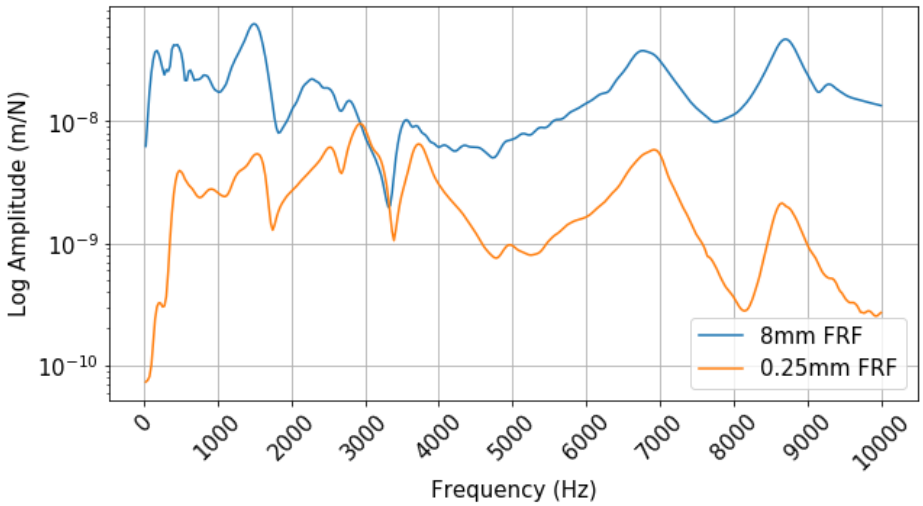

Figure 5.17 Comparison of the FRF estimate for large and small spall using Kalman Filter implementation.

5.3.3 Ensemble Kalman filter (EnKF)

In this section, the estimation of the FRF from a defective bearing's vibration response using the Ensemble Kalman Filter (EnKF) filter method presented in Section 3.2 is discussed and validated with the experimental data of a bearing with 0.25mm (small spall) and 8mm (large spall) on the outer ring of the bearing.

Figure 5.18 represents the FRF of bearing with a small spall (0.25mm) estimated from its measured vibration signal using the EnKF. The Ensemble Kalman filter implementation to estimate the FRF assumes that the excitation force pulse spectrum produced by the rolling-element moving over a defect to be a sinc function and the notches (local minima) of the sinc function to be speed dependent.

Figure 5.18 shows that the shape (peaks and notches) and the estimated amplitude of the FRF under different loads are similar. As the shape of the estimated FRF is not varying with load, this validates the estimated FRF using the EnKF implementation.

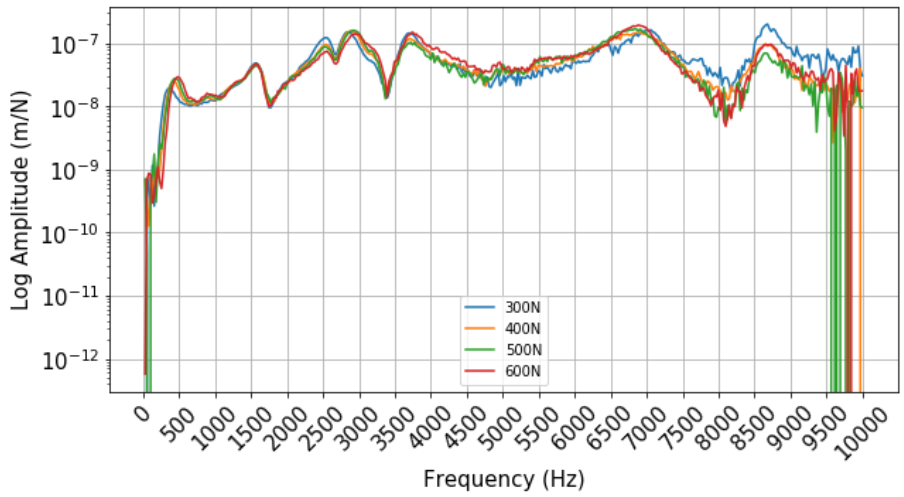

Figure 5.18 0.25mm spall, the mean of FRF using ENKF for 300N,400N,500N,600N loads.

The estimated FRF from the measured vibration response is noisy at higher frequencies, as shown in Figure 5.18. This is because the sinc function assumption deviates at higher frequencies (explained in Section 5.2).

Figure 5.19 shows peaks in the variance of the estimated FRF at specific frequencies. These peaks correspond to the uncertainty induced into the estimated FRF due to the notches in the measured dynamic response caused by the excitation pulse. The peaks caused by the notches of the latest measurement data are more prominently seen because the peaks (uncertainty) caused by the notches of initial measurements have reduced through the recursive process of the EnKF implementation, as shown in the Figure 5.20.

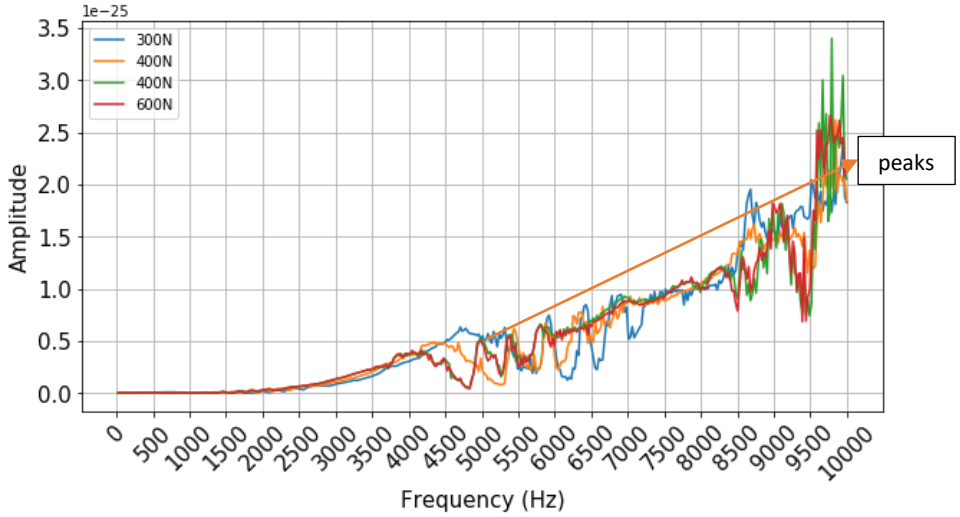

Figure 5.19 0.25mm spall, the variance of FRF using ENKF for 300N,400N,500N,600N loads.

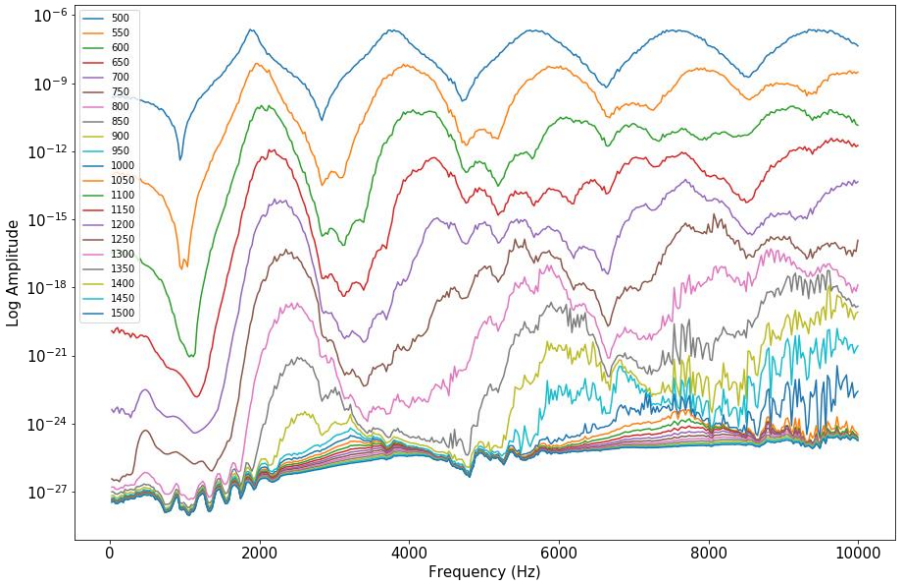

Figure 5.20 Change in the variance of the FRF through the speed-step.

Figure 5.21 represents the FRF of bearing with a large spall (8mm) on the outer-ring of the bearing extracted from its measured vibration signal using the EnKF implementation. From Section 5.2, it is understood that the sinc function assumption of the excitation pulse spectrum deviates at frequencies higher than 2000Hz. Thus, the EnKF implementation to estimate the FRF has comparatively higher variance at frequencies greater than 2000Hz, as shown in Figure 5.22. The Ensemble Kalman filter implementation is not successful in estimating the FRF for a bearing with large spalls.

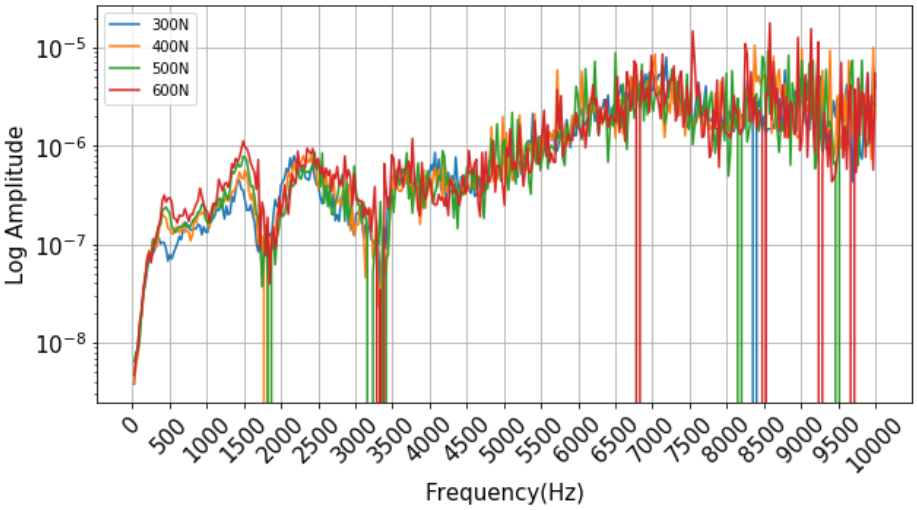

Figure 5.21 Mean of the estimated FRF of a bearing using ENKF for bearing with 8mm spall.

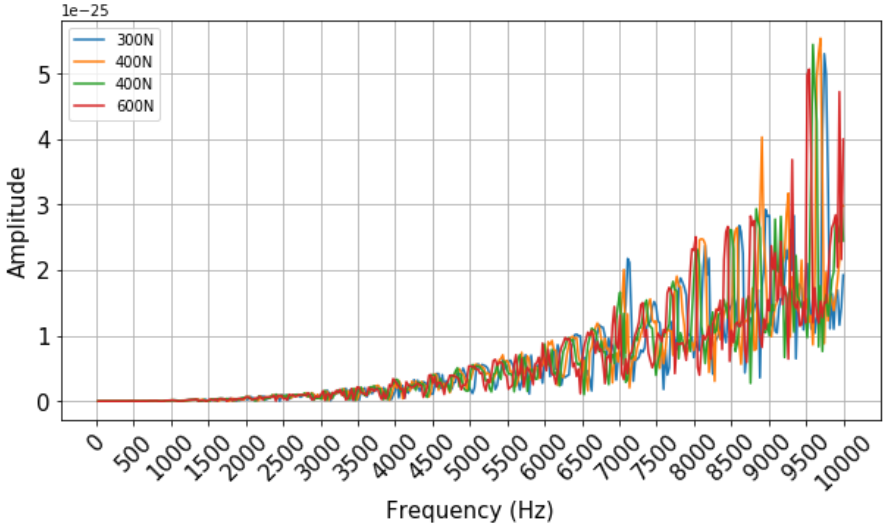

Figure 5.22 Variance of the estimated FRF using the EnKF of a bearing with 8mm spall.

5.4 Comparisons of the different methods implemented to estimate FRF

In this section, the different methods developed to estimate the FRF from the measured vibration response are compared. The results of the Mean Filter, Kalman filter implementation, and Ensemble Kalman filter implementation to estimate the FRF are presented in Table 2. The three methods are compared based on their ability to estimate the shape, amplitude, and the unit of the FRF from the uniaxial measured vibration signals for a bearing with small and large spalls.

Table 2 Overview of the methods

	Small spall			Large spall		
	Shape	Amplitude	Units	Shape	Amplitude	Units
Mean Filter	Yes	No	No	Yes	No	No
KalmanFilter implementation	Yes	No	Yes	Yes	No	Yes
EnKF implementation	Yes	Yes	Yes	No	No	Yes

From Table 2, it can be seen that the Mean filter and Kalman filter can estimate the shape of the FRF irrespective of the size of the spall. The Mean Filter estimation is the simplest method to estimate the shape of the frequency response function. However, it fails to estimate the right unit and the amplitude of the FRF.

The Kalman filter implementation successfully estimates the shape and the units of FRF for a bearing with both small and large spalls. However, fails to estimate the exact amplitude of the FRF of the bearing.

The EnKF implementation to estimate the FRF of a bearing can be used to precisely estimate the shape, amplitude, and the units of the FRF of a bearing with small spalls. However, fails to precisely estimate the shape and the amplitude of the FRF for bearings with large spalls. The EnKF implementation cannot estimate the FRF for larger spalls because it assumes that the excitation pulse spectrum to be a sinc function. This assumption is deviating for frequencies greater than 2000Hz for large spalls. Further research needs to be done to develop the analytical model to estimate the characteristic excitation pulse spectrum at frequencies higher than 2000Hz.

6 Conclusion and Recommendation

This chapter concludes the thesis by summarizing the findings of this research. Suggestions for future work are discussed later in this chapter.

6.1 Conclusion

The spectral method used to monitor the size of the spall in a bearing can be further improved by knowing the FRF of the bearing. Thus, the main research question that was focused on in this thesis is:

How to estimate the frequency response function by processing the uni-axial vibration response of a rolling-element moving over a spall located on the bearing's outer-ring?

To successfully answer the main research question, some subquestions were introduced at the start of this report. Throughout the report, the evidence to answer these questions are stated. The questions and their summarized answers are:

How do the properties of the dynamic response of a defective bearing change with the speed, load, and size of the defect?

From this thesis, it was shown to be valid that the dynamic response is characterized into two types, based on the size of the spall. The two types are:

1. **Small spall:** When the rolling-element moves over a small spall, it resulted in a single excitation pulse. The duration of this excitation pulse is dependent on the Hertzian contact length and the rotational speed of the bearing.
2. **Large spalls**: If the size of the spall is are larger than the Hertzian contact length in the direction of rotation, it is characterized to be a large spall. When the rolling-element moves over a large spall, the rolling-element loses complete contact with the raceways. A rectangular pulse is produced at the location of the spall when the rolling-element is detached from the raceways during the over-roll. The duration of this pulse is dependent on the speed of rotation, the size of the spall, and the Hertzian contact.

The dynamic response of a bearing to the excitation pulse in the frequency domain has peaks and notches due to the excitation pulse, resonance, and anti-resonances of the bearing.

The notches (local minima) in the frequency domain caused by the excitation pulse are dependent on the speed and the load. The notches and the peaks in the dynamic response spectrum caused by the resonance and anti-resonance of the bearing are independent of speed and load.

For larger spalls, the notches in the measured dynamic response caused by the excitation pulse start to disappear at frequencies greater than 2000Hz. This disappearance of the notches in the dynamic response is caused by the damping of the excitation pulse due to the lubricant's viscoelastic properties.

How to process the vibration signal to extract the bearing's dynamic response in the frequency domain to the rolling element moving over a spall?

The Repetitive Fourier Transform (RFT) technique is successful in processing the vibration signal to extract the bearing's dynamic response in the frequency domain to the rolling-element moving over a spall.

How can a data-driven approach, combined with an analytical model, be used to estimate the frequency response function from the bearing's measured dynamic response?

Three methods were developed in this thesis to estimate the FRF of a defective bearing from the measured vibration response. The three methods were Mean Filter, Kalman filter implementation, and Ensemble Kalman filter implementation.

The Mean Filter method was developed based on the assumption that the FRF of the bearing is independent of speed and load; the excitation pulse is dependent on the speed and load. Applying the Mean Filter method on the experimental data and synthetic data showed that it successfully estimated the shape of the FRF. However, failed to estimate the exact amplitude and the unit of the FRF.

Kalman filter implementation to estimate FRF developed based on the assumption that the FRF is independent of speed and the excitation pulse spectrum is of unit magnitude. Applying this method to the experimental data and synthetic data showed that this method successfully estimated the shape and the unit of the FRF for bearings with large and small spalls. However, it was unable to estimate the amplitude of the FRF precisely.

EnKF implementation to estimate FRF developed based on the assumption that the excitation pulse spectrum's notch frequency is known with some uncertainty. It also assumes that the bearing's frequency response function is independent of speed and load. EnKF implementation successfully estimates the shape and amplitude of the FRF of a bearing with small spalls. However, this method fails for larger spalls at frequencies greater than 2000Hz.

6.2 Recommendations and Future work

The EnKF implementation presented in this thesis can estimate the shape and amplitude of the FRF of the bearing with small defects. For bearings with large spalls, either Mean Filter or Kalman filter can be implemented to estimate the shape of the FRF, but they fail to estimate the actual amplitude of the FRF. Much work is still to be done to improve the FRF estimation. If this is done, the estimation of the size of the spall will be more efficient. Thus, improving the condition monitoring techniques of the bearing. The following recommendations are made to improve further and expand the FRF estimation of a bearing:

Error quantification: The error in the experimental data (measurement error) can be quantified by calibrating and testing the vibration sensors and load sensors. The error in the Hertzian contact length and spall length caused by the defective bearing preparation process quantifies modelling error. This information can be used to precisely model the error covariance matrix of the Kalman filter and Ensemble Kalman filter estimate.

Real-spalls: Real spalls do not have sharp straight edges like the artificial spall developed in this thesis in this thesis. Detailed research on the excitation pulse spectra of the real-spalls and the efficiency of the three methods have to be investigated.

Location of the sensors: Understand the variation in the FRF as a function of the location of the spall with respect to the location of the sensor. This understanding will explain the variation in the dynamic response function when the spall is located on either the inner-ring or the rolling-element. This insight will help improve the spall size estimation of bearing with spalls on either the rolling-element or the inner-ring.

Analytical excitation pulse spectrum: The analytical approximation of the excitation pulse spectra for larger defects needs to be further improved to include the damping effect of lubrication. This new

analytical model can be implemented in the EnKF implementation to estimate the FRF of bearing with large spalls.

As more knowledge is acquired about all the phenomena and errors in the defective bearing, methods can be further be improved to precisely estimate the FRF and the size of the defect. In the not too far future, the axle bearing of a train might be maintained based on their condition. This will improve the reliability, life, and maintenance planning of the Train wheelset.

7 References

[1] S. Kallas, “Roadmap to a single European transport area - Towards a competitive and RESOURCE-EFFICIENT transport system,” Publications Office of the European Union, Luxembourg, 2011.

[2] M. Asplund, “Wayside Condition Monitoring Technologies for Railway Systems,” Luleå University of Technology, Graphic Production, Lulea, 2014.

[3] SKF, “New Storage Concept for freight wagons,” *Evolution technology magazine from SKF,* 2005.

[4] SKF Group, “Bearing damage and failure analysis,” SKF Group, Nieuwegein, 2017.

[5] H. Mol and A. Gabelli, “Model Based Detection and Diagnosis of Bearing Defects,” in *European Conference Of The Prognostics And Health Management Society*, 2018.

[6] M. Entezami, C. Roberts, P. Weston, E. Stewart, A. Amini and M. Papaelias, “Perspectives on railway axle bearing condition monitoring,” *Journal of rail and rapid transit,* vol. 234, no. 1, pp. 17-31, 2020.

[7] N. Sawalhi and R. Randall, “Vibration response of spalled rolling element bearings: Observations, simulations and signal processing techniques to track the spall size,” *Mechanical Systems and Signal Processing,* vol. 25, no. 3, pp. 846-870, 2011.

[8] S. Singh, U. G.Köpke, C. Q.Howard and D. Petersena, “Analyses of contact forces and vibration response for a defective rolling element bearing using an explicit dynamics finite element model,” *Journal of Sound and Vibration,* vol. 333, no. 21, pp. 5356-5377, 2014.

[9] A. M. Ahmadi, D. Petersen and C. Howard, “A nonlinear dynamic vibration model of defective bearings – The importance of modelling the finite size of rolling elements,” *Mechanical Systems and Signal Processing,* Vols. 52-53, pp. 309-326, 2015.

[10] D. Petersen, C. Howard, N. Sawalhi, A. M. Ahmadi and S. Singh, “Analysis of bearing stiffness variations, contact forces and vibrations in radially loaded double row rolling element bearings with raceway defects,” *Mechanical Systems and Signal Processing,* Vols. 50-51, pp. 139-160, 2015.

[11] G. Kogan, R. Klein and J. Bortman, “A physics-based algorithm for the estimation of bearing spall width using vibrations,” *Mechanical System and Signal processing,* vol. 104, pp. 398-414, 2018.

[12] G. Kogan, J. Bortman and R. Klein, “A new model for spall-rolling-element interaction,” *Non-linear Dynamics,* vol. 87, pp. 219-236, 2017.

[13] A. M. Ahmadi, C. Howard and D. Petersen, “The path of rolling elements in defective bearings: Observations, analysis and methods to estimate spall size,” *Journal of Sound and Vibration,* vol. 366, pp. 277-292, 2016.

[14] R. Kumar and M. Singh, “Outer race defect width measurement in taper roller bearing using discrete wavelet transform of vibration signal,” *Measurement,* vol. 46, no. 1, pp. 537-545, 2013.

[15] M. Singh, R. K. Yadav and R. Kumar, “Discrete Wavelet Transform Based Measurement of Inner Race Defect Width in Taper Roller Bearing,” *MAPAN,* vol. 28, p. 17–23, 2013.

[16] M. Singh and R. Kumar, “Thrust bearing groove race defect measurement by wavelet decomposition of pre-processed vibration signal,” *Measurement ,* vol. 46, no. 9, pp. 3508-3515, 2013.

[17] S. Khanama, N. Tandona and J. K. Duttb, “Fault size estimation in the outer race of ball bearing using discrete wavelet transform of the vibration signal,” *Measurement,* vol. 14, pp. 12-19, 2014.

[18] H. Qiu, JayLee, J. Linc and G. Yud, “Robust performance degradation assessment methods for enhanced rolling element bearing prognostics,” *Advanced engineering informatics,* vol. 17, no. 3-4, pp. 127-140, 2003.

[19] D.P.Jena and S.N.Panigrahi, “Precise measurement of defect width in tapered roller bearing using vibration signal,” *Measurment,* vol. 55, pp. 39-50, 2014.

[20] A. R. Bastami and S. Vahid, “Estimating the size of naturally generated defects in the outer ring and roller of a tapered roller bearing based on autoregressive model combined with envelope analysis and discrete wavelet transform,” *Measurment,* vol. 156, 2020.

[21] W. Wang, N. Sawalhi and A. Becker, “Size Estimation for Naturally Occurring Bearing Faults Using Synchronous Averaging of Vibration Signals,” *Journal of Vibration and Acoustics,* vol. 5, p. 138, 2016.

[22] G. v. Nijen, P. v. Dalen, G. A. Dimitrov, V. v. Ravesteijn, M. Senesi, J. Stam and F. Tatar, Noise and vibration in bearing system, Nieuwegein: SKF Research & Technology Development, 2015, pp. 9-28.

[23] S. Elsayed, A. M. Elkhatib and M. Yakout, “Vibration Modal Analysis of Rolling Element Bearing,” in *International Conference on Integrity, Reliability and Failure*, Funchal, Portugal, 2013.

[24] B.Vervisch, S.Derammelaere, K.Stockman and M.Loccufier, “Frequency response functions and modal parameters of a rotating system exhibiting rotating damping,” in *International Conference on Noise and Vibration Engineering (ISMA)*, Leuven, Belgium, 2014.

[25] J. A. Wensing, “On the dynamics of ball bearing,” SKF , Twente, 1998.

[26] H. Mol, “Condition Monitoring of Bearings by Vibrations,” Group Development Centre / Mechatronics, NIEUWEGEIN, 2014.

[27] J. Ravesloot,, “A semi-analytical approach to simulate strains in load sensing bearings using FEA,” Delft, 2020.

[28] S. Singh, U. Kopke, C. Howard and D. Petersen, “Analyses of contact forces and vibration response for a defective rolling element bearing using an explicit dynamics finite element model,” *Journal of Sound and Vibration,* vol. 333, no. 21, pp. 5356-5377, 2014.

[29] G. v. Nijen, P. v. Dalen, A. G. Dimitrov, V. V. Ravesteijn, M. Senesi, J. Stam and F. Tatar, Noise And Vibration in Bearing System, Nieuwegein, 2017.

[30] Y. Pei, S. Biswas, D. S. Fussell and K. Pingali, “An Elementary Introduction to Kalman Filtering,” *arXiv,* 2019.

[31] D. Simon, Optimal State Estimation ,Kalman, H, and Nonlinear Approaches, Wiley & Sons, Inc, 2006.

[32] M. Roth, G. Hendeby and F. Gustafsson , “The Ensemble Kalman filter: a signal processing perspective,” *Journal on Advances in Signal Processing ,* no. 56 , 2017.

[33] Y. Tang, J. Ambandan and D. Chen, “Nonlinear Measurement Function in the Ensemble Kalman Filter,” *Advances in Atmospheric Science,* vol. 31, pp. 551-558, 2014.

[34] H. Mol, “SKF Technical Report,” SKF, Utrecht, 2018.

Appendix A

The dimensionless contact parameters are used to calculate the semi-axes of the Hertzian contact ellipse and the contact deformation shown in the table below.

Table 3

$F(\rho)$	a^*	b^*	δ^*
0	1	1	1
0.1075	1.076	0.9318	0.9974
0.3204	1.2623	0.8114	0.9761
0.4795	1.4556	0.7278	0.9429
0.5916	1.644	0.6687	0.9077
0.6716	1.8258	0.6245	0.8733
0.7332	2.011	0.5881	0.8394
0.7948	2.265	0.548	0.7961
0.83495	2.494	0.5186	0.7602
0.87366	2.8	0.4863	0.7169
0.90999	3.233	0.4499	0.6636
0.93657	3.738	0.4166	0.6112
0.95738	4.395	0.383	0.5551
0.9729	5.267	0.349	0.496
0.983797	6.448	0.315	0.4352
0.990902	8.062	0.2814	0.3745
0.995112	10.222	0.2497	0.3176
0.9973	12.789	0.2232	0.2705
0.998185	14.839	0.2072	0.2427
0.998916	17.974	0.18822	0.2106
0.999479	23.55	0.16442	0.17167
0.999853	37.38	0.1305	0.11995

Appendix B

In this section, the synthetic data generation is presented. The synthetic data is generated to verify the three methods developed in Chapter 3 to estimate the FRF. Synthetic data is generated using a dynamic model of a defective bearing. The dynamic model of a bearing is given by:

$$y = hf + \eta \tag{B.1}$$

where the y the dynamic response of the bearing in the frequency domain to an excitation pulse f in the frequency domain. The frequency response function, which relates the excitation pulse to the dynamic response, is given by h; η is the background noise.

Excitation pulse: An excitation pulse is generated when the rolling-element moves over a defect to the system. The duration of the excitation pulse is given by:

$$T = \frac{2b}{V} \tag{B.2}$$

A range of synthetic excitation pulses is generated for a bearing with an 0.25mm defect on the outer-ring of a 6206 SKF bearing for speeds ranging from 500RPM to 1500RPM in the steps of 50RPM. The Hertzian contact length in the direction of the rotation is 0.40mm. The figure below represents the excitation pulse in the frequency domain.

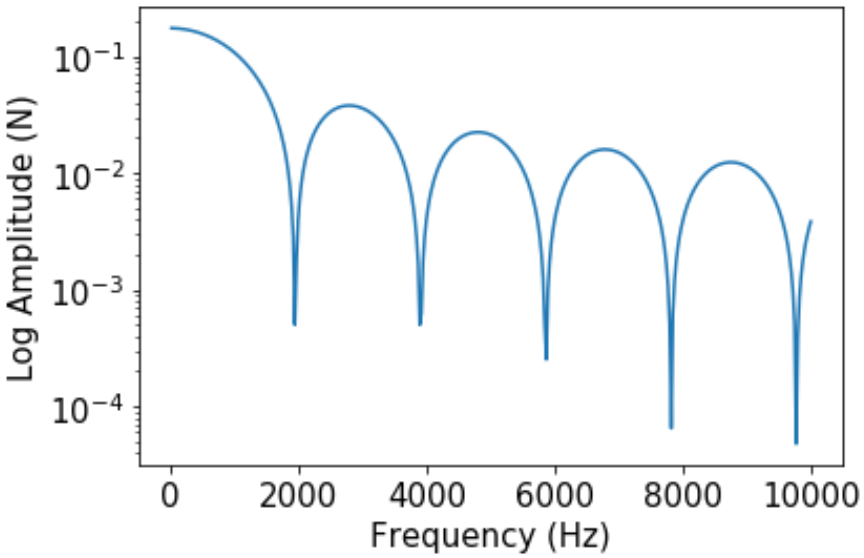

Figure B.1 Excitation Pulse Spectra at 500RPM

Frequency response function: An FRF of a radially loaded 6206 bearing with a defect on the outer ring is taken as the FRF for the synthetic data. The figure below shows the FRF of the synthetic data.

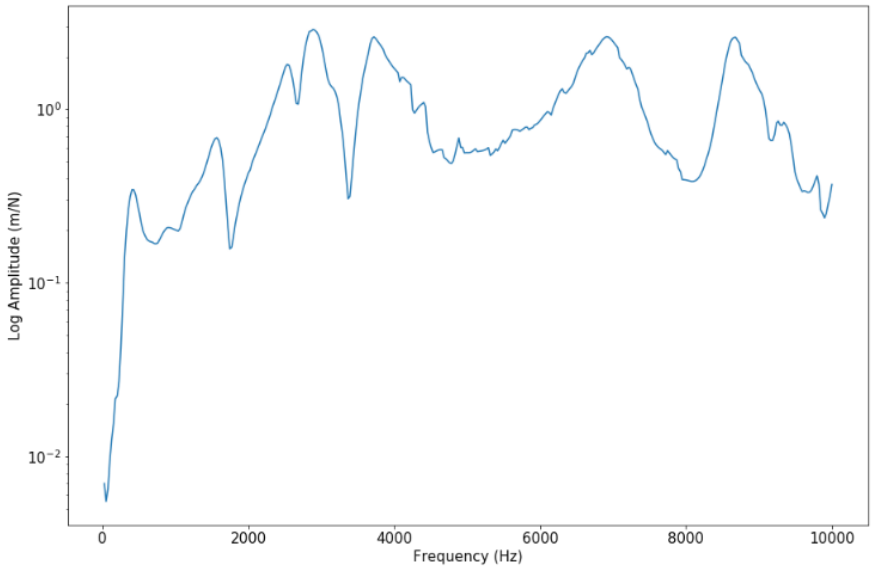

Figure B.2 Synthetic Frequency response function

Dynamic response: The dynamic response to this excitation pulse is a product of the excitation pulse in the frequency domain and the frequency response function. The figure below shows the dynamic response to the synthetic excitation pulse for a bearing rotating at 500RPM, with added background noise.

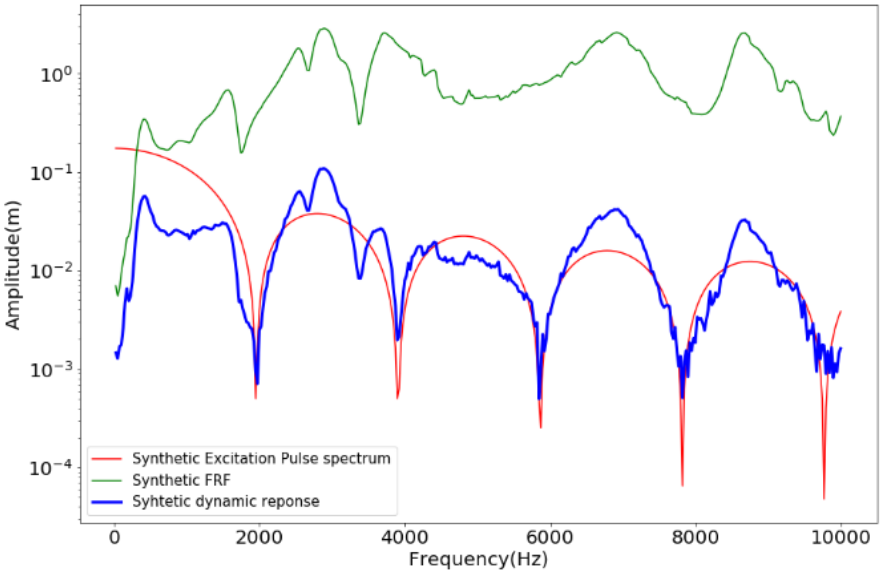

Figure B.3 Synthetic data

Similarly, the dynamic response at different speeds ranging from 500RPM to 1500RPM in the steps of 50RPM is calculated.

Appendix C

In this section, the estimated FRF using the Mean Filter, Kalman filter implementation, and Ensemble Kalman Filter implementation of bearing with spall size 0.1mm, 0.25mm, 0.5mm, 3mm, 5mm, and 8mm are presented.

Mean Filter:

Mean Filter estimate of the frequency response function estimated for bearing with different defect size is presented below:

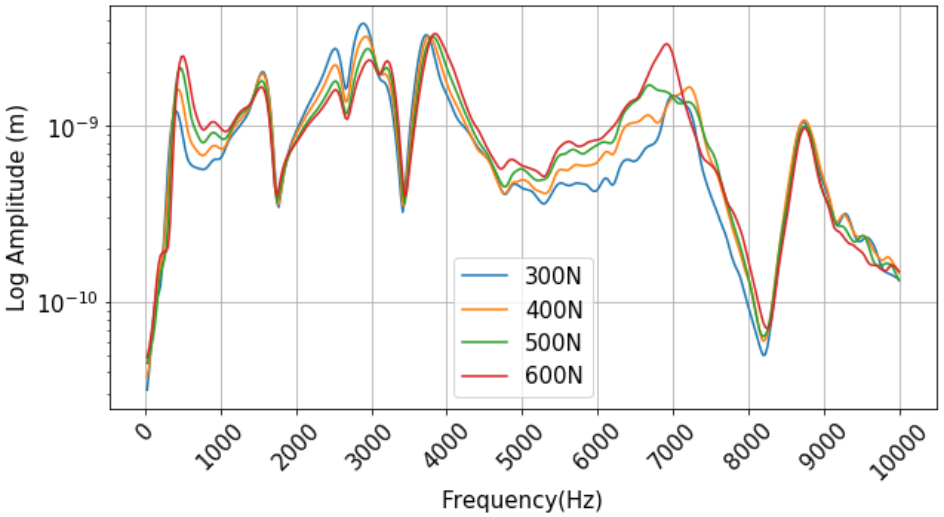

Figure C.1 Mean Filter estimate of the FRF of a bearing with 0.1mm spall

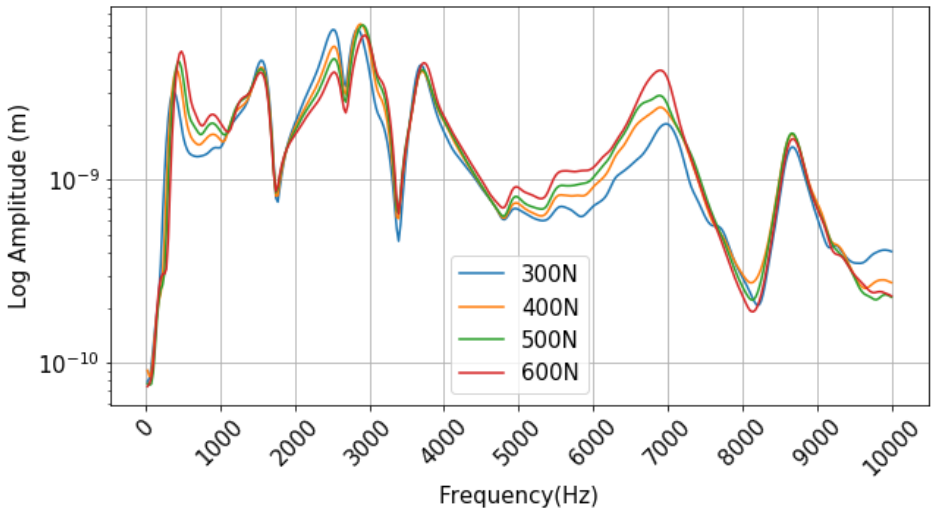

Figure C.2 Mean Filter estimate of the FRF of a bearing with 0.25mm defect

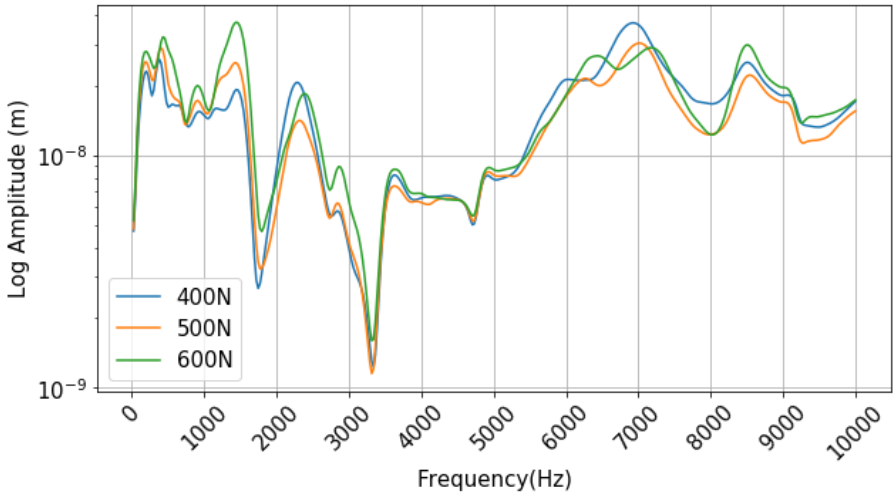

Figure C.3 Mean Filter estimate of the FRF of a bearing with 0.5mm spall

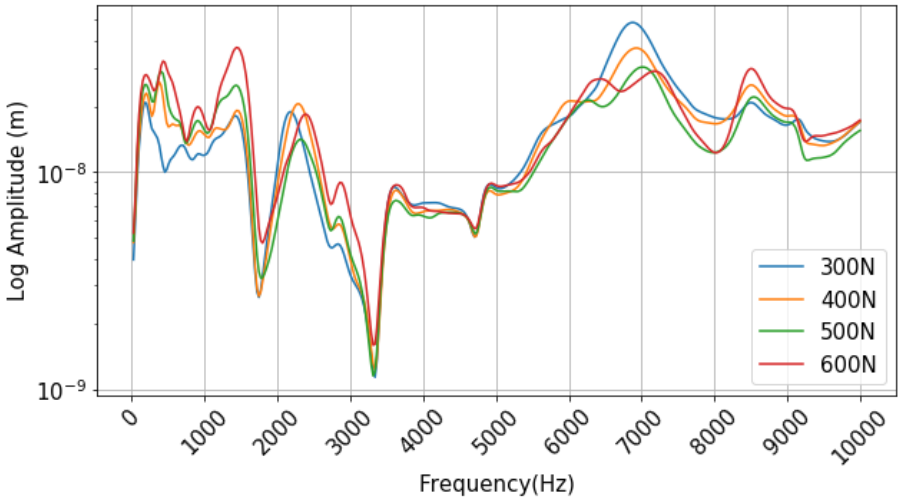

Figure C.4 Mean Filter estimate of the FRF of a bearing with 3mm spall

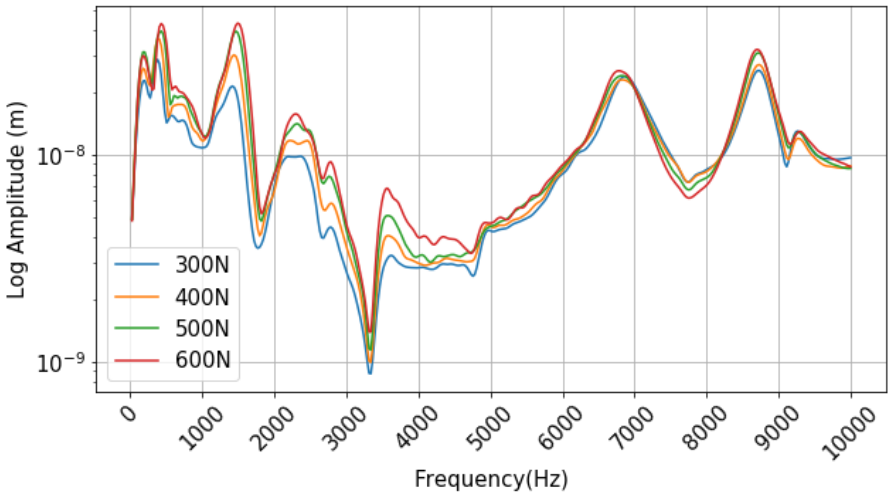

Figure C.5 Mean Filter estimate of the FRF of a bearing with 5mm spall

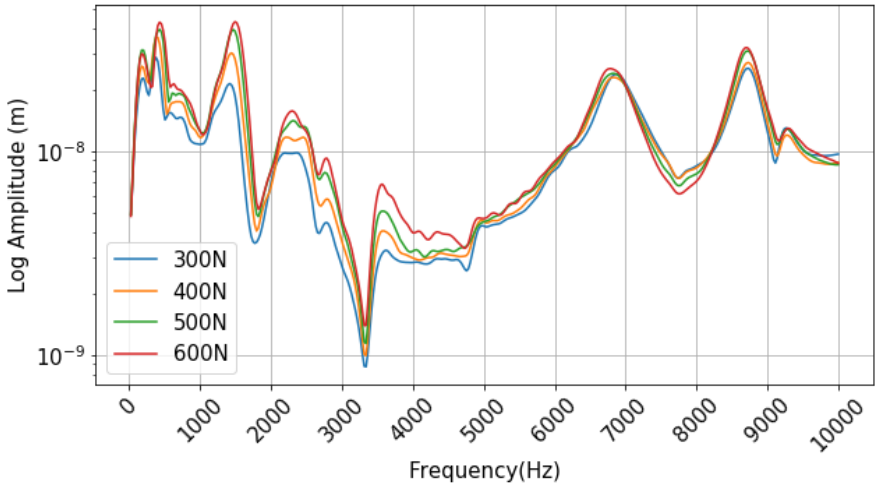

Figure C.6 Mean Filter estimate of the FRF of a bearing with 8mm spall

Kalman Filter Estimate of FRF

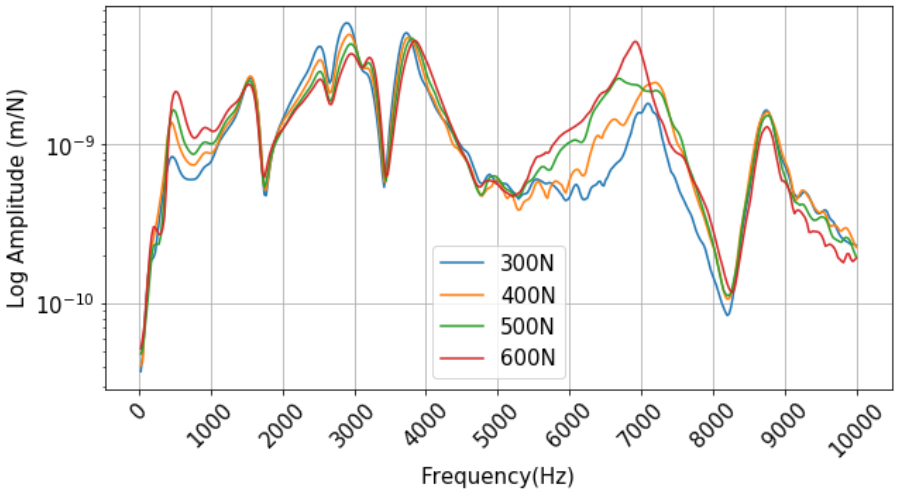

Figure C.7 Kalman Filter estimate of the FRF of a bearing with 0.1mm spall

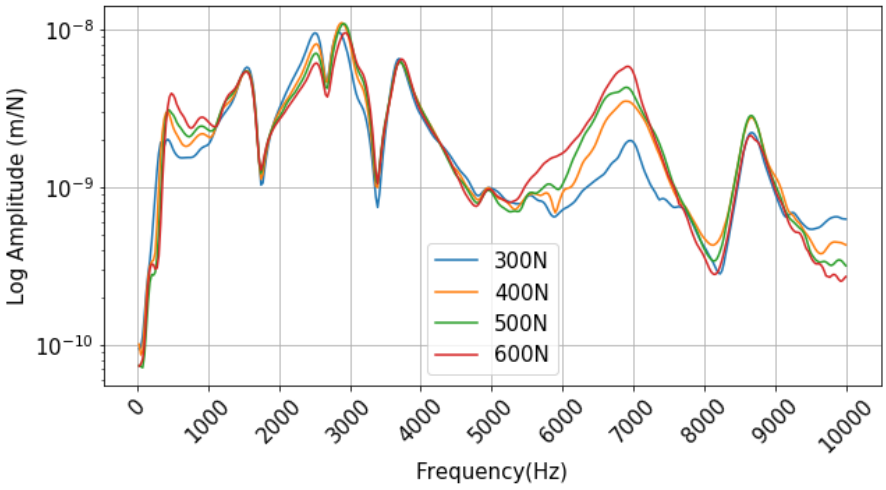

Figure C.8 Kalman Filter estimate of the FRF of a bearing with 0.25mm spall

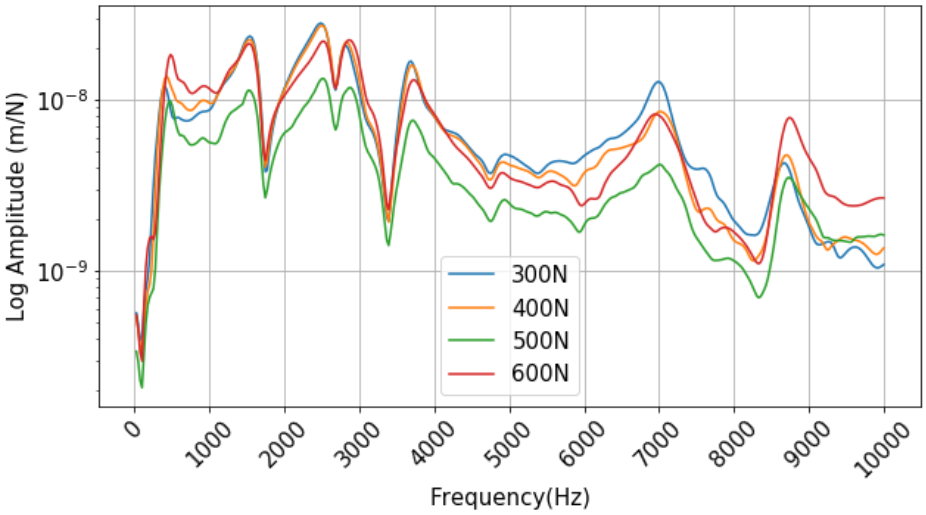

Figure C.9 Kalman Filter estimate of the FRF of a bearing with 0.5mm spall

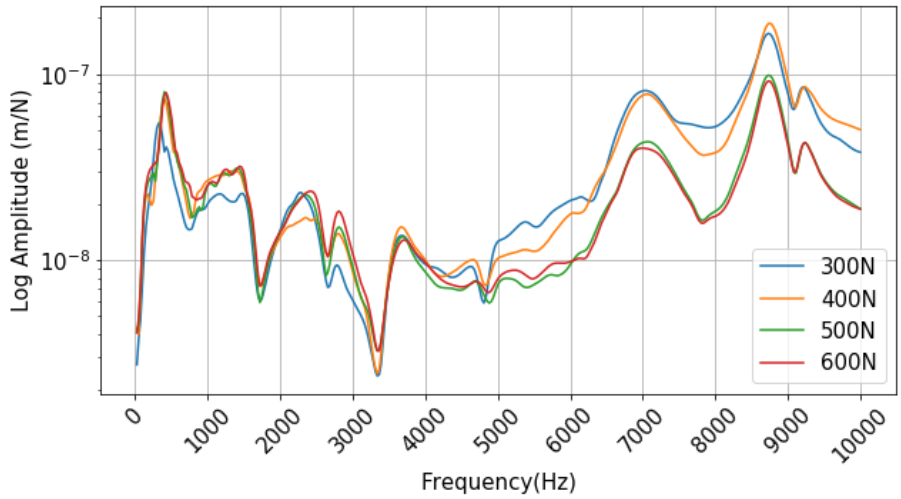

Figure C.10 Kalman Filter estimate of the FRF of a bearing with 3mm defect

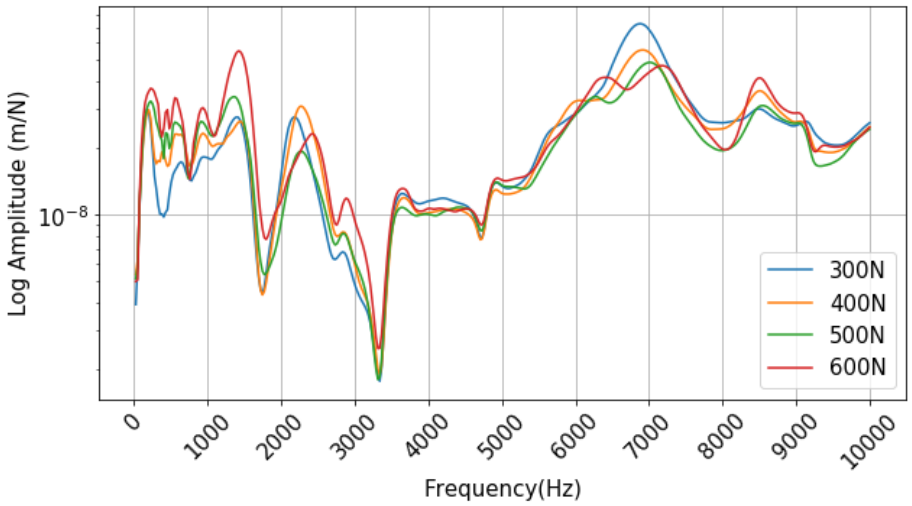

Figure C.11 Kalman Filter estimate of the FRF of a bearing with 5mm defect

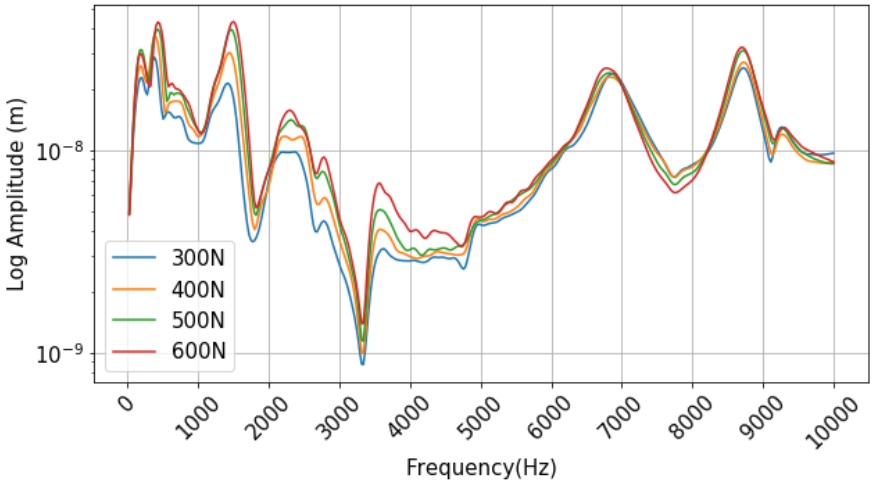

Figure C.12 Kalman Filter estimate of the FRF of a bearing with 8mm spall

Ensemble Kalman Filter

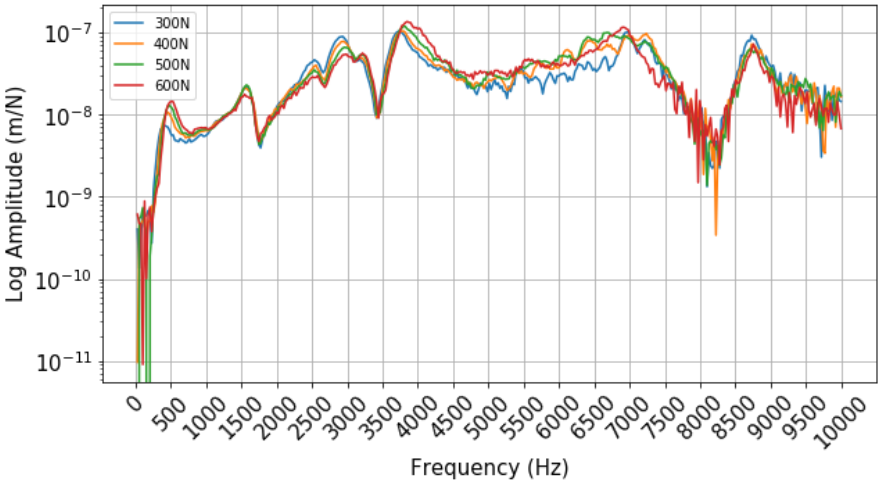

Figure C.13 Mean of EnKF estimate of the FRF of a bearing with 0.1mm spall

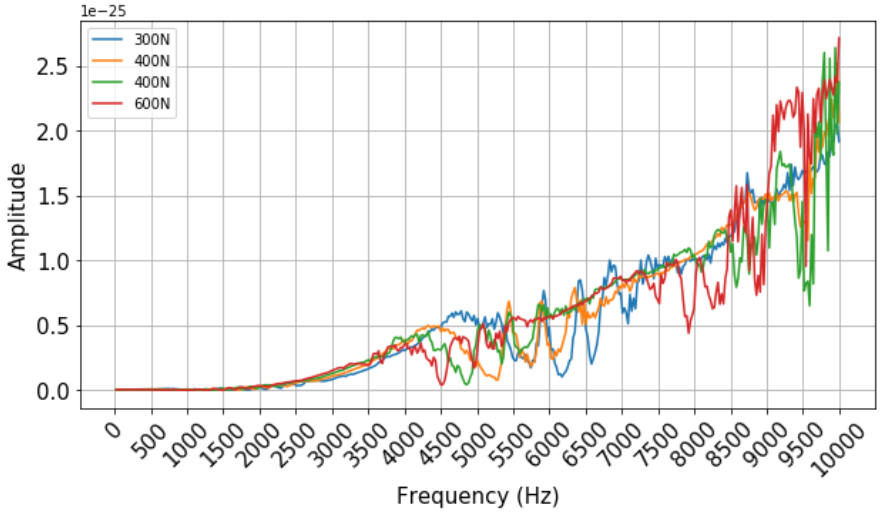

Figure C.14 Variance of EnKF estimate of the FRF of a bearing with 0.1mm spall

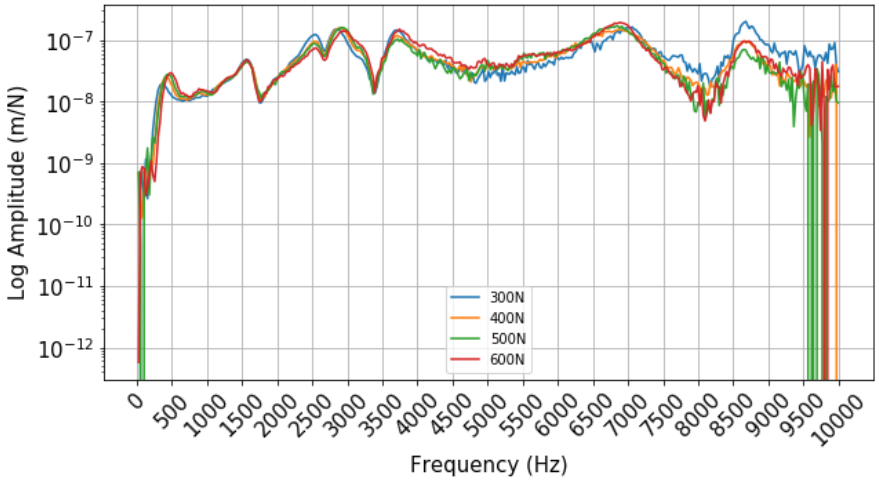

Figure C.15 Mean of EnKF estimate of the FRF of a bearing with 0.25mm spall

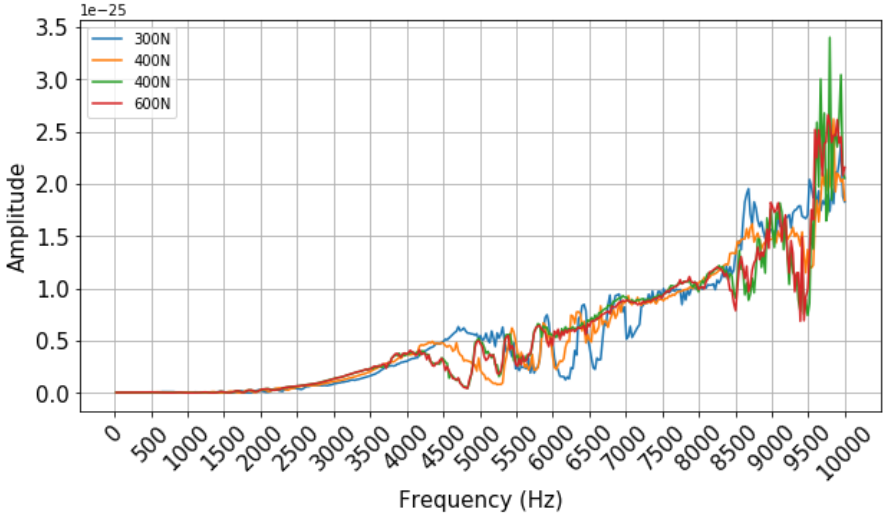

Figure C.16 Variance of EnKF estimate of the FRF of a bearing with 0.25mm spall

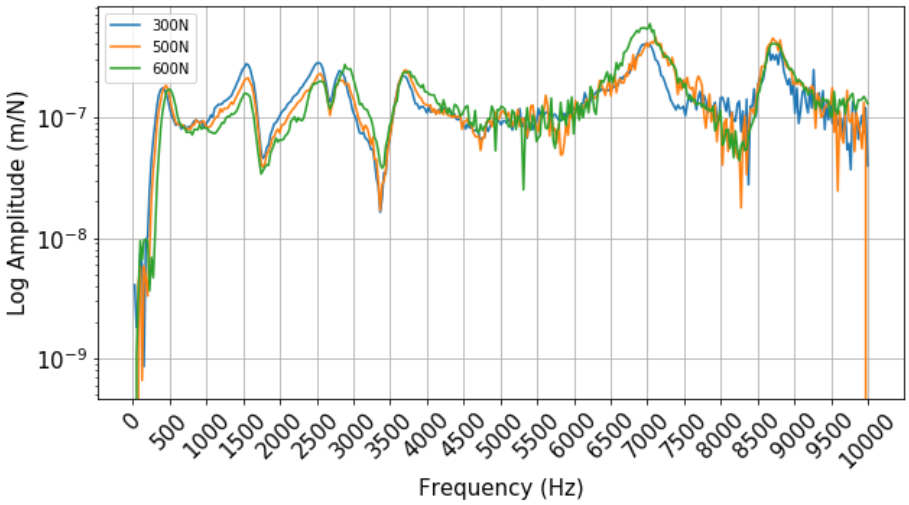

Figure C.17 Mean of EnKF estimate of the FRF of a bearing with 0.5mm spall

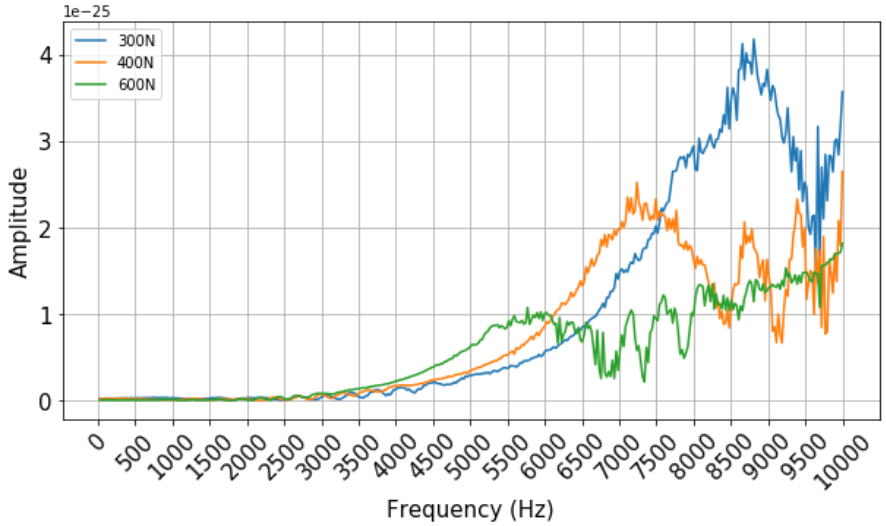

Figure C.18 Variance of EnKF estimate of the FRF of a bearing with 0.5mm spall

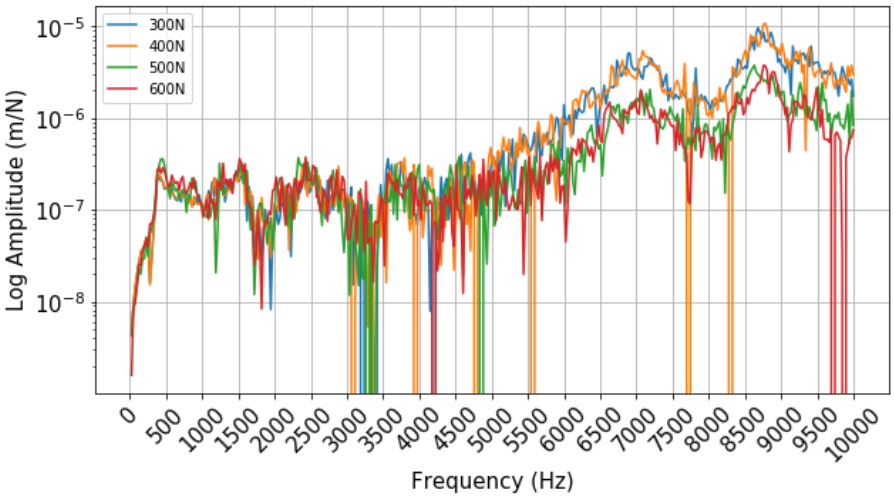

Figure C.19 Mean of EnKF estimate of the FRF of a bearing with 3mm spall

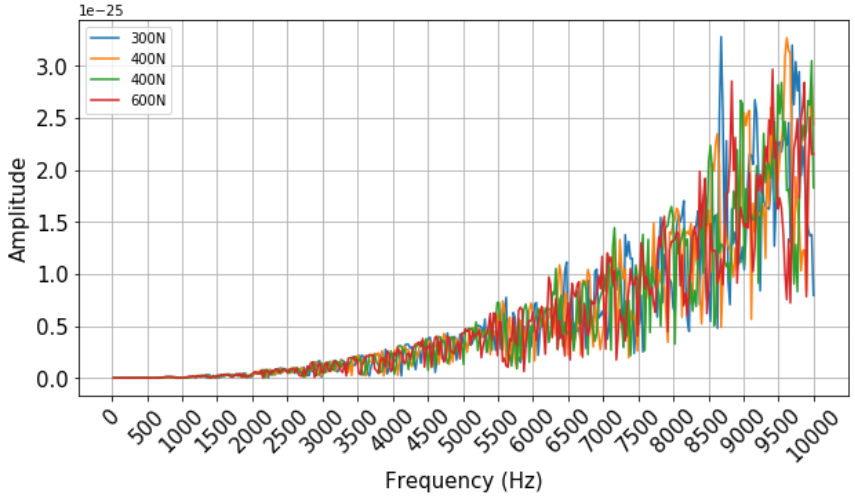

Figure C.20 Variance of EnKF estimate of the FRF of a bearing with 3mm spall

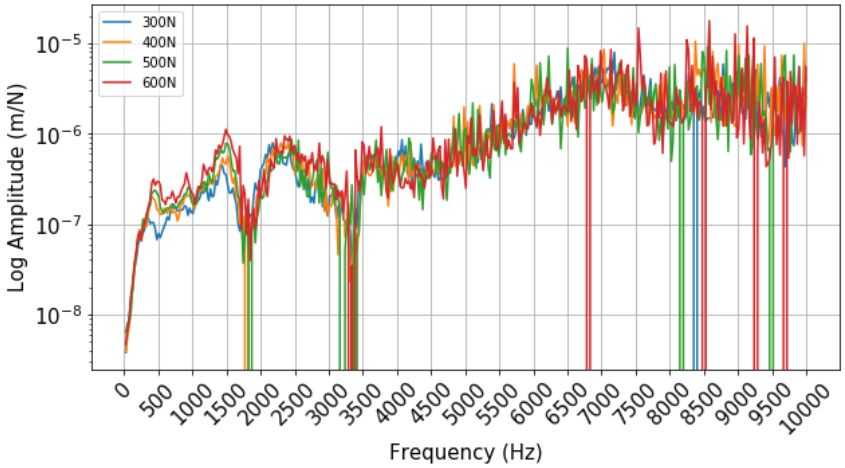

Figure C.21 Mean of EnKF estimate of the FRF of a bearing with 5mm spall

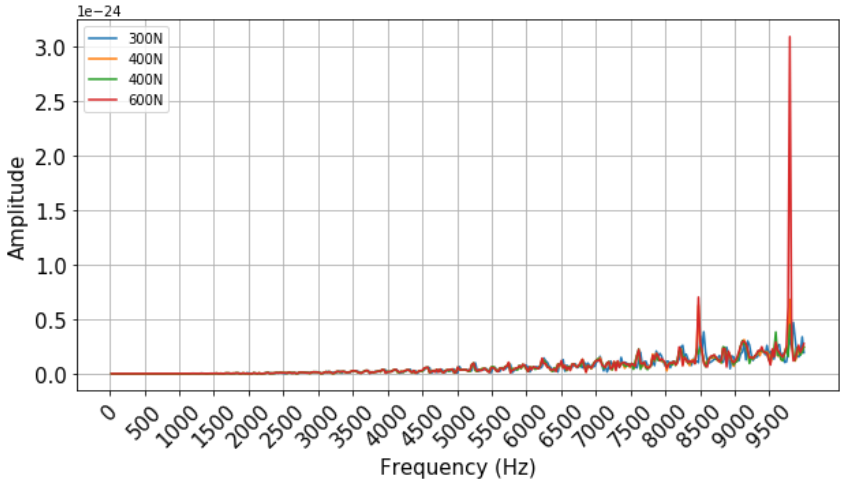

Figure C.21 Variance of the EnKF estimate of the FRF of a bearing with 5mm spall